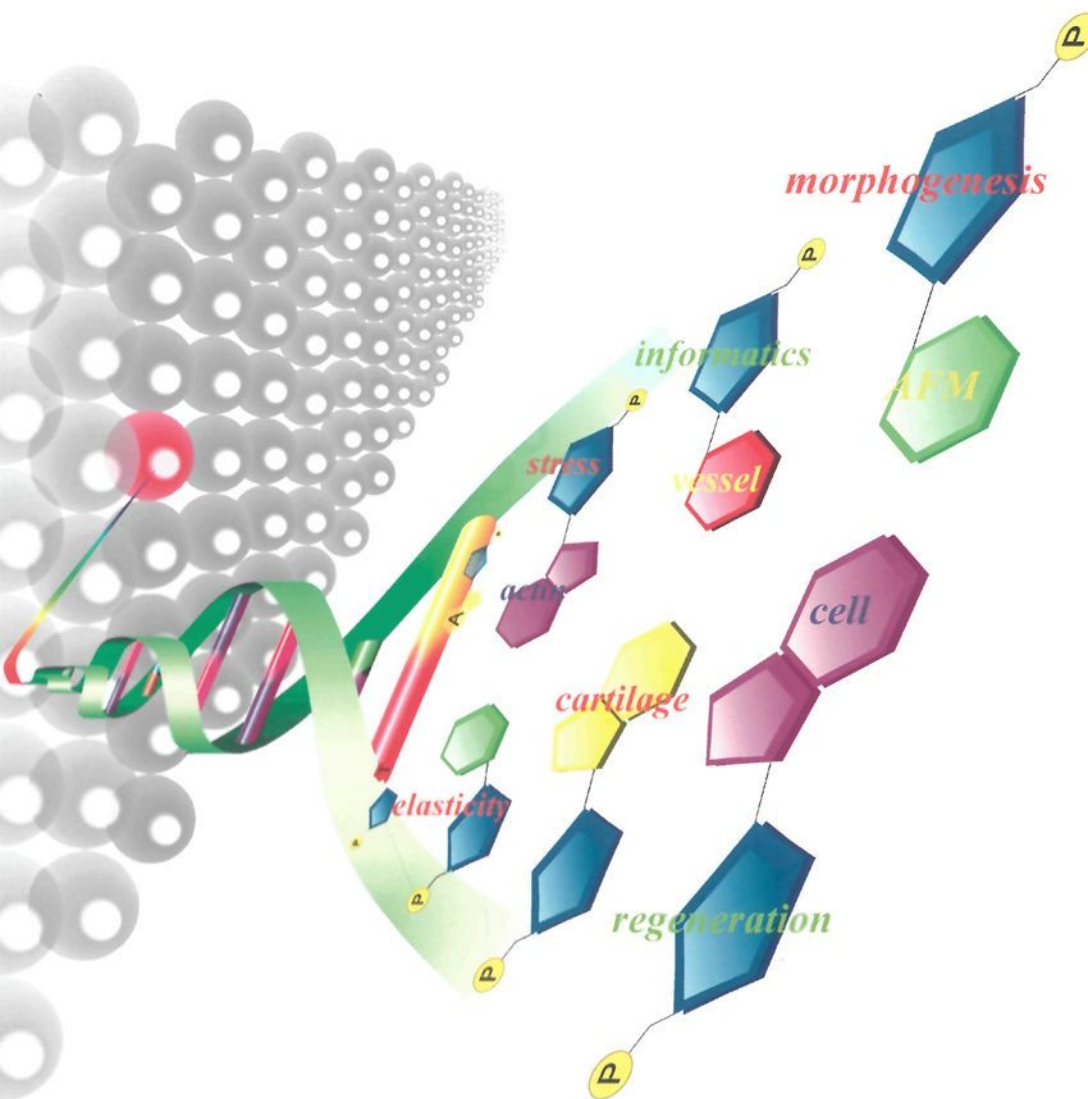


# BIOMECHANICS AT MICRO- AND NANOSCALE LEVELS

VOL. II



Hiroshi Wada *editor*

**BIOMECHANICS AT  
MICRO- AND NANOSCALE  
LEVELS**

**VOLUME II**

# **Biomechanics at Micro- and Nanoscale Levels**

*Editor-in-Charge:* Hiroshi Wada  
(*Tohoku University, Sendai, Japan*)

---

*Published*

Vol. I: Biomechanics at Micro- and Nanoscale Levels  
*Edited by Hiroshi Wada*  
ISBN 981-256-098-X

BIOMECHANICS AT  
MICRO- AND NANOSCALE  
LEVELS

VOLUME II

*editor*

Hiroshi Wada

*Tohoku University, Sendai, Japan*

 World Scientific

NEW JERSEY • LONDON • SINGAPORE • BEIJING • SHANGHAI • HONG KONG • TAIPEI • CHENNAI



*Published by*

World Scientific Publishing Co. Pte. Ltd.

5 Toh Tuck Link, Singapore 596224

*USA office:* 27 Warren Street, Suite 401-402, Hackensack, NJ 07601

*UK office:* 57 Shelton Street, Covent Garden, London WC2H 9HE

**British Library Cataloguing-in-Publication Data**

A catalogue record for this book is available from the British Library.

**BIOMECHANICS AT MICRO- AND NANOSCALE LEVELS**

**Volume II**

Copyright © 2006 by World Scientific Publishing Co. Pte. Ltd.

*All rights reserved. This book, or parts thereof, may not be reproduced in any form or by any means, electronic or mechanical, including photocopying, recording or any information storage and retrieval system now known or to be invented, without written permission from the Publisher.*

For photocopying of material in this volume, please pay a copying fee through the Copyright Clearance Center, Inc., 222 Rosewood Drive, Danvers, MA 01923, USA. In this case permission to photocopy is not required from the publisher.

ISBN 981-256-746-1

Printed in Singapore by Mainland Press

## PREFACE

A project on “Biomechanics at Micro- and Nanoscale Levels,” the title of this book, was approved by the Ministry of Education, Culture, Sports, Science and Technology of Japan in 2003, and this four-year-project is now being carried out by fourteen prominent Japanese researchers. The project consists of four fields of research, which are equivalent to four chapters of this book, namely, Cell Mechanics, Cell Response to Mechanical Stimulation, Tissue Engineering, and Computational Biomechanics.

Our project can be summarized as follows. The essential diversity of phenomena in living organisms is controlled not by genes but rather by the interaction between the micro- or nanoscale structures in cells and the genetic code, the dynamic interaction between them being especially important. Therefore, if the relationship between the dynamic environment of cells and tissues and their function can be elucidated, it is highly possible to find a method by which the structure and function of such cells and tissues can be regulated. The first goal of this research is to understand dynamic phenomena at cellular and biopolymer-organelle levels on the basis of mechanics. An attempt will then be made to apply this understanding to the development of procedures for designing and producing artificial materials and technology for producing or regenerating the structure and function of living organisms.

We are planning to publish a series of books related to this project, this book being the second in the series. The trend and level of research in this area in Japan can be understood by reading this book.

Hiroshi Wada, PhD,  
Project Leader,  
Tohoku University,  
Sendai,  
March, 2005.

This page is intentionally left blank

# CONTENTS

<b>PREFACE</b>	<b>v</b>
<b>I. CELL MECHANICS</b>	<b>1</b>
Heterogeneous expression of the motor protein prestin of cochlear outer hair cells	3
<i>H. Wada, K. Iida, S. Kumano, M. Murakoshi, K. Tsumoto K. Ikeda, I. Kumagai and T. Kobayashi</i>	
Effects of actin filaments on anisotropy and stiffness of aortic smooth muscle cells	16
<i>T. Matsumoto and K. Nagayama</i>	
Micro-vessel network formation of endothelial cells with in vitro three dimensional model	26
<i>K. Tanishita, A. Ueda, M. Koga, R. Sudo, S. Kudo and M. Ikeda</i>	
Time-dependent mechanical behaviors of articular cartilage and chondrocytes under constant total compressive deformation	37
<i>T. Murakami, N. Sakai, Y. Sawae, Y. Kurohara, I. Ishikawa and M. Okamoto</i>	
<b>II. CELL RESPONSE TO MECHANICAL STIMULATION</b>	<b>49</b>
Threshold fiber strain that induces reorganization of cytoskeletal actin structure in osteoblastic cells	51
<i>T. Adachi and K. Sato</i>	
Morphology of endothelial cells in response to hydrostatic pressure	62
<i>M. Sato</i>	
Mechanosensing in intestinal villi: ATP signaling in subepithelial fibroblasts network	72
<i>K. Furuya, S. Furuya and M. Sokabe</i>	

<b>III. TISSUE ENGINEERING</b>	<b>85</b>
Microelements for cartilage tissue engineering <i>K. Tsuchiya, K. S. Furukawa and T. Ushida</i>	87
Interrelationship between water filtration velocity and the thickness of pseudointima formed at the wall of artificial vascular grafts implanted in the dog common carotid artery <i>T. Karino, M. Kaichi and T. Ishizaka</i>	96
Strengthening of fibrous tissues under mechanical stimuli <i>K. Takakuda</i>	108
<b>IV. COMPUTATIONAL BIOMECHANICS</b>	<b>119</b>
Assessment of cortical bone microstructure using monochromatic synchrotron radiation micro-CT <i>T. Matsumoto, M. Yoshino and M. Tanaka</i>	121
Study on particle presentations of blood cells and the plasma in microvascular blood flow <i>T. Yamaguchi, S. Wada, K. Tsubota, H. Kamada and Y. Kitagawa</i>	132
Brief reviews of mechanical models of skeletal muscle and formulation of a muscle model taking into account microstructure and damage <i>E. Tanaka and D. Ito</i>	141
Numerical simulation of the effects of actin binding and cellular deformation on the orientation of actin stress fibers under cyclic stretch <i>H. Yamada, H. Ando and D. Morita</i>	149
<b>SUBJECT INDEX</b>	<b>161</b>

# **I. CELL MECHANICS**

This page is intentionally left blank

# HETEROGENEOUS EXPRESSION OF THE MOTOR PROTEIN PRESTIN OF COCHLEAR OUTER HAIR CELLS

H. WADA, K. IIDA, S. KUMANO AND M. MURAKOSHI

*Department of Bioengineering and Robotics, Tohoku University,  
6-6-01 Aoba-yama, Sendai 980-8579, Japan  
E-mail: wada@cc.mech.tohoku.ac.jp*

K. TSUMOTO

*Department of Medical Genome Sciences, Graduate School of Frontier Sciences,  
The University of Tokyo, 5-1-5 Kashiwanoha, Kashiwa, Chiba 277-8651, Japan*

K. IKEDA

*Department of Otorhinolaryngology, Juntendo University School of Medicine,  
2-1-1 Hongo, Bunkyo-ku, Tokyo 113-8421, Japan*

I. KUMAGAI

*Department of Biomolecular Engineering, Tohoku University,  
6-6-07 Aoba-yama, Sendai 980-8579, Japan*

T. KOBAYASHI

*Department of Otorhinolaryngology, Head and Neck Surgery, Tohoku University,  
Graduate School of Medicine, 1-1 Seiryomachi, Sendai 980-8675, Japan*

High sensitivity of human hearing is believed to be achieved by cochlear amplification. The basis of this amplification is thought to be the motility of mammalian outer hair cells (OHCs), i.e., OHCs elongate and contract in response to acoustical stimulation. This motility is thought to be based on voltage-dependent conformational changes of a motor protein embedded in the lateral wall of the OHC. In 2000, this motor protein was identified and termed prestin. Since identification of prestin, intensive research has been done using prestin-expressing cells to elucidate the function of prestin. However, the motor function of prestin at the molecular level is still unclear. To obtain knowledge about the function of prestin, it should be studied using not only prestin in cells, but also prestin in solution. For this purpose, a method of obtaining a large amount of prestin as material is required. In this study, an attempt was therefore made to construct an expression system for prestin. Prestin cDNA was introduced into *Escherichia coli* (*E. coli*), insect cells and Chinese hamster ovary (CHO) cells, and the expression of prestin was examined by Western blotting. As CHO cells expressed prestin well, we generated prestin-expressing cell lines using CHO cells by limiting dilution cloning. The stable expression, the N-linked glycosylation and the activity of prestin in generated cell lines were then confirmed.



## 1 Introduction

Mammalian hearing sensitivity relies on a mechanical amplification mechanism based on the electromotility of outer hair cells (OHCs) [1-5]. This mechanism enables the high sensitivity, wide dynamic range and sharp frequency selectivity of hearing in mammals [6]. The molecular basis of this mechanism is thought to be voltage-dependent conformational changes of motor proteins, which are embedded in the plasma membrane of the OHC lateral wall [7, 8].

In 2000, this motor protein was identified by a cDNA library subtraction procedure and termed prestin [9]. Since its identification, prestin has been intensively researched to elucidate the characteristic behavior of the OHCs. As a result, it has been confirmed that prestin-transfected mammalian cells show characteristic features of the OHC based on its motor protein, i.e., they exhibit voltage-dependent nonlinear capacitance [9-11], electromotility [9] and force generation [10]. It has also been clarified that intracellular anions act as voltage sensors of prestin [13]. In addition, the importance of prestin for the auditory mechanism was demonstrated by the fact that prestin knock-out mice exhibited a loss of outer hair cell electromotility *in vitro* and a significantly elevated hearing threshold of 40-60 dB *in vivo* [14, 15].

However, the motor function of prestin still needs to be understood at the molecular level. To obtain knowledge about the function of prestin, it is necessary to study prestin using purified protein. For this purpose, a method of obtaining a large amount of prestin as material is required. In this study, an attempt was therefore made to construct an expression system for prestin. First, a prestin gene was introduced into *Escherichia coli* (*E. coli*), insect cells and Chinese hamster ovary (CHO) cells, and the expression of prestin was examined by Western blotting. Second, as it was verified that CHO cells expressed prestin, limiting dilution cloning was done to generate prestin-expressing cell lines using the transfected CHO cells. Third, the stable expression of prestin in the generated cell lines was investigated by Western blotting. The N-linked glycosylation of prestin was also analyzed by Western blotting. Finally, the localization of prestin and the activity of prestin in the cell lines were examined by immunofluorescence experiments and whole-cell patch-clamp measurements, respectively.

## 2 Materials and Methods

### 2.1 Verification of expression in cells

*E. coli* expression vectors pET28b (Novagen, Madison, WI), pET20b (Novagen) and pMAL-c2 (New England Biolabs, Beverly, MA) were used for the *E. coli* expression system. Gerbil prestin cDNA was inserted into these vectors. The open reading frame of the prestin cDNA was fused in a frame with the His<sub>6</sub>-tag coding

sequence of the expression vector pET28b or pET20b. For this purpose, the stop codon was removed. To express prestin as a maltose-binding protein (MBP)-fusion protein, prestin cDNA was inserted into the pMAL-c2 expression vector. The *E. coli* strains BL21 and JM109 were transformed with pET28b or pET20b and pMAL-c2 *E. coli* expression vectors containing prestin cDNA, respectively. *E. coli* transformed with pET28b or pET20b was cultured in 200 ml 2 × YT medium at 28°C, and *E. coli* transformed with pMAL-c2 was cultured in 200 ml LB medium at 37°C. When the bacteria had grown to an optical density at 600 nm of 0.6, IPTG was added to a final concentration of 1 mM. After 2-5 hours, cells were harvested and the expression of prestin in bacteria was examined by Western blotting. When pET28b or pET20b was used, the expression was examined with anti-His<sub>6</sub> antibody (Invitrogen, Rockville, MD), and when pMAL-c2 was used, the expression was examined with anti-MBP antibody (New England Biolabs).

To use the baculovirus expression system, the pVL1392 transfer vector (PharMingen, San Diego, CA) was employed. Prestin cDNA fused at its 3' end to the His<sub>6</sub>-tag coding sequence was introduced into the pVL1392 transfer vector. Linearized baculovirus DNA (BaculoGold, Pharmingen) and the constructed pVL1392 transfer vector containing the prestin cDNA were co-transfected into Sf9 insect cells using Lipofectin Reagent (Invitrogen). The recombinant baculovirus was then amplified. Sf9 cells plated onto a 35-mm plate with 2 ml of fresh medium were infected with amplified baculovirus. After incubation for 3 days, cells were harvested and the expression of prestin in Sf9 cells was examined by Western blotting with anti-His<sub>6</sub> antibody.

For the mammalian expression system, the pIRES-hrGFP-1a (Stratagene, La Jolla, CA) mammalian expression vector was used. The open reading frame of the prestin cDNA was fused in the frame with the FLAG-tag of the expression vector. CHO-K1 cells (provided by the Cell Resource Center for Biomedical Research, Tohoku University) were transfected with the constructed expression vector using LipofectAMINE 2000 Reagent (Invitrogen). Transfected CHO cells were cultured in RPMI-1640 medium with 10% fetal bovine serum, 100 U penicillin/ml and 100 µg streptomycin/ml at 37°C with 5% CO<sub>2</sub> for 2 days, and the expression of prestin in CHO cells was then examined by Western blotting with anti-FLAG antibody (Sigma-Aldrich, St. Louis, MO).

When Western blotting was performed, cell proteins were separated on 10% SDS-polyacrylamide gel and electroblotted onto nitrocellulose membrane. After blocking with skim milk, membranes were incubated with the primary antibody described above. Bands were visualized using horseradish peroxidase-conjugated secondary antibody and the ECL Western blotting detection system (Amersham Pharmacia Biotech, Buckinghamshire, UK). Signals were recorded with a luminescent image analyzer (LAS-1000, Fuji Film, Tokyo, Japan).

## 2.2 Cloning of prestin-expressing CHO cells

As prestin was expressed in CHO cells, an attempt was made to generate stable prestin-expressing cell lines using CHO cells. Wild-type prestin cDNA or C-terminal FLAG-tagged prestin cDNA contained in the pIRES-hrGFP-1a mammalian expression vectors was transfected into CHO cells using LipofectAMIN 2000 Reagent. After transfection, cells were plated out at a density of one cell/well in 96-well tissue culture plates. Plates were incubated at 37°C with 5% CO<sub>2</sub>. Single colonies contained in 96-well plates were scaled up. Clones with slow growth were discarded. As the pIRES-hrGFP-1a vector includes the green fluorescent protein (GFP) gene, transfected clones were chosen based on the fluorescence of GFP using a fluorescent microscope.

## 2.3 Deglycosylation treatment

To evaluate N-linked glycosylation of prestin expressed in the generated CHO cell lines, cells were treated with PNGase F (New England Biolabs) according to the manufacturer's instructions. The molecular mass of deglycosylated prestin and that of untreated prestin were analyzed by Western blotting.

## 2.4 Immunofluorescence experiments

To confirm the localization of FLAG-tagged prestin in the generated cell lines, immunofluorescence experiments were performed. CHO cells transfected with FLAG-tagged prestin and untransfected CHO cells were fixed with 4% paraformaldehyde in phosphate buffer for 5 min at room temperature and washed with PBS. The samples were then incubated with skim milk and fetal bovine serum for 30 min at 37°C. After PBS washing, cells were incubated with anti-FLAG primary antibody in PBS with 0.1% saponin solution for 1 hour at 37°C. The samples were then washed with PBS and incubated with TRITC-conjugated anti-mouse IgG secondary antibody (Sigma-Aldrich) in PBS containing 0.1% saponin solution for 30 min at 37°C. Finally, the samples were washed with PBS, and immunofluorescence images of the samples were obtained using a confocal laser scanning microscope (LSM-GB200, Olympus, Tokyo, Japan).

## 2.5 Functional analysis of the generated cell lines

To confirm the activity of prestin expressed in the generated cell lines, the electrophysiological properties of these cell lines were measured. Patch pipettes for whole-cell patch-clamp recordings were pulled from glass capillaries with a puller (PP-830, Narishige). Patch pipettes had a resistance of 2-3 M $\Omega$  when filled with an internal solution composed of 140 mM KCl, 3.5 mM MgCl<sub>2</sub>, 5 mM EGTA, 5 mM HEPES, 0.1 mM CaCl<sub>2</sub> and 2.5 mM Na<sub>2</sub>ATP, adjusted to pH 7.3. The bath solution contained 145 mM NaCl, 5.8 mM KCl, 1.3 mM CaCl<sub>2</sub>, 0.9 mM MgCl<sub>2</sub>, 10 mM HEPES, 0.7 mM Na<sub>2</sub>HPO<sub>4</sub> and 5.6 mM glucose, adjusted to pH 7.3.

A block diagram of the measurement system is shown in Fig. 1. This system consisted of a patch amplifier (Axopatch 200B, Axon Instruments, Foster City, CA), an A/DD/A converter (Digidata 1320A, Axon Instruments), a personal computer and a function generator (WF1944, NF Electronic Instruments, Kanagawa, Japan). Measurements of cell capacitance were performed using the membrane test feature of pCLAMP 8.0 acquisition software (Axon Instruments). A test square wave (amplitude, 20 mV; period  $T = 4$  msec, i.e., frequency, 250 Hz) was generated by the personal computer controlled by pCLAMP 8.0 software and applied to the cell through the amplifier. The transient current, which is caused by the test square wave, was then sampled through the amplifier. Transient current  $Q$ , current decay  $\tau$  and total resistance  $R_t$  were continuously calculated by pCLAMP 8.0 software at a resolution of 25 Hz, by averaging the responses to 10 positive and 10 negative consecutive test steps, and measured values of these parameters were stored in the computer. Access resistance  $R_a$ , membrane resistance  $R_m$  and membrane capacitance  $C_m$  were then obtained by substituting  $Q$ ,  $\tau$  and  $R_t$  into the following equations (Huang and Santos-Sacchi, 1993):

$$R_a = \frac{R_t \tau V_c}{QR_t + \tau V_c}, \quad (1)$$

$$R_m = R_t - R_a, \quad (2)$$

$$C_m = \left( \frac{R_t}{R_m} \right)^2 \frac{Q}{V_c}, \quad (3)$$

where  $V_c$  is a voltage step. To determine the voltage dependence of membrane capacitance, triangular voltage ramps were superimposed on the above-mentioned square test wave. This triangular voltage wave (period  $T = 2$  sec) was generated by the function generator and swung the cell potential from  $-140$  mV to  $+70$  mV [16].

After the measurements, the membrane capacitance was plotted versus the membrane potential. The membrane capacitance was fitted to the derivative of a Boltzmann function [17],

$$C_m(V) = C_{lin} + \frac{Q_{max}}{\alpha e^{\frac{V-V_{1/2}}{\alpha}} \left( 1 + e^{-\frac{V-V_{1/2}}{\alpha}} \right)^2}, \quad (4)$$

where  $C_{lin}$  is the linear capacitance,  $Q_{max}$  is the maximum charge transfer,  $V$  is the membrane potential,  $\alpha$  is the slope factor of the voltage dependence of the charge transfer and  $V_{1/2}$  is the voltage at half-maximal charge transfer. When the membrane capacitance of the cell was fitted to Eq. (4) with the correlation coefficient  $R \geq 0.98$ , the cell was defined as showing nonlinear capacitance.

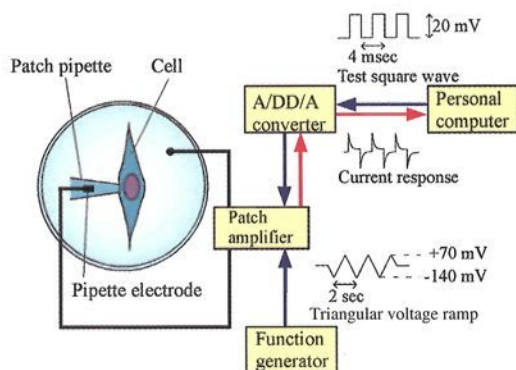


Figure 1. Block diagram of the measurement system. This system consisted of a patch amplifier, an A/DD/A converter, a personal computer and a function generator. Test square waves and triangular voltage ramps were generated by the personal computer and function generator, respectively. These waves were superimposed and applied to the cell through the amplifier. The transitional current was then measured and the membrane capacitance was calculated from this current.

### 3 Results

#### 3.1 Prestin expression in cells

Prestin cDNA was introduced into *E. coli*, Sf9 insect cells and CHO cells, and the expression of prestin was examined by Western blotting. Prestin has a predicted molecular weight of 81.4 kDa. The results of Western blotting used to assay the expression of prestin are shown in Fig. 2. When the *E. coli* expression system was employed, bands, which show the expression of prestin, were not detected, although three kinds of expression vectors were used for transformation. By contrast, when the baculovirus expression system was used, a band around 65 kDa and some weak bands below that were detected in transfected cells, but no band was detected in untransfected cells. When the CHO cell expression system was used, a strong, broad band around 90 kDa was detected in transfected cells, and bands around 30 kDa were detected in both untransfected cells and transfected cells. These results indicate that the prestin is expressed well in CHO cells. An attempt was therefore made to construct stable prestin-expressing cell lines using transfected CHO cells.

#### 3.2 Generation of prestin-expressing CHO cell lines

Transfected CHO cells were plated out into 96 wells. In the case of CHO cells transfected with wild-type prestin, 26 wells contained a single colony, the growth of 22 of them being good. In two of their clones, it was confirmed by fluorescence observation that all cells expressed GFP. In the case of CHO cells transfected with FLAG-tagged prestin, 21 wells contained a single colony, the growth of 13 of them being good. In two of their clones, it was confirmed by fluorescence observation that all cells expressed GFP. These four clones were then passaged over 40 times for four months, examination revealing that they retained the expression of the GFP. One of the obtained wild-type prestin-expressing cell lines and one of the FLAG-tagged prestin-expressing cell lines were then used for the following analysis.

### 3.3 Expression and glycosylation of prestin in generated cell lines

Expression and N-linked glycosylation of prestin in generated cell lines were examined by Western blotting (Fig. 3). When cells were untreated with PNGase F, which is an enzyme that removes N-linked carbohydrates, a broad band around 90 kDa was detected. By contrast, when cells were treated with PNGase F, the band around 90 kDa disappeared and a new band around 65 kDa appeared.

### 3.4 Localization of prestin in generated cell lines

The localization of FLAG-tagged prestin in generated cells was examined by immunofluorescence experiments. Results are shown in Fig. 4. The plasma membrane of 83% of the generated cells was stained. By contrast, untransfected cells were not stained.

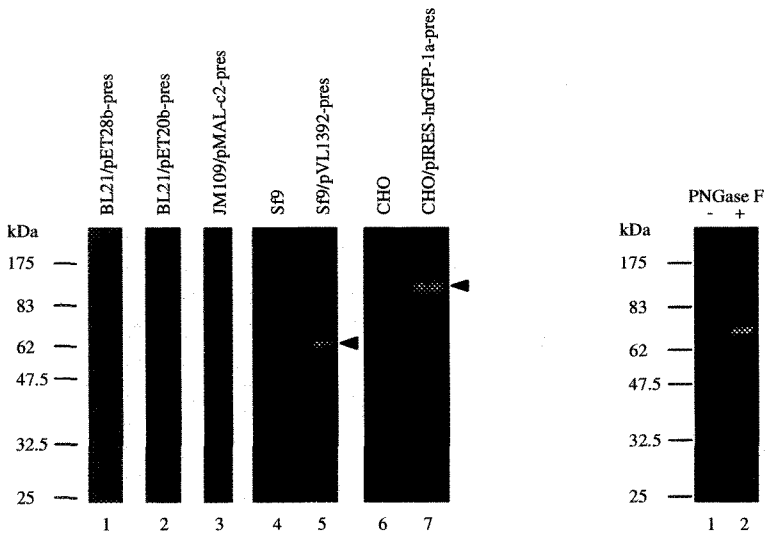


Figure 2. Expression of prestin examined by Western blot analysis. Lane 1: *E. coli* BL21 transformed with the pET28b vector containing prestin cDNA. Lane 2: *E. coli* BL21 transformed with the pET20b vector containing prestin cDNA. Lane 3: *E. coli* JM109 transformed with the pMAL-c2 vector containing prestin cDNA. Lane 4: Untransfected Sf9 insect cells. Lane 5: Sf9 insect cells transfected with the pVLI392 vector containing prestin cDNA. Lane 6: Untransfected CHO cells. Lane 7: CHO cells transfected with the pIRES-hrGFP-1a vector containing prestin cDNA. Arrows indicate the prestin bands. Bands were not detected using the *E. coli* expression system. By contrast, bands showing prestin were detected when a baculovirus expression system or a mammalian expression system was used.

Figure 3. Western blot of FLAG-tagged prestin-transfected CHO cells with or without PNGase F digestion. Lane 1: Untreated cells. Lane 2: Cells treated with PNGase F.

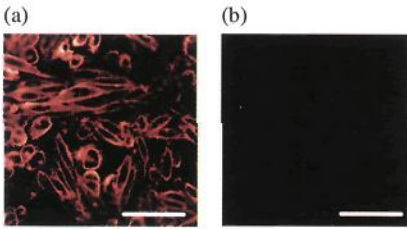


Figure 4. Immunofluorescence images. (a) FLAG-tagged prestin transfected CHO cell line. (b) Untransfected CHO cells. Fluorescent stains were observed in the transfected cell line after four months of subculture. By contrast, untransfected cells were not stained. Scale bars are 50  $\mu$ m.

### 3.5 Activity of prestin expressed in generated cell lines

After the expression of prestin was confirmed by immunofluorescence staining, the activity of prestin expressed in the generated cell lines was examined by patch-clamp measurements. Before obtaining the electrophysiological properties of CHO cells, those of OHCs of guinea pig were measured. They exhibited bell-shaped nonlinear membrane capacitance in response to ramping of the transmembrane voltage (Fig. 5). This nonlinear membrane capacitance was well fitted to a derivative of a Boltzmann function (Eq. (4)). In a group of 11 cells, the fitting parameters of Eq. (4) were obtained as  $C_{lin} = 26.8 \pm 3.7$  pF,  $Q_{max} = 2.88 \pm 0.65$  pC,  $\alpha = 28.4 \pm 2.3$  mV and  $V_{1/2} = -40.1 \pm 9.5$  mV (mean  $\pm$  SD) (Table 1).

The electrophysiological properties of wild-type prestin-expressing CHO cells and those of FLAG-tagged prestin-expressing CHO cells were then measured. The membrane capacitance versus membrane potential measured in a wild-type prestin-expressing CHO cell and that measured in a FLAG-tagged prestin-expressing CHO cell are shown in Fig. 6(a) and (b), respectively. As shown in these figures, wild-type prestin-expressing cells and FLAG-tagged prestin-expressing cells exhibited bell-shaped nonlinear membrane capacitance fitted to Eq. (4). In the case of wild-type prestin-expressing cells, 20 of 57 randomly measured cells showed nonlinear membrane capacitance, the fitting parameters of Eq. (4) being obtained as  $C_{lin} = 19.7 \pm 4.1$  pF,  $Q_{max} = 75.5 \pm 37.3$  fC,  $\alpha = 38.1 \pm 4.8$  mV and  $V_{1/2} = -74.8 \pm 11.6$  mV (mean  $\pm$  SD) (Table 1). In the case of FLAG-tagged prestin-expressing cells, 19 of 53 randomly measured cells showed nonlinear membrane capacitance, the fitting parameters of Eq. (4) being obtained as  $C_{lin} = 24.5 \pm 8.3$  pF,  $Q_{max} = 101.3 \pm 51.9$  fC,  $\alpha = 38.0 \pm 5.5$  mV and  $V_{1/2} = -73.0 \pm 12.9$  mV (mean  $\pm$  SD) (Table 1). By contrast, untransfected cells ( $n = 21$ ) did not exhibit nonlinear membrane capacitance (Fig. 6(c)).

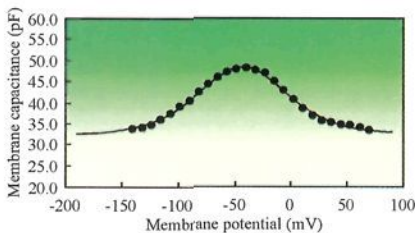


Figure 5. Representative data of the voltage dependent membrane capacitance of a guinea pig OHC. Data points are fitted to Eq. (4), which is shown by the solid line. Fitting parameters are  $C_{lin} = 33.1$  pF,  $Q_{max} = 2.33$  pC,  $\alpha = 28.0$  mV and  $V_{1/2} = -40.3$  mV.



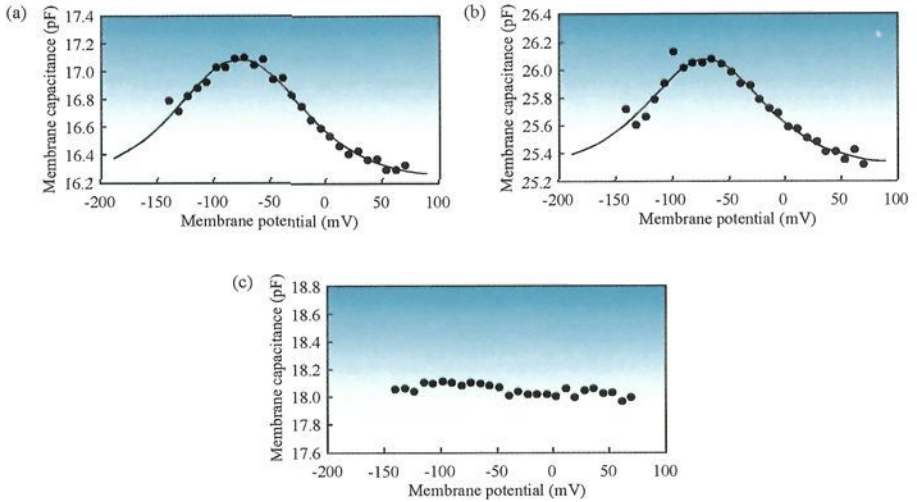


Figure 6. Representative data of the measured membrane capacitance versus membrane potential. (a) Membrane capacitance of a wild-type prestin-expressing CHO cell. Data points are fitted to Eq. (4), which is shown by the solid line, with the following parameters:  $C_{lin} = 16.2$  pF,  $Q_{max} = 127.1$  fC,  $\alpha = 36.8$  mV and  $V_{1/2} = -76.9$  mV. (b) Membrane capacitance of a FLAG-tagged prestin-expressing CHO cell. Data points were fitted to Eq. (4), which is shown by the solid line, with the following parameters:  $C_{lin} = 25.3$  pF,  $Q_{max} = 103.6$  fC,  $\alpha = 33.8$  mV and  $V_{1/2} = -70.4$  mV. (c) Membrane capacitance of an untransfected CHO cell.

Table 1. Fitting parameters of the derivative of a Boltzmann function and charge density.

	$C_{lin}$ (pF)	$Q_{max}$ (fC)	$\alpha$ (mV)	$V_{1/2}$ (mV)	Charge density ( $\mu\text{m}^{-2}$ )
OHC ( $n = 11$ )	$26.8 \pm 3.7$	$2,878 \pm 653$	$28.4 \pm 2.3$	$-40.1 \pm 9.5$	$6,830 \pm 1,910$
Wild-type prestin-expressing CHO cells ( $n = 20$ )	$19.7 \pm 4.1$	$75.5 \pm 37.3$	$38.1 \pm 4.8$	$-74.8 \pm 11.6$	$246 \pm 125$
FLAG-tagged prestin-expressing CHO cells ( $n = 19$ )	$24.5 \pm 8.3$	$101.3 \pm 51.9$	$38.0 \pm 5.5$	$-73.0 \pm 12.9$	$255 \pm 88$

## 4 Discussion

To obtain a large amount of prestin, we attempted to construct an expression system for prestin using *E. coli*, insect cells and CHO cells. Neither *E. coli* nor insect cells expressed prestin well. By contrast, prestin was found to be expressed in CHO cells. As the composition and constitution of the membrane of *E. coli* are generally recognized to be quite different from those of the mammalian plasma membrane, we



did not expect prestin to be expressed in the membrane of *E. coli*. We alternatively expected that prestin, which is a hydrophobic membrane protein, would be expressed as an inclusion body using the pET28b expression vector or as a solubilized protein fused with hydrophilic maltose-binding protein using the pMAL-c2 expression vector. Contrary to expectations, however, prestin was not expressed in these cells at all. Proteins expressed in *E. coli* differ from those in mammalian cells. Thus, it is presumed that prestin is not expressed in *E. coli* because some kinds of proteins which essentially interact with prestin are not expressed in *E. coli*. Alternatively, there is a possibility that prestin is toxic for *E. coli*.

By Western blot analysis (Fig. 2), when the CHO expression system was used, a broad band around 90 kDa representing prestin was detected in transfected cells (lane 7). Bands around 30 kDa detected in both transfected CHO cells (lane 7) and untransfected CHO cells (lane 6) may have resulted from nonspecific binding of antibodies. As shown in Fig. 3, when cells were treated with PNGase F (lane 2), a band around 90 kDa, which was detected in untreated cells (lane 1), disappeared and a new band around 65 kDa appeared. This result suggests that prestin expressed in CHO cells is glycosylated. As prestin expressed in CHO cells is modified by different lengths of carbohydrate chains leading to variation of molecular weight, the band detected in untreated CHO cells is broad. The idea that prestin is glycosylated in CHO cells agrees with findings of a glycosylation study of prestin [18]. Although prestin without carbohydrate chains has a predicted molecular weight of 81.4 kDa, the band of deglycosylated prestin was detected around 65 kDa. A possible explanation for this disagreement is related to the hydrophobicity of prestin. When SDS-PAGE was carried out, more SDS may have bound to prestin compared to the case of average soluble proteins because prestin is a hydrophobic membrane protein. As a result, prestin may have migrated through the polyacrylamid gel faster than average soluble proteins.

As shown in Fig. 2, when the baculovirus expression system was used, a band around 65 kDa and some weak bands below that were detected in transfected Sf9 cells (lane 5), while no band was detected in untransfected cells (lane 4). The position of the highest band was almost same as that of the band of deglycosylated prestin detected in Fig. 3. This result indicates that prestin expressed in Sf9 cells is not glycosylated. The other lower bands are likely to represent fragments of prestin. In Fig. 2, the fact that the band detected in CHO cells was brighter than that detected in Sf9 cells suggests that prestin is highly expressed in CHO cells due to its stabilization realized by glycosylation.

In our experimental results, prestin was not expressed in *E. coli* at all and only slightly expressed in insect cells. However, since few attempts were made to express prestin in insect cells and bacterial cells, there is a possibility that it could be expressed in such cells using other host vector systems. Even though there are other possibilities to obtain prestin, we adopted the CHO cell expression system because prestin was well expressed in CHO cells.

Transfected cell lines were obtained by limiting dilution cloning, and GFP was stably expressed for over four months in these cell lines. As the prestin gene and the GFP gene are transcribed into sequential mRNA when the constructed expression vector is used, stable expression of prestin may be achieved in these cell lines. In fact, according to the results of Western blotting (Fig. 3) and immunofluorescence experiments (Fig. 4), it was confirmed that FLAG-tagged prestin was stably expressed in the generated cell line after subculturing for four months. As the same expression vector was applied, it was anticipated that wild-type prestin was also stably expressed in the generated cell line. We therefore considered that the stable prestin-expressing cell lines have been established using transfected CHO cells.

The electrophysiological properties of the OHCs measured in this study agree with those of OHCs reported by Huang and Santos-Sacchi [8], and the electrophysiological properties of prestin-expressing CHO cells, which were subcultured for over four months and measured in this study, agree with those of transiently prestin-expressing CHO cells [10]. As both the established wild-type prestin-expressing and FLAG-tagged prestin-expressing cell lines exhibited bell-shaped nonlinear membrane capacitance fitted to Eq. (4), similar to prestin in the OHCs, wild-type prestin and FLAG-tagged prestin expressed in the established cell lines have activity. Moreover, as there were no significant differences between the electrophysiological properties of wild-type prestin-expressing cells and those of FLAG-tagged prestin-expressing cells, it is concluded that the FLAG-tag does not interfere with the function of prestin (Table 1).

Nonlinear membrane capacitance was not obtained in about half of the transfected cells. The reason for this result may have been individual differences in the expression level of prestin in the transfected cells. When the expression level of prestin was low, it was difficult to obtain nonlinear membrane capacitance which fitted Eq. (4) with a correlation coefficient of  $R \geq 0.98$  because the measured membrane capacitance was affected by measurement noise. If measurement noise were decreased, more cells would show nonlinear capacitance. Although about half of the transfected cells do not show nonlinear capacitance, i.e., the expression level of prestin in some cells is low, it does not interfere with obtaining prestin from those cells.

The expression level of prestin in the established cell line was then estimated using the obtained linear capacitance,  $C_{in}$ , and the maximum charge transfer,  $Q_{max}$ . As  $Q_{max}$  indicates the total amount of charge carried by all prestin in the plasma membrane and  $e$  is electron charge, which is presumed to equal the charge carried by one prestin molecule, the number of prestin molecules in the cell is given by  $Q_{max}/e$ . As  $C_{in}$  expressed in picofarads indicates the total capacitance of the plasma membrane of the cell, and the membrane capacitance of the cell per unit surface area is known to be  $0.01 \text{ pF}/\mu\text{m}^2$  [19], the surface area of the cell is expressed by  $C_{in}/0.01 \mu\text{m}^2$ . The expression level of prestin per unit surface area, i.e., charge density, of the cell can therefore be obtained with

$$\text{Charge density} = \frac{Q_{\max}}{e} \bigg/ \frac{C_{\text{lin}}}{0.01} . \quad (5)$$

The charge density of the 20 measured wild-type prestin-expressing CHO cells and 19 measured FLAG-tagged prestin-expressing CHO cells were determined to be  $246 \pm 125/\mu\text{m}^2$  and  $255 \pm 88/\mu\text{m}^2$ , respectively (Table 1). The charge densities of established cell lines are lower than the average density of OHCs, which is  $6830/\mu\text{m}^2$  as obtained in this study or  $7500/\mu\text{m}^2$  as reported by Huang and Santos-Sacchi [8]. The charge densities are also lower than that of transiently prestin-expressing TSA201 cells, reported to be  $5360/\mu\text{m}^2$  [9]. Although the expression levels were 1/20-1/35 of those in OHCs and TSA201 cells, the stable expression of prestin in the established cell lines is an advantage.

## 5 Conclusions

In this study, to obtain a large amount of prestin, an expression system for prestin was constructed. The conclusions are as follows:

1. Glycosylated prestin is expressed in mammalian cells, but not in *E. coli* nor in insect cells.
2. Prestin-expressing cell lines can be generated by limiting dilution cloning.
3. In established cell lines, although the expression levels are about 1/20-1/35 of those in OHCs and TSA201 cells transiently expressing prestin, prestin is expressed stably in the generated cell lines.

## Acknowledgments

This work was supported by Grant-in-Aid for Scientific Research on Priority Areas 15086202 from the Ministry of Education, Culture, Sports, Science and Technology of Japan, by a Health and Labour Science Research Grant from the Ministry of Health, Labour and Welfare of Japan, by a grant from the Human Frontier Science Program, and by the 21st Century COE Program Special Research Grant of the "Future Medical Engineering Based on Bio-nanotechnology."

## References

1. Brownell, W.E., Bader, D., Ribaupierre, Y., 1985. Evoked mechanical responses of isolated cochlear outer hair cells, *Science* 227, 194-196.
2. Kachar, B., Brownell, W.E., Altschuler, R., Fex, J., 1986. Electrokinetic shape changes of cochlear outer hair cells, *Nature* 322, 365-368.

3. Zenner, H.P., 1986. Motile responses in outer hair cells, *Hear. Res.* 22, 83-90.
4. Ashmore, J.F., 1987. A fast motile response in guinea-pig outer hair cells: the cellular basis of the cochlear amplifier, *J. Physiol.* 388, 323-347.
5. Santos-Sacchi, J. and Dilger, J.P., 1988. Whole cell currents and mechanical responses of isolated outer hair cells, *Hear. Res.* 35, 143-150.
6. Dallos, P., 1992. The active cochlea, *J. Neurosci.* 12, 4575-4585.
7. Forge, A., 1991. Structural features of the lateral walls in mammalian cochlea outer hair cells, *Cell Tissue Res.* 265, 473-485.
8. Huang, G., Santos-Sacchi, J., 1993. Mapping of the distribution of the outer hair cell motility voltage sensor by electrical amputation, *Biophys. J.* 65, 2228-2236.
9. Zheng, J., Shen, W., He, D.Z.Z., Long, K.B., Madison, L.D., Dallos, P., 2000. Prestin is the motor protein of cochlear outer hair cells, *Nature* 405, 149-155.
10. Ludwig, J., Oliver, D., Frank, G., Klöcker, N., Gummer, A.W., Fakler, B., 2001. Reciprocal electromechanical properties of rat prestin: the motor molecule from rat outer hair cells, *Proc. Natl. Acad. Sci. USA* 98, 4178-4183.
11. Santos-Sacchi, J., Shen, W., Zheng, J., Dallos, P., 2001. Effects of membrane potential and tension on prestin, the outer hair cell lateral membrane motor protein, *J. Physiol.* 531, 661-666.
12. Zheng, J., Long, K.B., Shen, W., Madison L.D., Dallos, P., 2001. Prestin topology: localization of protein epitopes in relation to the plasma membrane, *NeuroReport* 12, 1929-1935.
13. Oliver, D., He, D.Z.Z., Klöcker, N., Ludwig, J., Schulte, U., Waldegger, S., Ruppersberg, J.P., Dallos, P., Fakler, B., 2001. Intracellular anions as the voltage sensor of prestin, the outer hair cell motor protein. *Science* 292, 2340-2343.
14. Liberman, M.C., Gao, J., He, D.Z.Z., Wu, X., Jia, S., Zuo, J., 2002. Prestin is required for electromotility of the outer hair cell and for the cochlear amplifier, *Nature* 419, 300-304.
15. Wu, X., Gao, J., Guo, Y., Zuo, J., 2004. Hearing threshold elevation precedes hair-cell loss in prestin knockout mice, *Mol. Brain Res.* 126, 30-37.
16. Frolenkov, G.I., Mammano, F., Belyantseva, I.A., Coling, D., Kachar, B., 2000. Two distinct  $Ca^{2+}$ -dependent signaling pathways regulate the motor output of cochlear outer hair cells, *J. Neurosci.* 20, 5940-5948.
17. Santos-Sacchi, J., 1991. Reversible inhibition of voltage-dependent outer hair cell motility and capacitance, *J. Neurosci.* 11, 3096-3110.
18. Matsuda, K., Zheng, J., Du, G.G., Klöcker, N., Madison, L.D., Dallos, P., 2004. N-linked glycosylation sites of the motor protein prestin: effects on membrane targeting and electrophysiological function, *J. Neurochem.* 89, 928-938.
19. Neher, E., Marty, A., 1982. Discrete changes of cell membrane capacitance observed under conditions of enhanced secretion in bovine adrenal chromaffin cells, *Proc. Natl. Acad. Sci. USA* 79, 6712-6716.

# EFFECTS OF ACTIN FILAMENTS ON ANISOTROPY AND STIFFNESS OF AORTIC SMOOTH MUSCLE CELLS

T. MATSUMOTO AND K. NAGAYAMA

*Department of Mechanical Engineering, Nagoya Institute of Technology,  
Gokiso-cho, Showa-ku, Nagoya 466-8555, Japan  
E-mail: takeo@nitech.ac.jp*

Actin filaments have been reported to be ~1000 times stiffer than whole cells. Thus, they must play major roles in mechanical properties of cells. Effects of actin filament distribution and alignment on anisotropy and stiffness were studied on rat aortic smooth muscle cells. Freshly isolated cells (FSMCs), cultured cells (CSMCs), and CSMCs treated with cytochalasin D to disrupt their actin filaments (CSMCs-CYD) were stretched with an originally designed micro tensile tester. FSMCs were stretched in their major and minor axes directions to evaluate their anisotropy. The normalized stiffness of FSMCs was significantly higher in the major axis ( $14.8 \pm 4.3$  kPa, mean  $\pm$  SEM,  $n=5$ ) than the minor axis ( $2.8 \pm 1.0$  kPa,  $n=5$ ). Long and thick fibers of actin filament were found running almost parallel to the major axis of the cells, indicating increased stiffness in this direction. CSMCs and CSMCs-CYD were stained for actin filament after the tensile test while they remained attached to the tester. Relative concentration of the actin filament in the central region of the cell  $F$  had significant positive correlation with normalized stiffness in both cells. These results indicate that elastic properties of smooth muscle cells are affected not only by the amount of their actin filaments, but also by their organization and distribution in cells.

## 1 Introduction

Cytoskeletal structures, such as actin filaments have a close correlation with mechanical properties of cells [1, 2]. One of the main reasons would be that cytoskeletons were much stiffer than whole cells. For example, Young's modulus of actin filaments has been reported to be 1.8 GPa for single fibers [3] and 3 MPa for bundles [4], while that of whole cell on the order of 1 to 10 kPa for aortic smooth muscle cells [5–8]. Thus, the actin filaments are several orders of magnitude stiffer than whole cells. Not only their amount but also their distribution and alignment must have close correlation with the elastic properties of whole cells.

In this section, we would like to introduce our recent results on the effect of actin filaments on mechanical properties of rat aortic smooth muscle cells (SMCs): 1) effects of actin filament alignment on the anisotropy of cells [7], and 2) effects of actin filament distribution on the cell stiffness [8].

To study the anisotropy of cells, we used SMCs freshly isolated from rat thoracic aortas by enzymatic digestion. SMCs are spindle-shaped and aligned almost parallel to the circumferential direction in the arterial wall. Their intracellular contractile apparatus, such as actin filaments and myosin filaments, run mostly parallel to their major axis, and their contraction takes place in that direction.

Thus, they may be stiffer in their major axis direction than in other directions. To check this hypothesis, we measured tensile properties of freshly isolated SMCs (FSMCs) in their major and minor axis directions using a cell tensile tester developed in our laboratory [7]. We also used FSMCs treated with  $10^{-5}$ M serotonin to induce their contraction, measured the tensile properties of the contracted cells in their major and minor axis directions, and examined the effect of cell contraction on the anisotropy of cells. We also observed the morphology of actin filaments in both untreated and contracted FSMCs to investigate the effect of actin filament morphology on the mechanical anisotropy of FSMCs.

For the study on the actin filament distribution, we measured the tensile properties of cultured SMCs, and cultured SMCs whose actin filament network was disrupted with cytochalasin D, and examined the effect of actin filament on the static tensile properties of SMCs quantitatively [8]. The actin filament morphology, such as their length, thickness, orientation, organization and distribution are different from cell to cell. We thus need to observe the intracellular actin filaments of cells whose mechanical properties has been measured in the tensile test. For this purpose, we established an in process observation technique and observed the actin filament distribution in cultured cells while the cells were kept attached to the tester after the tensile test.

## 2 Materials and Methods

### 2.1 Preparation of freshly isolated smooth muscle cells (FSMCs)

All animal experiments and treatments were conducted in accordance with the *Guide for Animal Experimentation, Nagoya Institute of Technology*. Male Wistar rats (8–14 weeks of age) were killed by suffocation in a CO<sub>2</sub> chamber and their thoracic aortas were quickly excised. FSMCs were isolated from aortic tissue by enzymatic digestion [9]. Briefly, the excised aortas were placed in a 2 ml Ca<sup>2+</sup>-Mg<sup>2+</sup>-free Hank's balanced salt solution (HBSS(-), Sigma) at 37°C containing 300 U of collagenase type III (Worthington Biochemical) and 1.8 U of elastase type I (Sigma), and gently shaken at a rate of 50 cycle/min for 1.5 h. After the adventitia was separated, remaining tissues were placed into 2 ml of the fresh enzyme solution and shaken again for 0.5–1 h to yield an FSMC suspension. The cell suspension was filtered by a cell strainer (40µm Nylon, Falcon) to remove excess tissue, and diluted in HBSS(-) to about 1:10 to reduce the effect of the enzymes.

Cells were used for the tensile test within 3 hours of the dilution, and were stored at 4°C until they were used. Untreated FSMCs possessing an axial length of more than 20 µm and a smooth-looking surface were used for the tensile test of relaxed FSMCs. For contracted cells, they were treated with HBSS(-) containing  $10^{-5}$ M Ca<sup>2+</sup> and  $10^{-5}$ M serotonin (5-hydroxytryptamine, Sigma) at 37°C. The cells

completed their morphological changes (cell shortening and membrane bleb formation) within 20 min were used as contracted FSMCs.

## 2.2 Preparation of cultured smooth muscle cells (CSMCs and CSMCs-CYD)

SMCs cultured until 4–9th passage were used. They were harvested from the bottom of cell culture dish with 0.05% Trypsin–EDTA solution (Gibco), diluted in the HBSS(-) to about 1:10, and stored at 4°C. Thus harvested cells were called CSMCs and used for the tensile test within 3 hours after the trypsinization.

Actin filament networks were disrupted by treating CSMCs adhered on the cell culture dish with 2 µg/ml cytochalasin D (Sigma) for 1 h at 37°C. After the treatment, the cells were harvested with the trypsin and stored at 4°C as mentioned above. These cells were called CSMCs-CYD.

## 2.3 Tensile test

The cell tensile tester used for CSMCs and CSMCs-CYD was similar to that reported previously [5], which consisted of an upright microscope, a computer-controlled electric micromanipulator (MMS-77, Shimadzu), a manual micromanipulator (MHW-3, Narishige), and an analog CCD camera (TM1650B, Toshiba). For the measurement of FSMCs, we used a slightly modified setup: an inverted microscope (TE2000E, Nikon) and the cooled digital CCD camera were employed instead of an upright microscope and an analog CCD camera, respectively.

Cell holding method was similar for both setup (Fig. 1). An arm made from a glass micropipette, whose tip diameter was about 10 µm, was set on each micromanipulator. A cell culture dish containing the cell suspension was set on the microscope stage, whose temperature was controlled at 37°C, and waited for about 10 min until the temperature of the suspension reached the preset value. A cell in the dish was randomly selected and held with two glass micropipettes: an operation pipette and a deflection pipette. The cell was held by gently pressing onto its surface two pipettes that had been coated with a urethane resin adhesive (Sista M5250, Henkel) [10, 11]. An operation pipette was moved with the electric micromanipulator to stretch the cell horizontally. The tension applied to the cell was measured by the deflection of the cantilever part of the deflection pipette.

When the cell was stretched along its major axis, each of the glass micropipettes was gently pressed down on each end of the cell (Fig. 2). The cell was held gently on both sides with the two pipettes when stretched in the minor axis direction. After waiting for about 5 minutes to make the adhesion between the cell and the pipettes firm, we stretched the cell stepwise by moving the operation pipette 1 µm every 5 seconds until fracture occurred, or until the cell began to slip off from the pipette. The cell image was recorded during the stretch procedure via a CCD camera connected to a personal computer. Specimens were not preconditioned to eliminate possible stretch-induced contraction of the cells.

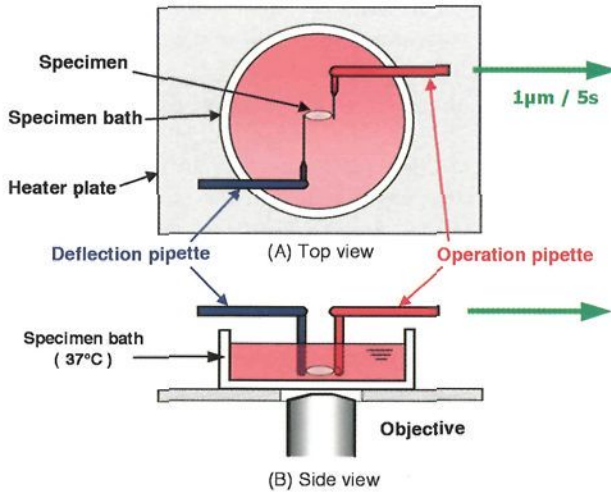


Figure 1. Schematic drawing of the test section of the tensile tester used for anisotropy analysis of FSMCs [7]. Upright microscope with similar setup was used for the measurement of CSMCs [8].

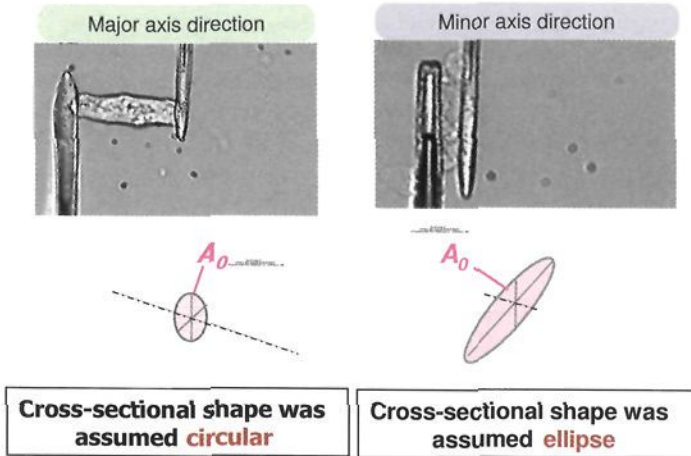


Figure 2. FSMCs held with a deflection pipette (left side of each cell) and an operation pipette (right side) and their schematic drawings with cross-section.

#### 2.4 Evaluation of mechanical properties of the cells

After the tensile test, we measured the distance between the two pipettes  $L$  and the displacement of the deflection pipette  $x$  on the recorded images. The tension applied to the cell  $T$  was calculated by multiplying  $x$  with the spring constant of the deflection pipette  $k$  measured after each experiment. The elongation of the cell  $\Delta L$



was calculated as the increment of  $L$ . To reduce the effect of cell dimension on mechanical properties, we normalized the tension  $T$  with the initial cross-sectional area of the cell  $A_0$ , as given by  $\sigma = T/A_0$ , and refer to it as normalized tension. When we estimated  $A_0$  for a cell stretched along its major axis, we calculated the initial diameter of the cell  $D_0$  by dividing the initial tracing area of the cell  $C_0$  with the initial distance between the two pipettes  $L_0$ , as given by  $D_0 = C_0/L_0$ , and assumed that the cell cross-sectional shape perpendicular to the stretch direction was circular, such that  $A_0 = \pi(D_0/2)^2$  (Fig. 2). We assumed that the cell cross-sectional shape perpendicular to the stretch direction in a cell stretched along the direction of its minor axis was an ellipse with major and minor diameters  $D_0^L$  and  $D_0^S$ , respectively. The initial major diameter  $D_0^L$  was calculated as  $D_0$ , as mentioned above, such that  $D_0^L = C_0/L_0$ . The initial minor diameter  $D_0^S$  was assumed to be equal to the initial distance between the two pipettes  $L_0$ . The nominal strain  $\varepsilon$  was obtained by normalizing the elongation  $\Delta L$  with the initial distance of the two pipettes  $L_0$ . Mechanical properties of the cells were evaluated with normalized tension–nominal strain ( $\sigma$ – $\varepsilon$ ) curves. The initial normalized stiffness  $E_{\text{ini}}$  was obtained by fitting a straight line from the origin to the low strain region ( $\varepsilon < 0.2$ ) of  $\sigma$ – $\varepsilon$  curves.

### 2.5 Observation of actin filament morphology

Actin filaments in both untreated and contracted FSMCs were stained with rhodamine-phalloidin. The cells in the culture dish were fixed with formaldehyde for 5 min, rinsed gently with plain PBS, treated with PBS containing 0.1% Triton X-100 (ICN Biomedicals) for 5 min, and stained with rhodamine-phalloidin (Molecular Probes) in PBS for 20 min at room temperature. Stained filaments were observed using an inverted microscope with a confocal laser scanning system (DIGITAL ECLIPSE C1, Nikon). Optically sectioned images (0.35–0.80  $\mu\text{m}$  steps) were collected and reconstructed to form a plane image.

Actin filaments were also observed in CSMCs and CSMCs-CYD while they were kept attached to the tester. The tensile test was terminated when the strain became within the range of 0.6–1.0, and the cell was immediately fixed and stained similarly. The operations were performed very carefully to avoid the cell detachment from the pipettes. The fluorescent image whose contrast of the cell periphery was the most clear was fed to the computer for each cell.

## 3 Results

Figure 3 shows the normalized tension–nominal strain curves of FSMCs. The relationship between the normalized tension and nominal strain was relatively linear along the major and minor axes in untreated cells, and so was in the major axis of contracted cells. In contrast, the contracted cells showed marked curvilinearity along their minor axis. In untreated cells, the slopes in the major axis looked steeper

than those in the minor axis. On the other hand, the slope of the curves in contracted cells seems to show little difference between major and minor axes.  $E_{ini}$  of untreated cells was significantly higher ( $P < 0.05$ , paired  $t$  test.) in the major axis ( $14.8 \pm 4.3$  kPa, mean  $\pm$  SEM,  $n = 5$ ) than in minor ( $2.8 \pm 1.0$  kPa,  $n = 5$ ), indicating that freshly isolated SMCs are anisotropic. In contracted cells,  $E_{ini}$  was significantly higher than that obtained for untreated cells in both directions, but the difference between the two directions was insignificant in contracted cells:  $E_{ini}$  was  $88.1 \pm 13.3$  kPa ( $n = 4$ ) and  $59.0 \pm 9.4$  kPa ( $n = 4$ ) for the major and minor axis, respectively. Actin filaments in untreated cells were observed as long and thick fibers running almost in parallel with the direction of the major axis (Fig. 4). The actin filaments in contracted cells looked entangled and possessed bulk-like structures, and appeared to exhibit no preferential direction.

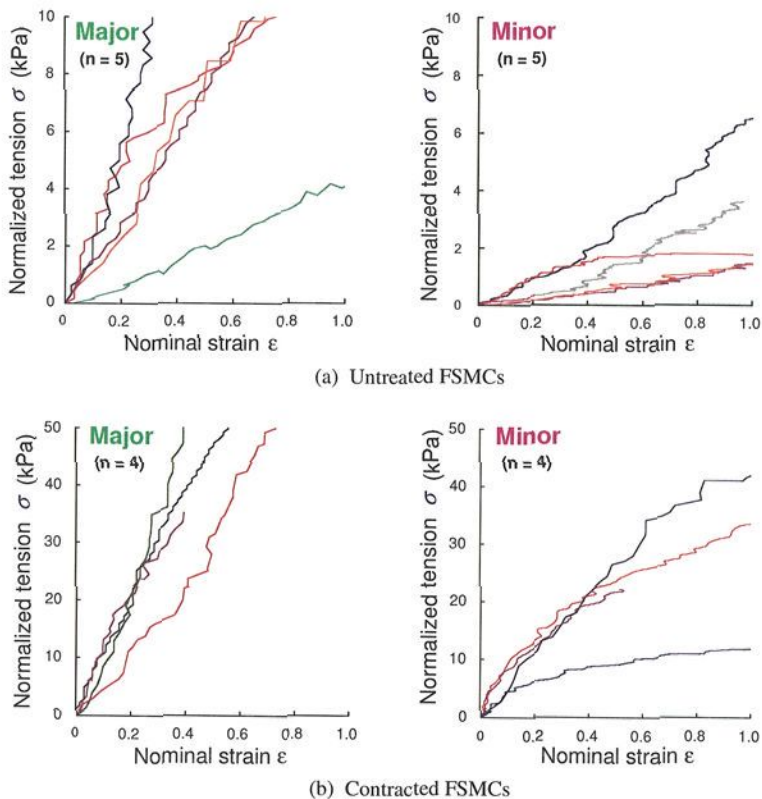


Figure 3. Normalized tension–nominal strain curves in major and minor axes of FSMCs. Please note that the full scale of ordinate is different between untreated and contracted cells [7].

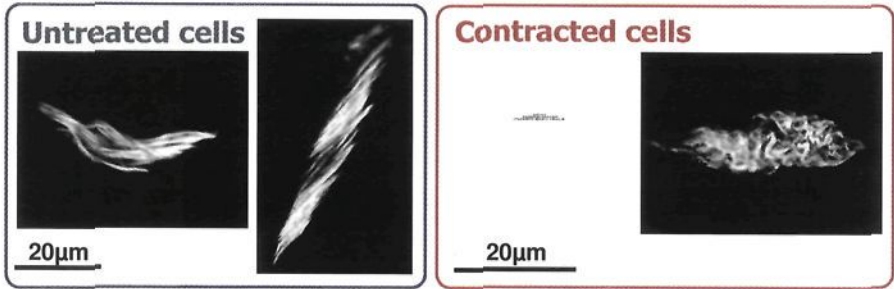


Figure 4. Examples of morphology of actin filaments in untreated and contracted FSMCs [7].

The examples of normalized tension–nominal strain curves of CSMCs and CSMCs-CYD were shown in Fig. 5. The slopes of the curves were more gradual in CSMCs-CYD than in CSMCs. The relationship between the normalized tension and nominal strain was relatively linear.  $E_{ini}$  was significantly lower in CSMCs-CYD ( $1.3 \pm 0.3$  kPa,  $n = 13$ ) than in CSMCs ( $3.4 \pm 0.7$  kPa,  $n = 21$ ). Examples of CSMCs and CSMCs-CYD stained for actin filaments are shown in Fig. 6. Although the cells were treated with the same protocol, their normalized stiffness was highly variable among them. In the fluorescent images, the actin filament distribution also looked variable, especially in their central region. To evaluate the effect of the difference of actin filament distribution on the mechanical properties of cells, we defined a normalized actin filament concentration in the central region of cell  $F$  (Fig. 7). We separated each of the cell image into 5 segments with equal length, measured average fluorescent intensity of each segment, and obtained the relative intensity of the central segment to that of all segments. There was a significant positive correlation between  $E_{ini}$  and  $F$  both in CSMCs and CSMCs-CYD. The slope of the regression line was much steeper in CSMCs than in CSMCs-CYD.

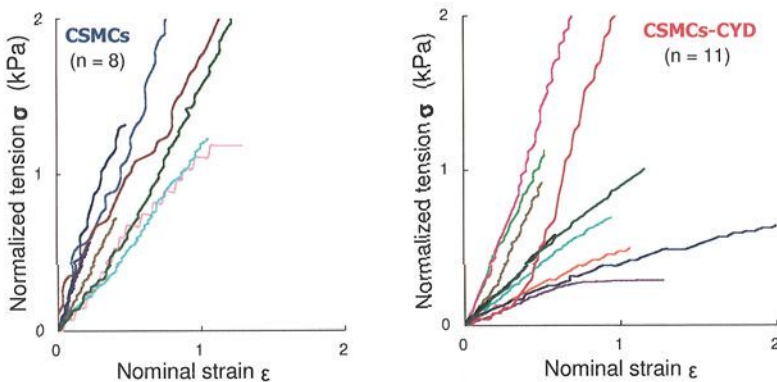


Figure 5. Examples of normalized tension–nominal strain curves of CSMCs and CSMCs-CYD.

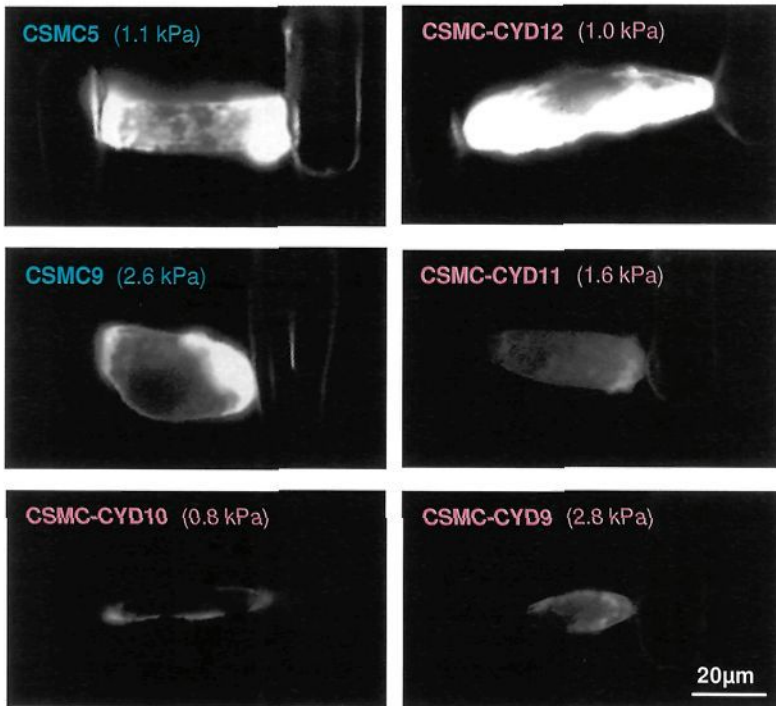


Figure 6. Examples of in-process staining of actin filaments in cultured rat aortic smooth muscle cells (CSMCs) and those treated with cytochalasin D (CSMCs-CYD). Length marker applied to all.

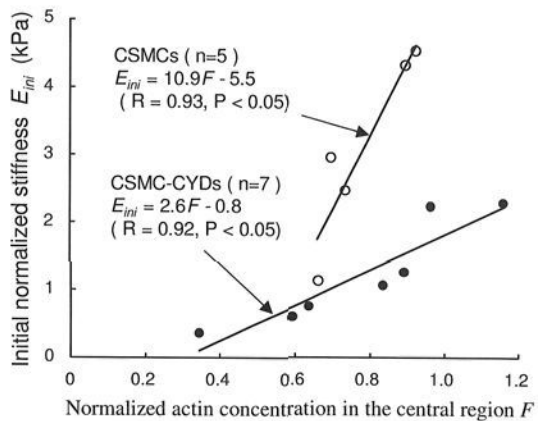
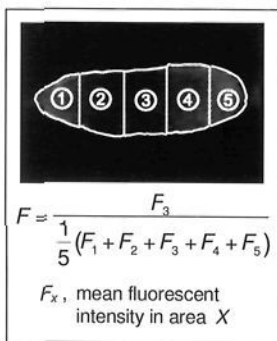


Figure 7. Definition of the normalized actin filament concentration in the central region of the cell (a), and relationship between the initial normalized stiffness  $E_{init}$  and normalized actin filament concentration in the central region  $F$ .

## 4 Discussion

In untreated FSMCs, the thick actin filament bundles were observed running almost parallel to their major axis direction (Fig. 4). When the cell was stretched along the major axis direction, the actin bundles of the cell may be able to resist the tension applied to the cell. When stretched in the minor axis direction, the actin bundles may not participate in resisting the tension. Thus, the cells may be softer when the stretch direction is perpendicular to the fiber direction. While in the contracted FSMCs, their anisotropy disappeared although the cells stiffened drastically both in their major and minor axis directions. The three-dimensional morphology of actin filaments in contracted FSMCs showed an aggregated structure without a preferential direction. Actin bundles formed in such a way may have no preferential direction. Thus, FSMCs may not only increase their stiffness, but also reduce their mechanical anisotropy.

With regard to cultured cells, the normalized actin filament concentration in the central region  $F$  had a positive correlation with their normalized stiffness both in the CSMCs and CSMCs-CYD (Fig. 7). In contrast, there was no significant correlation between the average fluorescent intensity of whole cells and their normalized stiffness as noted in Fig. 6. Caille *et al.* [12] measured the mechanical properties of the nucleus isolated from endothelial cells to find that the elastic modulus of the endothelial nucleus was on the order of 5 kPa, which was significantly higher than that of the cytoplasm (about 0.5 kPa). If there were a strong mechanical interaction between the actin filaments and nucleus, the relatively high elastic modulus of the nucleus may cause the stiffening of the cells whose actin filaments concentrated on their central region.

It would be also interesting to note that the slope of the regression line between  $E_{ini}$  and  $F$  in CSMCs and CSMCs-CYD was different. The reason for this difference may be due to the difference in actin filament morphology. The well organized actin filament network was observed in CSMCs, while the network was disrupted and looked like clusters following cytochalasin D treatment [7]. These results may indicate that not only actin filament distribution but also their organization has remarkable effect on the mechanical properties of the smooth muscle cells.

## Acknowledgments

We wish to thank Mr. Y. Nagano and Prof. M. Sato at Tohoku University for their superb researches adopted in this paper. This work was supported financially in part by Grants-in-Aids for Scientific Research 15086209 and 16360052 from the Ministry of Education, Culture, Sports, Science and Technology of Japan and the Tatematsu foundation.

**References**

1. Franke, R.P., Grafe, M., Schmittler, H., Seiffge, D., Mittermayer, C., Drenckhahn, D., 1984. Induction of human vascular endothelial stress fibers by fluid shear stress. *Nature* 307, 648-649.
2. Wang, H.C.J., Goldschmidt-Clermont, P., Willea, J., Yin, C.P.F., 2001. Specificity of endothelial cell reorientation in response to cyclic mechanical stretching. *J. Biomech.* 34, 1563-1572.
3. Kojima, H., Ishijima, A., Yanagida, T., 1994. Direct measurement of stiffness of single actin filaments with and without tropomyosin by in vitro nanomanipulation, *Proc. Natl. Acad. Sci. USA* 91, 12962-12966.
4. Deguchi, S., Ohashi, T., Sato, M., 2003. Single Stress Fibers Isolated from Vascular Smooth Muscle Cells Possess Surprisingly High Extensibility, *Proc. ASME Summer Bioengng. Conf.*, 833.
5. Matsumoto, T., Sato, J., Yamamoto, M., Sato, M., 2000. Smooth muscle cells freshly isolated from rat thoracic aortas are much stiffer than cultured bovine cell: Possible effect of phenotype. *JSME Int. J., Ser. C* 43, 867-874.
6. Miyazaki, H., Hasegawa, Y., Hayashi, K., 2002. Tensile properties of contractile and synthetic vascular smooth muscle cells. *JSME Int. J., Ser. C* 45, 870-879.
7. Nagayama, K., Matsumoto, T., 2004. Mechanical Anisotropy of Rat Aortic Smooth Muscle Cells Decreases with Their Contraction: Possible effect of actin filament orientation, *JSME Int. J., Ser. C* 47, 985-991.
8. Nagayama, K., Nagano, Y., Sato, M., Matsumoto, T., in press. Effect of Actin Filament Distribution on Tensile Properties of Smooth Muscle Cells Obtained from Rat Thoracic Aortas, *J. Biomechanics*.
9. Chamley, J., Campbell, G., McConnell, J., 1977. Comparison of vascular smooth muscle cells from adult human, monkey and rabbit in primary culture and in subculture. *Cell and Tissue Research* 177, 503-522.
10. Shue, G.H., Brozovich, F.V., 1999. The frequency response of smooth muscle stiffness during Ca<sup>2+</sup>-activated contraction. *Biophysical Journal* 76, 2361-2369.
11. Smith, P.G., Roy, C., Fisher, S., Huang, Q., Brozovich, F.V., 2000. Cellular responses to mechanical stress: Selected contribution: Mechanical strain increases force production and calcium sensitivity in cultured airway smooth muscle cells. *Journal of Applied Physiology* 89, 2092-2098.
12. Caille, N., Thoumine, O., Tardy, Y., Meister, J. J., 2002. Contribution of the nucleus to the mechanical properties of endothelial cells. *Journal of Biomechanics* 35, 177-187.

# MICRO-VESSEL NETWORK FORMATION OF ENDOTHELIAL CELLS WITH IN VITRO THREE DIMENSIONAL MODEL

K. TANISHITA, A. UEDA, M. KOGA, R. SUDO, S. KUDO AND M. IKEDA

*School of Fundamental Science and Technology, Keio University,*

*3-14-1 Hiyoshi, Kohoku-ku, Yokohama 223-8522, Japan*

*E-mail: tanishita@sd.keio.ac.jp*

Bovine pulmonary microvascular endothelial cells were seeded onto collagen gels with basic fibroblast growth factor (bFGF) to make a micro-vessel formation model. We observed this model in detail using phase contrast microscopy, confocal laser scanning microscopy and electron microscopy. The results show that cells invaded the collagen gel and reconstructed the tubular structures, containing a clearly defined lumen consisting of multiple cells. The model was placed in a parallel-plate flow chamber. A laminar shear stress of 0.3 Pa was applied to the surfaces of the cells for 48 hours. Promotion of micro-vessel network formation was detectable after approximately 10 hours in the flow chamber. After 48 hours, the length of networks exposed to shear stress was 6.17 ( $\pm$  0.59) times longer than at the initial state, whereas the length of networks not exposed to shear stress was only 3.30 ( $\pm$  0.41) times longer. The number of bifurcations and endpoints increased for networks exposed to shear stress, whereas the number of bifurcations alone increased for networks not exposed to shear stress. These results demonstrate that shear stress applied to the surfaces of endothelial cells on collagen gel promotes the growth of micro-vessel network formation in the gel and expands the network due to repeated bifurcation and elongation.

## 1 Introduction

Angiogenesis is the formation of new micro-vessels (capillaries) by endothelial cells (ECs) migrating and proliferating from the pre-existing vessel. This process is essential for numerous physiological events such as embryonic development, ovulation, and wound healing (1). Angiogenesis is also beneficial for tissue recovery by reperfusion of ischemic tissue, but is maladaptive for arteriosclerosis, diabetes, and tumor growth (2). With three-dimensional (3D) models, *in vitro* experiments have significantly advanced the understanding of angiogenesis. These models are based on the ability of stimulated ECs to invade substrates in a 3D manner. When confluent cells cultured on gels are activated by cytokines such as bFGF (3) and VEGF (4) or by phorbol esters (5), they invade the underlying gel and form capillary-like structures. Compared with 2D models (e.g., Matrigel model), 3D models more accurately represent an *in vivo* environment. In 3D models, depending on the culture media composition, ECs are induced to sprout, proliferate, migrate, or differentiate in a 3D manner (6). Shear stress also plays a role as a significant stimulus for angiogenesis. *In vivo* studies, Ichioka et al. (7) indicate that wound-healing angiogenesis is enhanced by the adaptive response of microvasculature to shear stress, and Nasu et al. (8) show that increased blood flow causes tumor

vascular enlargement. Recent *in vitro* experiments, Gloe et al. (9) identify that shear stress induces capillary-like structure formation, and Cullen et al. (10) find that shear stress is a physiologically relevant stimulus for EC migration and angiogenesis.

To clarify the details of the physiological and pathophysiological processes of angiogenesis under shear stress stimulus, 3D networks of capillary-like structure must be reconstructed. We successfully reconstructed the 3D network formation under shear stress stimulus (11). To assess the effect of shear stress on micro-vessel formation, we used an *in vitro* 3D model in which ECs were induced by a basic fibroblast growth factor (bFGF) to invade a collagen gel. Bovine pulmonary microvascular ECs (BPMECs) were seeded onto collagen gels with bFGF and then placed in a parallel-plate flow chamber. A laminar shear stress of 0.3 Pa was applied to the surfaces of the ECs for 48 hours. The total length of the networks was measured and used as an index of network formation. The density and the number of bifurcations and endpoints of the networks were measured to evaluate the morphology of the network. The migration velocity and direction of the ECs on the surface of collagen gel were measured to evaluate the influence of shear stress on the cells of the confluent monolayer of the 3D model. We considered the effect that shear stress applied to the ECs on the surface of collagen gel had on the network formation in the gel. Our results reveal that shear stress induces network formation, enhances EC migration velocity, and affects both the direction of EC migrate and the morphology of the network.

## **2 Methods**

### *2.1 Endothelial cell culture*

Cultured BPMECs were purchased from Cell Systems (lot. 32030, USA) and were used in all experiments. BPMECs had been used *in vitro* experiments (12, 13) as capillary ECs, the property and culture methods of these cells have been established. These cells were cultured in Dulbecco's modified Eagle's medium (DMEM; 31600-34, GIBCO, USA) supplemented with 10% fetal bovine serum (FBS; lot. 9K2087, JRH Biosciences, USA), 1% antibiotic-antimycotic (15240-062, GIBCO, USA), and 15 mM HEPES (346-D1373, DOJINDO, Japan). The BPMECs were seeded in 60-mm culture dishes (430166, Corning, USA.) and cultivated under standard conditions (37°C, 5% CO<sub>2</sub>). BPMECs were passaged using of trypsin-EDTA (25300-054, GIBCO, USA). In our experiments, we used BPMECs passaged between 5 and 9 times.

### *2.2 In vitro network formation assay*

Collagen gels were prepared as follows: 8 volumes of type I collagen solution (3.0 mg/ml; Cellmatrix Type I-A, Nitta Gelatin, Japan) were mixed with 1 volume of 5×



DMEM and 1 volume of 0.1 N NaOH (192-02175, Wako Pure Chemicals Industries, Japan) on ice. The mixture was then poured into a glass-base dish (3911-035, IWAKI, Japan) and allowed to gel at 37°C for 30 minutes. BPMECs were seeded onto 1.53-mm-thick collagen gels at  $4 \times 10^5$  cells per 35-mm culture dish. The cells reached confluence 72 hours after seeding, and 30 ng/ml bFGF (Recombinant Human Fibroblast Growth Factor-basic; 100-18B, Pepro Tech, UK) was added to the culture medium to promote network formation (3, 4). The ECs were then incubated at 37°C in 5% CO<sub>2</sub>. After the addition of bFGF, the ECs invaded the underlying gel and began forming the network. This 3D network model was used in the experiments.

### 2.3 Application of shear stress

Collagen gels with 3D networks were placed into a parallel-plate flow chamber made of polycarbonate (Fig. 1), and the ECs grown on these collagen gels were subjected to well-defined laminar fluid shear stress by the flow of culture medium (DMEM). Flow of DMEM was provided by a sterile continuous-flow loop. Shear stress on ECs ( $\tau$ , in Pa) was calculated by using the following formula:

$$\tau = 6Q\mu/bh^2$$

where  $\mu$  is fluid viscosity ( $8.5 \times 10^{-4}$  Pa·s at 37°C),  $Q$  is flow rate (cm<sup>3</sup>/s),  $h$  is the flow chamber height (0.2 mm), and  $b$  is the flow chamber width (20 mm). Because the main objective of this study was to show that the ability of microvasculature ECs to form new micro-vessel was modified under the conditions whether shear stress exists or not, the  $\tau$  in the chamber was  $0.30 \pm 0.06$  Pa to compare with previous in vivo study (7). The BPMECs were subjected to this  $\tau$  for 48 hours. The flowing culture medium was kept at 37°C in a water bath and was gassed with 5% CO<sub>2</sub>-95% air to maintain pH 7.5 throughout the experiment. Bubbles were removed by a bubble trap. The perfusate was circulated by a roller pump (MP-3N, EYELA, Japan) in the flow circuit. The total priming volume was 60 ml for the entire circuit. For control, the 3D models were left at rest (static conditions,  $\tau = 0$ ) under standard conditions (37°C, 5% CO<sub>2</sub>) throughout the experiments.

### 2.4 Images of the structure of 3D networks

The 3D network models under static conditions were dyed with CellTracker Green BODIPY (C-2102, Molecular Probes, USA) to observe the 3D structure of the network in detail. After 3D networks were formed, the collagen gel sample was washed in serum-free culture medium. CellTracker at 25 mM concentration was added, and the network was incubated for 45 minutes at 37°C. After the sample was washed in serum-free culture medium, the images were recorded by using a laser scanning confocal microscope (MRC-600; BIO-RAD Laboratories, CA, USA) with

a 20× objective lens. The emission of BODIPY excited at a wavelength of 488 nm with a 25-mW argon ion lasers was detected in the wavelength region longer than 515 nm. Images were recorded every 5 μm in depth, starting from the confluent layer.

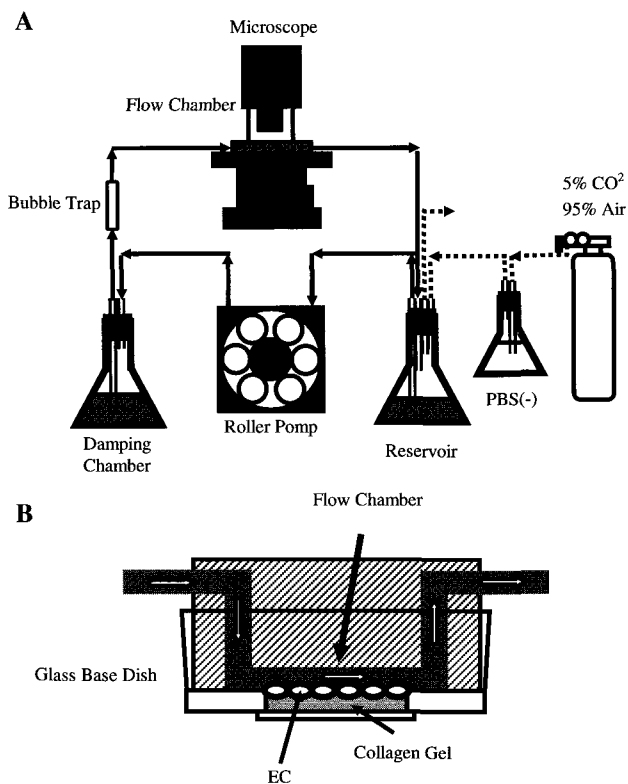


Figure 1. Apparatus to apply shear stress to endothelial cells. (A) A flow chamber (dark shading) placed on the stage of a phase contrast microscope was connected to a continuous flow circuit of culture medium (DMEM; arrows) and gas (5% CO<sub>2</sub>-95% air; broken line). (B) ECs (ovals) in collagen gel (light shading) were subjected to shear stress by flow of DMEM (white arrows) for 48 hours. The height and width of the flow chamber were 0.2 mm and 20 mm, respectively.

### 2.5 Measurement of network morphology and EC migration using 2D parameters

Although there were 3D networks in the gel, we used 2D parameters because the formation of networks in a horizontal direction to the collagen surface was much larger than that in a perpendicular direction. The acquired phase images were analyzed by using a scion image analyzer (Scion Corporation, USA). When we measured the following parameters, we focused only on one network per dish. As ECs began forming the network all over the dish 24 hours after the addition of bFGF, there were more than 500 early networks in the dish and one network, near the

center of the culture dish was randomly selected for analysis. The growth of the network was quantified by determining the total additive length of the network. The network density was calculated from the total additive length of the network divided by the area enclosing all the endpoints of the network (Fig. 2C). The network length and its density with time were respectively normalized by the initial length and density (i.e., at 0 hours of applied shear stress). Coordinates of the network centroid were calculated as follows:

$$x = \sum x_i / n$$

$$y = \sum y_i / n$$

where  $x_i$  and  $y_i$  are the x- and y-coordinates of the i-th point along the network. Migration velocity and direction of ECs on the surface of collagen gel were calculated by tracking a single cell in the phase contrast images. Because these images were recorded at 10-minute intervals for 48 hours, it was easy to detect the successive movements of individual cells. We randomly chose some cells in the region near the network centroid (distance in the direction parallel to collagen surface between the network centroid and the cell was within 100  $\mu\text{m}$ ) and some cells far from the centroid (over 100  $\mu\text{m}$ ) and tracked each cell. The downstream direction of the flow was defined as 0°.

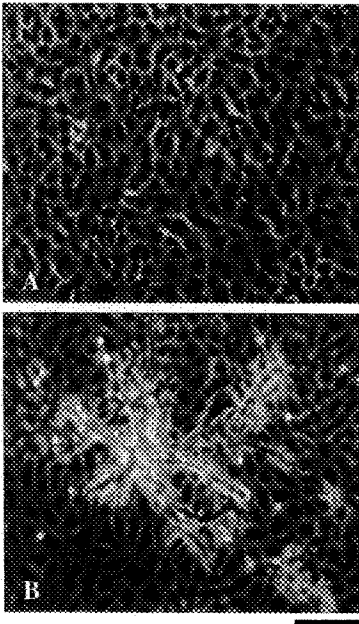


Figure 2. In vitro model of 3D network formation. ECs (A) grown to confluent on the surface of collagen gel and (B) incubated with bFGF (30 ng/ml) for 48 hours under static conditions. Bar scale: 100  $\mu\text{m}$ .

### 3 Results

Growth factor bFGF enhanced the network formation in vitro. To assess the effect of shear stress on micro-vessel formation, we used an in vitro 3D model in which ECs were induced to invade a collagen gel. BPMECs formed a confluent monolayer on the surface of the collagen gel 72 hours after seeding (Fig. 2A), which we added 30 ng/ml bFGF. 24 hours after the addition of bFGF, the cells had invaded the underlying gel to begin forming the networks, which was slightly beneath the original

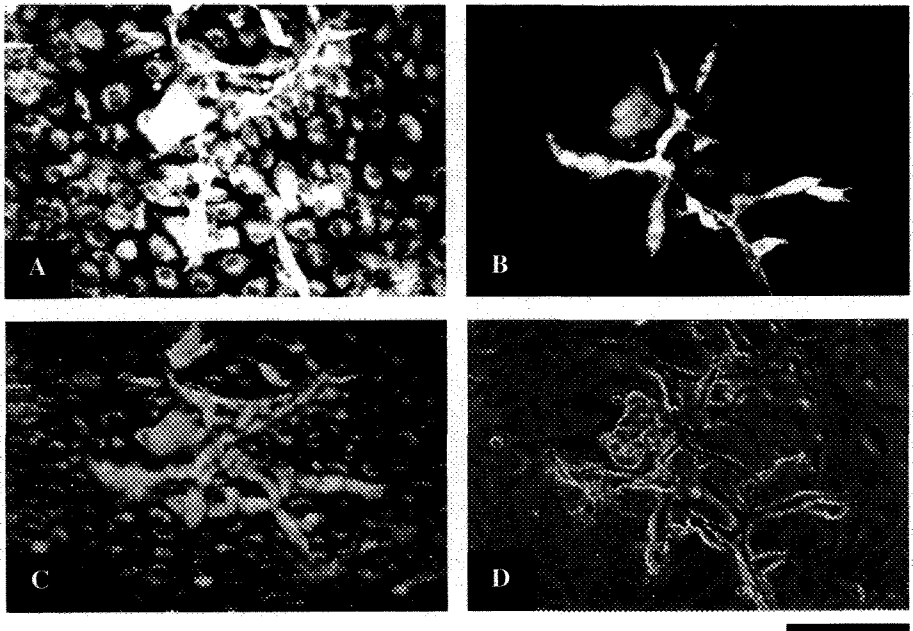


Figure 3. Fluorescent image of 3D network formation model under static conditions. Fluorescent image of (A) confluent monolayer and (B) structure 20  $\mu\text{m}$  below the confluent monolayer. (C) Fluorescent image and (D) phase contrast image of the 3D structure of the network. Bar scale: 100  $\mu\text{m}$ .

monolayer. After 48 hours of incubation with bFGF, these cells organized into branching capillaries and formed an extensive network under the surface monolayer (Fig. 2B), same as previous studies (3, 4).

To observe the 3D structure of the network in detail, the ECs were dyed with CellTracker after 72 hours of incubation with bFGF and images were recorded every 5  $\mu\text{m}$  in depth, starting from the confluent layer by using confocal laser scanning microscopy. These images were used to clarify the 3D structure of the network with the help of image analysis software. The results clearly show that cells invaded the collagen gel (Fig. 3), and reached a depth of up to 50  $\mu\text{m}$ . Images of thin sections perpendicular to the collagen surface obtained by using electron microscopy confirmed that the EC reconstructed the tubular structures, containing a clearly defined lumen consisting of multiple cells.

To investigate the effect of shear stress on network formation, cells were incubated with bFGF for 24 hours and then subjected to laminar shear stress or left at static condition for 48 hours. The total length of the network was measured as an index of network formation. Results show that after 9 hours (Fig. 4), applied shear stress did not significantly affect the network formation; the total length of the

network under applied shear stress increased by a factor of  $1.38 \pm 0.14$  compared with the initial length (i.e., at 0 hours of applied shear stress), similar to the increase under static conditions ( $1.42 \pm 0.13$ ). After approximately 10 hours, however, applied shear stress started to enhance the network formation (Fig. 4), compared with network formation under static conditions. After 24 hours, the enhancement was significant; the network length increased by a factor of  $3.13 \pm 0.46$  under applied shear stress, compared with  $2.17 \pm 0.29$  for static conditions ( $P < 0.01$ ). After 48 hours, the enhancement reached a maximum; a factor of  $6.17 \pm 0.59$  under applied shear stress, compared with  $3.30 \pm 0.41$  for static conditions ( $P < 0.01$ ), indicating that the total length under applied shear stress was 1.87 times longer than under static conditions. These results clearly show that the 3D network formation was significantly enhanced by shear stress loading.

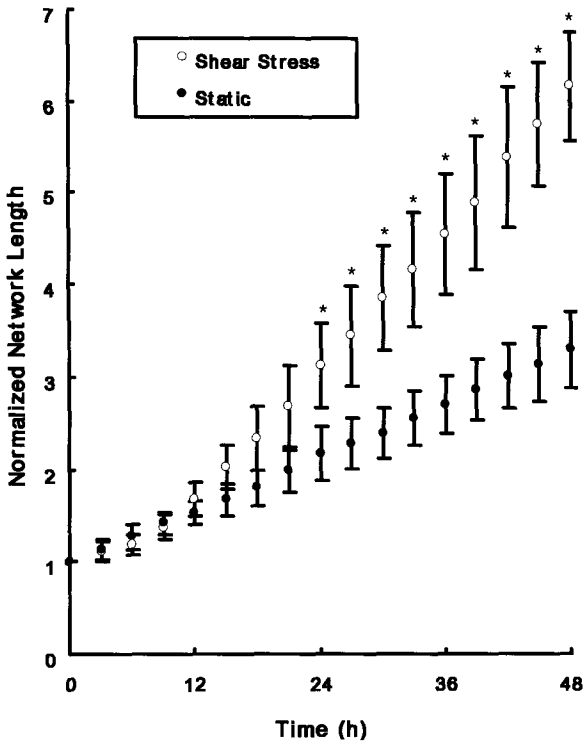


Figure 4. Effect of shear stress on network length. Total length of the network under shear stress and static conditions were calculated every 3 hours. Total length was normalized by the initial total length (i.e., at 0 hours). Data are mean  $\pm$  S.D.,  $n=6$ , \* $P < 0.01$  vs static cultures.

## 4 Discussion

Correlation between blood flow and angiogenesis in vivo has been reported (7, 8). For example, Ichioka et al. (7) showed that the blood flow in vessels influenced angiogenesis. They used vasodilator prazosin to modify the blood flow, and found that angiogenesis during wound healing in the rabbit ear chamber was positively influenced by elevated prazosin-induced shear stress. Nasu et al. (8) observed growing tumor vessels in vivo to elucidate the relationship between blood flow and vascular enlargement, and showed that tumor angiogenesis depended more on local hemodynamics than on vascular growth factors. In an in vitro study, Albuquerque et al. (14) demonstrated that physiological shear stress enhances wound closure in cultured human umbilical vein and coronary artery ECs through the action of EC spreading and migration. In another in vitro study, Urbich et al. (15) indicated that the shear stress-induced migration was independent of cell proliferation, but was dependent on the fibronectin receptor  $\alpha_5\beta_1$ . Only few studies, however, have quantified the relationship between network formation and shear stress. Recent in vitro studies showed that flow induced the growth of the network formation of ECs in 2D (10, 9). In our study, we successfully reconstructed a 3D network formation model that mimics the conditions of an in vivo environment (6). The application of shear stress on the ECs resulted in an increased length of the entire network after approximately 10 hours (Fig. 4), the same time that active migration of cells on the collagen gel began.

This refractory period, which required transmitting the effect of shear stress to EC features, was thought to be similar to previous studies. Franke et al. (10) showed that the endothelial stress fibers could be induced by a 3 hours exposure of shear stress of 0.2 Pa and Ookawa et al. (17) indicated that stress fiber-like structure was formed by a 3 hours exposure of shear stress of 2.0 Pa. Wechezak et al. (18) exposed shear stress of 0.93 Pa on ECs for 2 hours and observed that microfilament bundles and their associated focal contacts were concentrated in the proximal cell regions. As just described, these changes in cytoskeleton and adherence protein need several hours and probably cause the refractory period of EC migration and network formation. For EC migration, Tanishita et al. (19) also observed ECs under shear stress of 5 Pa in which migration velocity was 1-5  $\mu\text{m}/\text{h}$  initially, accelerated slightly after 12 to 16 hours, finally reaching approximately 16  $\mu\text{m}/\text{h}$  after 16 hours. In our study, we observed that ECs required approximately 10 hours to transmit the effect of shear stress to not only EC migration but also network formation. Our study also revealed that the migration velocity and direction of ECs on the confluent surface depended on the distance from the network centroid. Thus, the nature of cellular migration strongly affects the network formation in the gel.

Numerous previous studies focused on relationships between shear stress and growth factors such as bFGF and VEGF. For example, Gloe et al. (9) demonstrated that shear stress induced the release of bFGF from EC, and Malek et al. (20)

reported that laminar shear stress induced bFGF mRNA expression. Milkiewicz et al. (21) reported that higher capillary shear stress increases VEGF expression, whereas Conklin et al. (22) reported that low shear stress increases VEGF expression in ECs. Furthermore, NO is associated with angiogenesis. For example, Smith et al. (23) reported that eNOS enhances angiogenesis, and Lee et al. (24) showed that NO induces angiogenesis *in vivo* and *in vitro* by promoting EC migration and differentiation into capillaries. Lee et al. (24) also demonstrated that NO increased  $\alpha_v\beta_3$  integrin expression in ECs, a critical mediator of EC-matrix adhesion and migration. Although proteolysis is a key step in angiogenesis, matrix metalloproteinase does not increase after stimulation by shear stress (25). Our results show that in the presence of bFGF the migration velocity of ECs without applied shear stress (static conditions) only slightly increased, whereas that of ECs under shear stress conditions significantly increased.

In summary, shear stress promoted the growth of 3D network formation *in vitro*. The enhancement became detectable 10 hours after the initiation of shear stress. After 48 hours, the growth rate (i.e. increase in network length) of a network under shear stress conditions was approximately 2 times faster than that of a network under static conditions. Furthermore, shear stress applied to ECs on the surface of collagen gel influenced the process of network formation in the gel. The endpoints of the network branches were extended, and the networks were significantly expanded due to repeated bifurcation and elongation.

## Acknowledgments

This work was supported financially in part by Grants-in-Aids for Scientific Research 15086214 and 17650144 from the Ministry of Education, Culture, Sports, Science and Technology, Japan and the 21<sup>st</sup> Century COE program, System Design: Paradigm shift from intelligence to life.

## References

1. Gerwins, P., Skoldenberg, E., Claesson-Welsh, L., 2000. Function of fibroblast growth factors and vascular endothelial growth factors and their receptors in angiogenesis. *Crit. Rev. Oncol. Hematol.* 34, 185-194.
2. Carmeliet, P., Jain, R.K., 2000. Angiogenesis in cancer and other diseases. *Nature* 407, 249-257.
3. Montesano, R., Vassalli, J.D., Baird, A., Guillemin, R., Orci, L., 1986. Basic fibroblast growth factor induces angiogenesis *in vitro*. *Proc. Natl. Acad. Sci. USA* 83, 7297-7301.
4. Pepper, M.S., Ferrara, N., Orci, L., Montesano, R., 1995. Leukemia inhibitory factor (LIF) inhibits angiogenesis *in vitro*. *J. Cell. Sci.* 108, 73-83.

5. Montesano, R., Orci, L., 1985. Tumor-promoting phorbol esters induce angiogenesis in vitro. *Cell*. 42, 469-477.
6. Vailhé, B., Vittet, D., Feige, J.J., 2001. In vitro models of vasculogenesis and angiogenesis. *Lab. Invest.* 81, 439-452.
7. Ichioka, S., Shibata, M., Kosaki, K., Sato, Y., Harii, K., Kamiya, A., 1997. Effects of shear stress on wound-healing angiogenesis in the rabbit ear chamber. *J. Surg. Res.* 72, 29-35.
8. Nasu, R., Kimura, H., Akagi, K., Murata, T., Tanaka, Y., 1999. Blood flow influences vascular growth during tumour angiogenesis. *Br. J. Cancer* 79, 780-786.
9. Gloe, T., Sohn, H.Y., Meininger, G.A., Pohl, U., 2002. Shear stress-induced release of basic fibroblast growth factor from endothelial cells is mediated by matrix interaction via integrin  $\alpha\beta 3$ . *J. Biol. Chem.* 277, 23453-23458.
10. Cullen, J.P., Sayeed, S., Sawai, R.S., Theodorakis, N.G., Cahill, P.A., Sitzmann, J.V., Redmond, E.M., 2002. Pulsatile flow-induced angiogenesis: role of Gi subunits. *Arterioscler. Thromb. Vasc. Biol.* 22, 1610-1616.
11. Ueda, A., Koga, M., Ikeda, M., Kudo, S., Tanishita, K., 2004. Effect of shear stress on micro-vessels network formation of endothelial cells with in vitro three-dimensional model, *American J. Physiology Heart Circ. Physiol.* 287, H994-H1002.
12. Garcia, J.G., Liu, F., Verin, A.D., Birukova, A., Dechert, M.A., Gerthoffer, W.T., Bamberg, J.R., English, D., 2001. Sphingosine 1-phosphate promotes endothelial cell barrier integrity by Edg-dependent cytoskeletal rearrangement. *J. Clin. Invest.* 180, 689-701.
13. Tomii, Y., Kamochi, J., Yamazaki, H., Sawa, N., Tokunaga, T., Ohnishi, Y., Kijima, H., Ueyama, Y., Tamaoki, N., Nakamura, M., 2002. Human thrombospondin 2 inhibits proliferation of microvascular endothelial cells. *Int. J. Oncol.* 20, 339-342.
14. Albuquerque, M.L., Waters, C.M., Savla, U., Schnaper, H.W., Flozak, A.S., 2000. Shear stress enhances human endothelial cell wound closure in vitro. *Am. J. Physiol. Heart Circ. Physiol.* 279, H293-H302.
15. Urbich, C., Dernbach, E., Reissner, A., Vasa, M., Zeiher, A.M., Dimmeler, S., 2002. Shear stress-induced endothelial cell migration involves integrin signaling via the fibronectin receptor subunits  $\alpha 5$  and  $\beta 1$ . *Arterioscler. Thromb. Vasc. Biol.* 22, 69-75.
16. Franke, R.P., Grafe, M., Schnittler, H., Seiffge, D., Mittermayer, C., Drenckhahn D., 1984. Induction of human vascular endothelial stress fibres by fluid shear stress. *Nature* 307, 648-649.
17. Ookawa, K., Sato, M., Ohshima, N., 1992. Changes in the microstructure of cultured porcine aortic endothelial cells in the early stage after applying a fluid-imposed shear stress. *J. Biomech.* 25, 1321-1328.



18. Wechezak, A.R., Wight, T.N., Viggers, R.F., Sauvage, L.R., 1986. Endothelial adherence under shear stress is dependent upon microfilament reorganization. *J. Cell Physiol.* 139, 136-146.
19. Tanishita, K., Nagayama, K., Fujii, M., Kudou, S., 1999. Empirical study on grouping behavior of individual endothelial cells under shear stress. *JSME Int. J. C-Mech. Sy.* 42, 715-720.
20. Malek, A.M., Gibbons, G.H., Dzau, V.J., Izumo, S., 1993. Fluid shear stress differentially modulates expression of genes encoding basic fibroblast growth factor and platelet-derived growth factor B chain in vascular endothelium. *J. Clin. Invest.* 92, 2013-21.
21. Milkiewicz, M., Brown, M.D., Egginton, S., Hudlicka, O., 2001. Association between shear stress, angiogenesis, and VEGF in skeletal muscles in vivo. *Microcirculation* 8, 229-241.
22. Conklin, B.S., Zhong, D.S., Zhao, W., Lin, P.H., Chen, C., 2002. Shear stress regulates occludin and VEGF expression in porcine arterial endothelial cells. *J. Surg. Res.* 102, 13-21.
23. Smith, R.S. Jr., Lin, K.F., Agata, J., Chao, L., Chao, J., 2002. Human endothelial nitric oxide synthase gene delivery promotes angiogenesis in a rat model of hindlimb ischemia. *Arterioscler Thromb. Vasc. Biol.* 22,1279-1285.
24. Lee, P.C., Kibbe, M.R., Schuchert, M.J., Stolz, D.B., Watkins, S.C., Griffith, B.P., Billiar, T.R., Shears, L.L. II., 2000. Nitric oxide induces angiogenesis and upregulates avb3 integrin expression on endothelial cells. *Microvasc. Res.* 60, 269-280.
25. Rivilis, I., Milkiewicz, M., Boyd, P., Goldstein, J., Brown, M.D., Egginton, S., Hansen, F.M., Hudlicka, O., Haas, T.L., 2002. Differential involvement of MMP-2 and VEGF during muscle stretch- versus shear stress-induced angiogenesis. *Am. J. Physiol. Heart Circ. Physiol.* 283, H1430-H1438.

# TIME-DEPENDENT MECHANICAL BEHAVIORS OF ARTICULAR CARTILAGE AND CHONDROCYTES UNDER CONSTANT TOTAL COMPRESSIVE DEFORMATION

T. MURAKAMI, N. SAKAI, Y. SAWAE, Y. KUROHARA,  
I. ISHIKAWA AND M. OKAMOTO

*Department of Intelligent Machinery and Systems, Kyushu University,  
744 Motoooka, Nishi-ku, Fukuoka 819-0395, Japan  
E-mail: tmura@mech.kyushu-u.ac.jp*

The excellent performance of very low friction and long durability of natural synovial joints is maintained with synergistic metabolism of articular cartilage and synovial fluid. To study metabolic mechanism including repair process, it is important to know the stress-strain state of the cartilage and extracellular matrix around chondrocytes during cartilage deformation, where chondrocytes seem to experience similar deformation to extracellular matrix. The articular cartilage of high water content has a biphasic viscoelastic property and shows the time-dependent deformation behavior. In this study, the compressive behaviors in articular cartilage containing chondrocytes were observed in the compressive apparatus located in the stage of confocal laser scanning microscope. The time-dependent behavior of articular cartilage was evaluated by the finite element method for biphasic model.

## 1 Introduction

The natural synovial joints have excellent tribological performance known as very low friction and very low wear for various daily activities in human life. To maintain the excellent performance, the adaptive multimode lubrication mechanism is likely to operate under various activities in which the elasto-hydrodynamic lubrication, weeping, adsorbed film and/or gel film lubrication can become effective depending on the severity of operating conditions [1-3]. In natural synovial joints subjected to severe loading and rubbing, various protective roles of synovial fluid, cartilage surface layer, extracellular matrix and chondrocyte are required. It is important to repair the damaged surface layer by not only synovial fluid containing phospholipids, proteins, hyaluronic acid etc. but also supply of proteoglycan from extracellular matrix produced by chondrocytes as shown in Fig. 1 [4-6]. For supply of proteoglycan to surface gel film, the chondrocytes in surface zone appear to play an important role. The articular cartilage adapts to changing mechanical environments, but the detailed adaptive and/or restorative process has not yet been clarified. To study such mechanism involved, it is important to know the stress-strain state of the cartilage and extracellular matrix around chondrocytes during cartilage deformation, where chondrocytes seem to experience similar deformation to extracellular matrix. The articular cartilage has a biphasic viscoelastic property based on a high water content up to 80%. In this study, therefore, the time-dependent deformation of compressed articular cartilage was observed in the

compressive apparatus located in the stage of confocal laser scanning microscope (CLSM). The stained chondrocytes were used as markers to evaluate the local strain of articular cartilage. The enlarged images of chondrocytes at higher magnification exhibited the deformed state of chondrocyte. In this study, the excessive deformation of chondrocyte in the surface zone is focused.

The finite element method (FEM) for biphasic model was applied to evaluate the time-dependent mechanical behavior of articular cartilage. The influence of surface boundary conditions on deformation was examined.

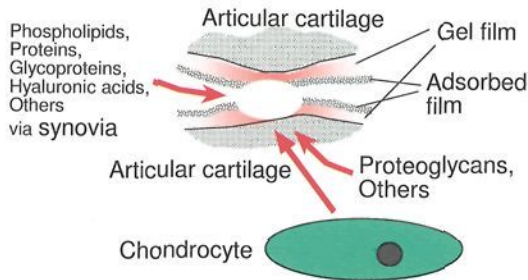


Figure 1. Restoration of locally damaged articular cartilage surfaces via synovial fluid and extracellular matrix.

## 2 Materials and Methods

### 2.1 Experimental compression test in confocal laser scanning microscope

The cartilage specimens are prepared from the intact femoral condyle of porcine knee joints. The cylindrical specimen of 3 mm diameter was prepared by the punch. Then, the cylinder was sectioned as half size with a scalpel. The semi-cylindrical specimen includes the subchondral bone of about 0.5 mm thickness. Next, we observed the changes in local strain in articular cartilage specimens by monitoring the position of stained chondrocyte in the CLSM. The staining of chondrocyte is treated with calcein-AM, at 1  $\mu\text{l/ml}$  and 37°C for 30 min. The compression apparatus (Fig. 2) with high precision within 0.2  $\mu\text{m}$  for position control was newly developed [5, 6]. This apparatus was allocated on the stage of CLSM and the compression speed can be adjusted from 1  $\mu\text{m/s}$  to 4 mm/s by feed-back control of DC servo-motor. In this study, 13% or 15% total compressive strain was applied by moving impermeable alumina ceramic plate at constant speed. The local strain was estimated as the approaching distance divided by the initial distance in perpendicular direction to the surface between corresponding chondrocytes in each layer in cartilage. On the basis of these visualized images, the time-dependent and depth-dependent changes in local strain of articular cartilage were evaluated.

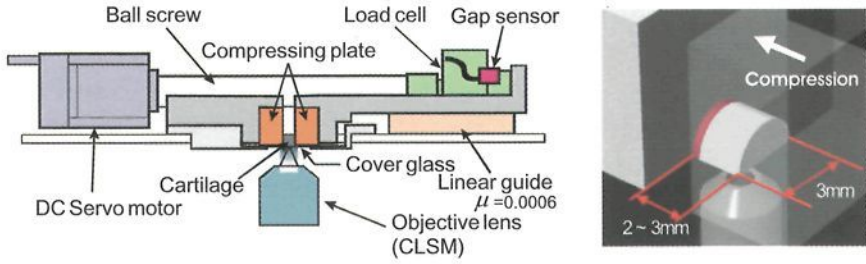


Figure 2. Test apparatus and specimen.

## 2.2 Finite element method for biphasic articular cartilage

The articular cartilage with high water content is treated as the biphasic model proposed by Mow et al. [7]. To evaluate time-dependent and depth-dependent compression behavior in articular cartilage, the biphasic FEM analysis [8] was applied for an axisymmetric cylindrical model. The governing equations for linear biphasic model are given as follows;

$$\nabla \cdot (\phi^s \mathbf{v}^s + \phi^f \mathbf{v}^f) = 0 \quad (1)$$

$$\boldsymbol{\sigma}^s = -\phi^s p \mathbf{I} + \lambda \text{tr}(\boldsymbol{\varepsilon}^s) \mathbf{I} + 2\mu \boldsymbol{\varepsilon}^s \quad (2)$$

$$\boldsymbol{\sigma}^f = -\phi^f p \mathbf{I} \quad (3)$$

$$\nabla \cdot \boldsymbol{\sigma}^s + \frac{(\phi^f)^2}{\kappa} (\mathbf{v}^f - \mathbf{v}^s) - p \nabla \phi^f = 0 \quad (4)$$

$$\nabla \cdot \boldsymbol{\sigma}^f - \frac{(\phi^f)^2}{\kappa} (\mathbf{v}^f - \mathbf{v}^s) + p \nabla \phi^f = 0 \quad (5)$$

Here,  $\mathbf{v}$  : velocity,  $\phi$  : constituent volume fraction,  $\boldsymbol{\sigma}$  : stress,  $\lambda, \mu$  : Lamé constants,  $\boldsymbol{\varepsilon}$  : strain,  $p$  : pore pressure,  $\mathbf{I}$  : identity tensor,  $\kappa$  : permeability, superscripts “s” and “f” correspond to solid phase and fluid phase, respectively.

The dependence of permeability on strain ( $\varepsilon < 0$  for compression) expressed as the following formula proposed by Jurvelin et al. [9].

$$\kappa_z = \kappa_0 + A \cdot \exp(\varepsilon/t) \quad (6)$$

The cylindrical model of 1.5 mm radius and 2.0 mm height is composed of tetrahedron elements with 10 nodes (including midpoints) as shown in Fig. 2, where the bottom plane of  $z = 0$  mm is fully fixed as the tidemark connected to subchondral bone without fluid flow. The upper surface ( $z = 2.0$  mm) was uniformly compressed to attain 15% total compression at the constant rate in 10 s and then kept as constant total compressive deflection under unconfined condition for outer cylindrical surface. In this study, the typical values for  $\phi^s=0.17$ ,  $\phi^f=0.83$ ,  $\lambda=0.1\text{MPa}$ ,  $\mu=0.3\text{MPa}$  were used. For the permeability, constant values in horizontal direction of  $\kappa_x = \kappa_y = 9.14 \times 10^{-15} \text{ m}^4/\text{N}\cdot\text{s}$  were used and the equation (6) was applied in the compressed direction with  $\kappa_0 = 1.75 \times 10^{-15} \text{ m}^4/\text{N}\cdot\text{s}$ ,  $A = 23.7 \times 10^{-15} \text{ m}^4/\text{N}\cdot\text{s}$ ,  $t = 0.025$ .

The influence of surface conditions on the compressive behavior was evaluated by changing the friction level and permeability as shown in Table 1. The healthy articular cartilage keeps low friction level of 0.01 as friction coefficient and lower permeability. The progress of osteoarthritis induces the increasing of friction and permeability, while the normal cartilage surface is covered with proteoglycan gel layer and adsorbed films, and keeps the lower permeability. Therefore, the condition 2 corresponds to normal cartilage, and condition 3 corresponds to degenerated cartilage in osteoarthritis. The intact cartilage is considered to be simulated with condition 2 but may be influenced by friction increase in local direct contact with indenter and the existence of some permeable region.

Table 1. Surface conditions for FEM analysis.

	Friction	Permeability
Condition1	Fixed	Impermeable
Condition2	Frictionless	Impermeable
Condition3	Fixed	Permeable
Condition4	Frictionless	Permeable

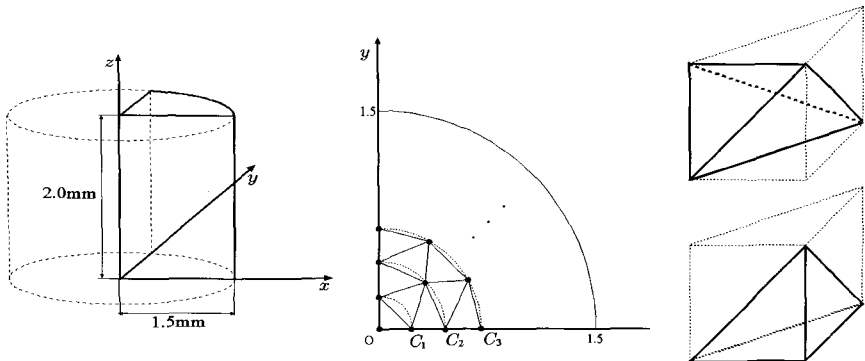


Figure 3. FEM model for articular cartilage.

### 3 Results

#### 3.1 Experimental compression test in confocal laser scanning microscope

In Fig. 4, the estimated values of local strain in cartilage specimens immediately after the total compressive deflection of 15% (0.15) was attained are plotted against the relative location in the depth direction, where 0 % means surface and 100% means the tidemark as the boundary of subchondral bone. We estimated the local strain by calculating the changes of the distance before and after compression in perpendicular direction to the cartilage surface between the definite stained chondrocytes as reported in the previous paper [5-6]. The local strain behaviors exhibited some depth-dependence, although the observation in top surface zone was difficult in many cases immediately after compression. It is noticed that the middle zone shows larger compression than deep zone particularly at lower strain rate.

Next, the changes in local strain at equilibrium during stress relaxation process under constant total compression of 15% (0.15) are shown in Fig. 5. The deformation of deeper zone was clearly recovered probably accompanied with flowing of fluid into the middle and deep zone. On the contrary, the surface zone was largely compressed than average strain during stress relaxation in unconfined compression. The corresponding movement of stained chondrocytes in the surface zone is visualized in Fig. 6, where three chondrocytes are indicated by circles. The chondrocytes located near surface before compression (Fig. 6(a)) were moved to the surface (Fig. 6(b)) and then significantly moved towards the surface resulting in remarkable flattening of chondrocytes (Fig. 6(c)).

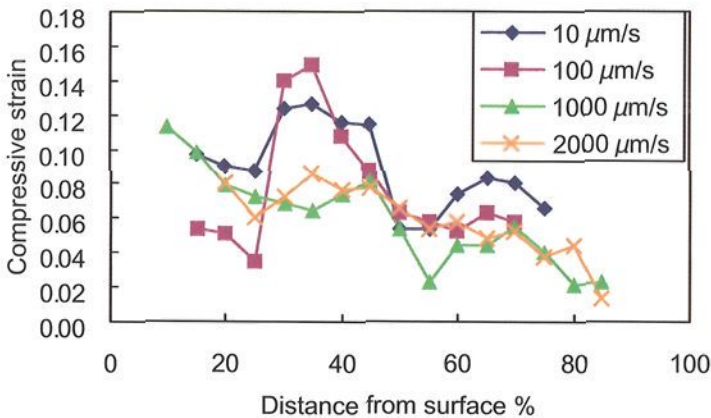


Figure 4. Local strain in articular cartilage immediately after compression.



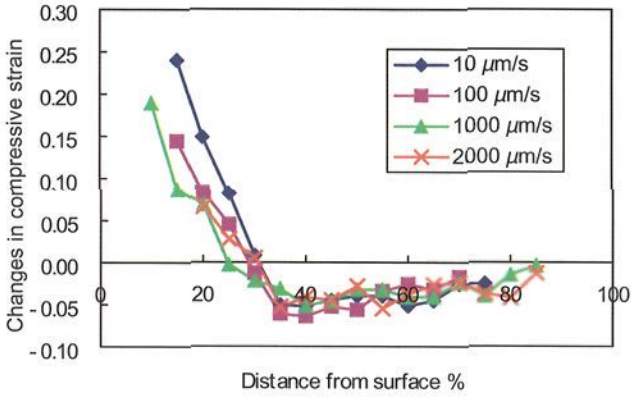


Figure 5. Changes in local strain in articular cartilage at equilibrium during stress relaxation process after compression.

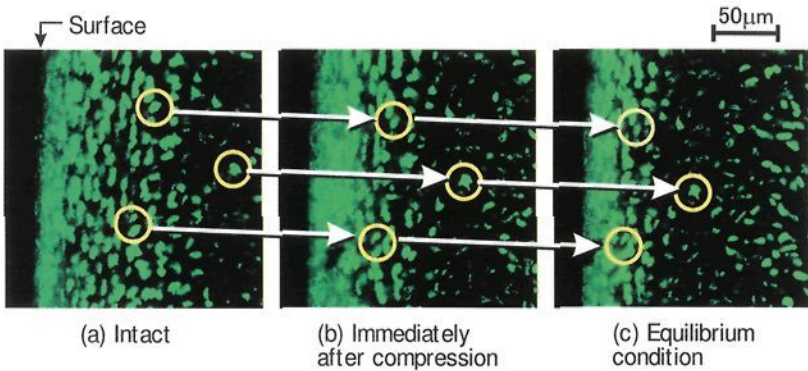


Figure 6. Changes in location of chondrocyte near surface in unconfined compression test.

To observe precisely the changes in deformation of chondrocytes, the morphology of chondrocyte was examined with large magnification. The three-dimensional images for chondrocyte morphology were reconstructed by stacks of images sliced by CLSM with about  $1.5 \mu\text{m}$  thickness. The three-dimensional images for the surface region of  $154 \mu\text{m} \times 154 \mu\text{m} \times 50 \mu\text{m}$  are shown in Fig. 7. In the intact condition the chondrocyte located near surface has a flattened geometry compared with one in deeper zone. Under compressive condition, chondrocytes are deformed with similar strain to cartilage. It was confirmed that the chondrocytes in the surface zone change their location immediately after compression, and then

approached significantly to the surface during stress relaxation process. At equilibrium condition, the chondrocytes are largely strained as shown in Fig. 7.

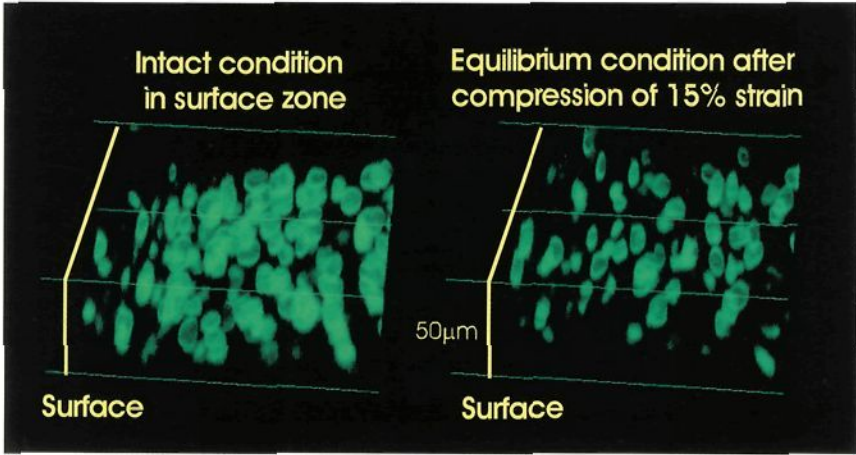


Figure 7. Three-dimensional visualization of chondrocytes in surface zone before and after compression.

### 3.2 Finite element analysis for biphasic articular cartilage

The time-dependent and depth-dependent compression behaviors of articular cartilage were evaluated by changing the surface boundary conditions. In this analysis, the strain in  $z$ -direction was calculated at the slow speed of  $30 \mu\text{m/s}$  for 10s to attain 15% (0.15) total strain. Figure 8 shows the distribution in compressive strain at  $z$  axis at 10 s, when 15% total strain has been attained. Under simplified condition 1 where both upper surface and lower planes are fixed, the middle zone is intensely compressed as larger strain than average level of 0.15, as suggested from the bulging behavior of cylindrical specimen. Under condition 2 which corresponds to healthy cartilage, the constant strain higher than the average is observed at the zone from middle layer to surface. At this low friction surface, the movement or extension of surface region to outer direction is not constrained, and thus the uniform compressive strain appears to be formed at higher level than the average but at lower level than the middle zone under condition 1, as indicated for soft tissues [10]. In contrast, under the condition 3 corresponding to degenerated cartilage, the larger compressive strain in the middle zone at similar level to condition 1 and higher strain near surface were observed. Under condition 4, the strain distribution combined of the condition 2 with condition 3 was produced. At the deep zone, there are not large differences among these four kinds of conditions. The strains from middle to surface zones are affected with differences in surface conditions.



Next, time-dependent strain behaviors near surface at  $z = 1.9$  mm (at 5% location from the surface) under these surface conditions are shown in Fig. 9. In this analysis for biphasic material of uniform and isotropic properties except permeability, all of the equilibrium strain values under four surface conditions approach to the average strain of 0.15, although the time-dependent paths are different. Under condition 1, the strain gradually increases. Under condition 2 for normal intact cartilage, at 10 s the strain attain a little higher value than the average but changes to decrease during stress relaxation process. Conditions 3 and 4 show some progress in deformation.

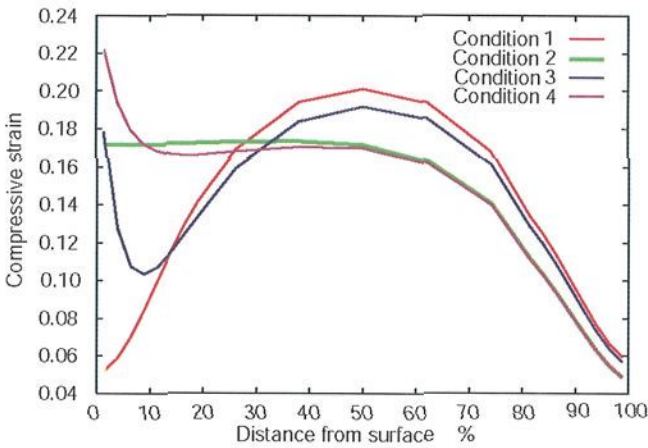


Figure 8. Strain distribution of cartilage at 10 s under four kinds of surface conditions.

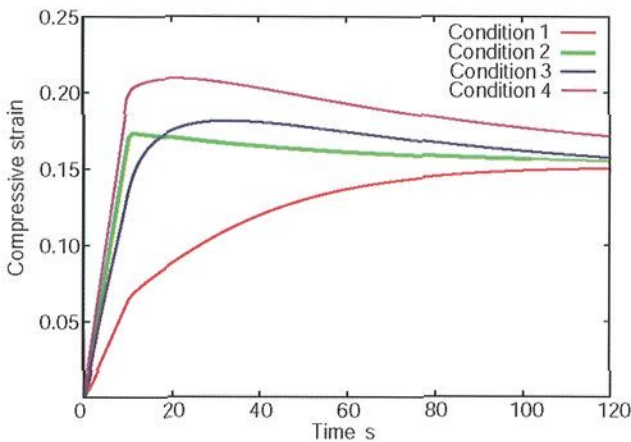


Figure 9. Changes in strain near surface under four kinds of surface conditions.

Figure 10 shows the distribution of pore pressure along thickness direction at 10 s, when total compressive strain of 0.15 has been just attained. Under conditions 1 and 3, high friction at upper surface and fixation at subchondral bone form higher pressure gradient from both bottom and surface-side to middle zone, which produces fluid flow towards the middle zone. For normal cartilage under condition 2, pore pressure gradually decreases from bottom, and thus one-way flow alone is expected. The larger pressure gradient near surface under conditions 3 and 4 suggests that the local strain can increase even after compressive process ended at 10 s as shown in Fig. 9.

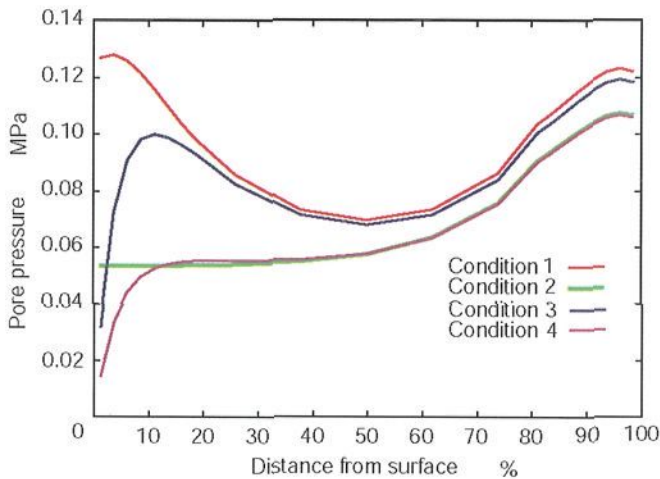


Figure 10. Distribution of pore pressure at 10 s.

#### 4 Discussion

In compression tests of articular cartilage in the apparatus on the stage of CLSM, the time-dependent and depth-dependent behaviors in the local strain of cartilage could be evaluated by observing the stained chondrocytes as markers. The fluorescent images indicated that the surface zone responded at more or less than the average at the initial stage of compression and then was largely compressed during stress relaxation. Although excessive strain of cartilage and chondrocyte in surface zone at equilibrium is mainly caused by unconstrained compression, similar situation might occur during deteriorating process with wear in osteoarthritis.

The time-dependent and depth-dependent compressive behaviors were evaluated by FEM analysis of corresponding biphasic cylindrical model with homogeneous and isotropic properties with an exception of strain-dependent permeability under four kinds of surface conditions for friction and permeability. The higher local strain in the middle zone immediately after compression at lower compression speed

(Fig. 4) might be related to some increase in friction during lower speed compression, where the experimental condition might approach to condition 1 or 3, as suggested by calculated results in Figs. 8 and 10. The restoration in the middle zone and the strain increasing in surface zone during relaxation process from slow to high compression speed ranges (Fig. 5) in experiment seem to correspond to not only the calculated pressure gradient in Fig. 10 but also the inhomogeneity particularly in surface zone. Although there are still problems to observe precisely the location of definite chondrocyte near surface in many cases immediately after compression, high or similar local strains compared with middle zone are observed near surface. As indicated in Figs. 5, 6 and 7, the cartilage and chondrocytes in the surface zone is excessively compressed at equilibrium after stress relaxation. In contrast, FEM analysis for homogeneous and isotropic material shows the asymptotic behavior to average strain for all conditions in Fig. 9. In our FEM analysis, the strain-dependent permeability did not induce large change in local strain at equilibrium compared with constant permeability. The phenomena of excessive strain appear to be influenced by heterogeneous and anisotropic properties of cartilage. Wang et al. [11] indicated that large strain of 50 % occurs near surface during the ramp loading phase in confined stress-relaxation compression with porous plate at average strain of 10%, although deep zone experiences only low strains less than average strain in the finite deformation biphasic analysis for articular cartilage with depth-dependent aggregate modulus ranging 20-fold difference between the surface and the deep zones. They confirmed that at equilibrium after stress relaxation, the inhomogeneous tissue can no longer achieve a uniform equilibrium strain state through the depth although uniform strain state is attained in a homogeneous tissue model. At our next stage of FEM analysis, inhomogeneous properties should be considered.

In summary, the fact that both cartilage and chondrocytes show the time-dependent and depth-dependent deformation was demonstrated in unconfined compression test of articular cartilage in this study. It was shown that the chondrocytes near surface particularly at equilibrium experiences larger strain than average state. FEM analysis indicated the importance of surface conditions for friction and permeability in time-dependent and depth-dependent deformation behaviors. To evaluate the actual function and durability of natural synovial joints with good metabolism, further researches by experimental visualization and numerical simulation [12-13] at both macroscopic tissue level and microscopic cellular level are required. Furthermore, we are exploring the biomechanical behaviors of chondrocytes and surrounding matrix at nanoscopic cytoskeleton and/or molecular level with consideration of mechano-transduction.

## Acknowledgments

Financial supports were given by the Grant-in-Aid of Japan Society for the Promotion of Science (A) 15200037 and the Grant-in-Aid for Scientific Research on Priority Areas 15086212 from the Ministry of Education, Culture, Sports, Science and Technology.

**References**

1. Dowson, D., 1966-67. Modes of Lubrication in Human Joints. Proc. Instn. Mech. Engrs. 181, Pt3J, 45-54.
2. Murakami, T., 1990. The Lubrication in Natural Synovial Joints and Joint Prostheses. JSME Int. J. Series III 33, No.4, 465-474.
3. Murakami, T., Higaki, H., Sawae, Y., Ohtsuki, N., Moriyama, S., Nakanishi, Y., 1998. Adaptive multimode lubrication in natural synovial joints and artificial joints. Proc. Instn. Mech. Engrs. 212, Part H, 23-35.
4. Murakami, T., Sawae, T. and Ihara, M., 2003. The Protective Mechanism of Articular Cartilage to Severe Loading: Roles of Lubricants, Cartilage Surface Layer, Extracellular Matrix and Chondrocyte. JSME Int. J. Ser.C 46, No.2, 594-603.
5. Murakami, T., Sawae, Y., Sakai, N., Ishikawa, I., 2005. Biomechanical and Biotribological Importance of Surface and Surface Zone in Articular Cartilage, Biomechanics at Micro- and Nanoscale Levels Vol. I, Ed. By Wada, H. World Scientific, 42-52.
6. Murakami, T., Sakai, N., Sawae, Y., Tanaka, K., Ihara, M., 2004. Influence of Proteoglycan on Time-dependent Mechanical Behaviors of Articular Cartilage under Constant Total Compressive Deformation. JSME Int. J., Ser. C 47, 1049-1055.
7. Mow, V.C., Kuei, S.C., Lai, W.M., Armstrong, C.G., 1980. Biphasic creep and stress relaxation of articular cartilage in compression theory and experiment. J. Bio. Eng. 102, 73-84.
8. Vermilyea, M.E., Spilker, R.L., 1992. A hybrid finite element formulation of the linear biphasic equations for hydrated soft tissue. Int. J. Num. Met. Eng. 33, 567-593.
9. Jurvelin, J.S., Buschmann, M.D. and Hunziker, E.B., 2003. Mechanical anisotropy of the human knee articular cartilage in compression. Proc. Instn. Mech. Engrs. 217, Part H, 215-219.
10. Wu, J.Z., Dong, R.G. and Schopper, A.W., 2004. Analysis of effects of friction on the deformation behavior of soft tissues in unconfined compression tests. J. Biomech. 37, 147-155.
11. Wang, C.C-B., Hung, C.T. and Mow V.C., 2001. An analysis of the effects of depth-dependent aggregate modulus on articular cartilage stress-relaxation behavior in compression. J. Biomech. 34, 75-84.
12. Guilak, F. and Mow V.C., 2000. The mechanical environment of chondrocyte: a biphasic finite element model of cell-matrix interactions in articular cartilage. J. Biomech. 33, 1663-1673.
13. Ihara, M., Murakami T. and Sawae, Y., 2003. Modelling of Articular Cartilage Containing Chondrocytes and Finite Element Analysis for Articular Cartilage and Chondrocytes Under Compression. Trans. JSME (in Japanese) Ser. C 678, 487-493.

This page is intentionally left blank

## **II. CELL RESPONSE TO MECHANICAL STIMULATION**

This page is intentionally left blank

# THRESHOLD FIBER STRAIN THAT INDUCES REORGANIZATION OF CYTOSKELETAL ACTIN STRUCTURE IN OSTEOBLASTIC CELLS

T. ADACHI

*Department of Mechanical Engineering and Science, Kyoto University,  
Yoshida-Honmachi, Sakyo-ku, Kyoto 606-8501, Japan  
E-mail: adachi@me.kyoto-u.ac.jp*

K. SATO

*Department of Mechanical Engineering, Yamaguchi University,  
2-16-1 Tokiwa-dai, Ube 755-8611, Japan  
E-mail: katsuyas@yamaguchi-u.ac.jp*

In reorganization process of the actin stress fibers, a change in its mechanical condition has been suggested as one of the key mediators. Some experimental studies have clarified that tension release in the stress fibers induces the fiber depolymerization that is considered as the initial phase of its reorganization. However, quantitative mechanical values such as strain or stress that induce the depolymerization still have not been evaluated. This study tried to quantify the fiber strain that induces the depolymerization of the actin stress fibers to gain a basic understanding of the reorganization phenomenon from a mechanical viewpoint. Osteoblastic cells were cultured on prestretched silicone rubber substrate. Compressive deformation was applied to the cells by uniaxially releasing the prestretched substrate strain and the change of the stress fiber structure was observed. The results indicated that the compressive strain, not in the whole cell body but in the stress fiber itself, is important to induce the disassembly of the fiber structure. In addition, the existence of a threshold strain for initiating fiber disassembly was suggested.

## 1 Introduction

The cytoskeletal actin stress fibers is known to act as one of the important components in the mechanosensory mechanism by which cells can sense mechanical stimuli such as force and deformation [1-4]. In osteoblasts, actin stress fibers particularly have a dense network-like structure aligned along the major axis of the spindle-like cell as shown in Fig. 1. This distinctive aligned structure may affect the characteristics of the intracellular calcium signaling response to the mechanical stimulus [4]. In addition, the structure of the stress fibers itself is dynamically reorganized under the change of the surrounding mechanical environment [5-8]. Although the details of the reorganization mechanism activated by a mechanical stimulus still are not clearly understood, the intracellular tension existing in the cytoskeletal structure is proposed as one of the mediators of the reorganization mechanism [9].



The intracellular tension is believed to play essential roles in various cellular dynamic functions such as cytokinesis [10], cell movements [11], signal transduction [12], remodeling of the extracellular matrix [13, 14], and the apoptosis [15]. The source of the intracellular tension is believed to relate with the stress fibers that contain actin polymer filaments and type-2 myosin [16-19]. Therefore, it is considered that the stress fiber itself can generate internal tensile force, and that tension normally exists in the stress fiber structure.

Regarding the role of intracellular tension in the reorganization mechanism, interesting phenomena have been reported: the compressive deformation, applied to the cell body, that partially releases the intracellular tension induces the disassembly of the stress fibers as an initial phase of the fiber structure reorganization [9, 20]. On the basis of this observation, intracellular tension can be considered as one of the mediators in reorganization mechanism. However, the quantitative evaluation of the mechanical value at which the reorganization of the stress fiber structure is induced has not yet been conducted.

The aim of this study was to evaluate the mechanical values, such as stress/strain, at which the stress fiber reorganization is induced. Because it is difficult to directly measure the intracellular tension in a living cell, except for the indirect measurement of the traction force in moving cells on a soft elastic substrate [21, 22], the fiber strain magnitude is evaluated as a mechanical measure related to the intracellular tension.

A new experimental apparatus for applying uniaxial compressive deformation to a cell body was designed. The apparatus holds a silicone rubber chamber in which *osteoblast-like cells (MC3T3-E1)* were plated and incubated on its prestretched bottom substrate. Controlled compressive uniaxial strain is applied to the chamber, by which the cells are deformed via elastic substrate deformation and the intracellular pretension in the cytoskeletal stress fibers is released. Then, the change of the stress fiber structure following the strain application is observed to quantitatively evaluate the strain magnitude at which stress fiber reorganization is induced.

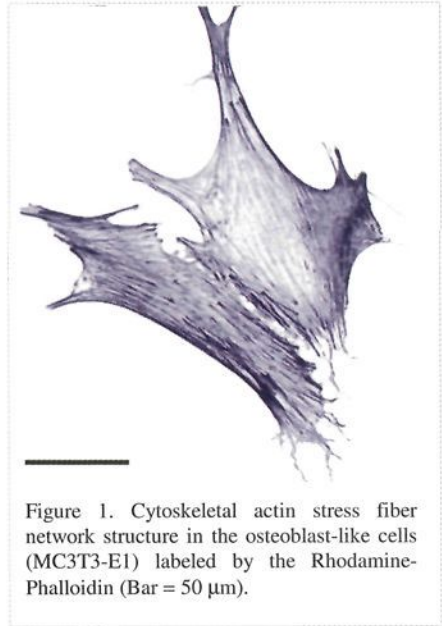


Figure 1. Cytoskeletal actin stress fiber network structure in the osteoblast-like cells (MC3T3-E1) labeled by the Rhodamine-Phalloidin (Bar = 50  $\mu\text{m}$ ).

## 2 Materials and Methods

### 2.1 Cell culture

Osteoblast-like MC3T3-E1 cells obtained from the RIKEN BioResource Center were plated sparsely at a density of  $3.0 \times 10^4$  cells / chamber ( $75.0$  cells /  $\text{mm}^2$ ). The cells were cultured in  $\alpha$ -minimum essential medium ( $\alpha$ -MEM: ICN Biomedicals) containing 10% fetal bovine serum (FBS: ICN Biomedicals) and were maintained in a 95% air – 5%  $\text{CO}_2$  humidified environment at 37 degree C. At 24 hours of incubation after plating, cells were used in the experiment.

### 2.2 Fluorescent labeling and observation of actin stress fibers

Actin stress fiber structures in the cells were observed using fluorescent labeling techniques. At  $t = 15$  min after the release of tension of the actin stress fibers, cells were fixed with 5% paraformaldehyde for 30 min at 4 degree C., rinsed with PBS, permeabilized by 0.1% Triton X-100, and labeled with Rhodamine-Phalloidin in PBS for 2.5 hours at 37 degree C., Phalloidin associates specifically with actin polymer filaments (F-Actin). Therefore, the stress fiber structure, which contains mainly actin polymer filaments, is specifically labeled. In contrast, unpolymerized monomeric actin (G-Actin) in cytosol is not labeled. Fluorescent images were obtained using a confocal laser-scanning microscope (Digital Eclipse C1: Nikon). Obtained images were recorded as 12-bit digitized image data using a PC. The focal plane was set at the bottom level of the cell where cells adhere to the substrate and the actin stress fibers are highly organized.

### 2.3 Experimental apparatus

A new apparatus for applying uniaxial compressive strain to the cells was designed for this study [23], as shown in Fig. 2. The apparatus can be mounted on the stage of an inverted microscope and operated at the installed position. The apparatus consists of two parallel linear guides, a shaft with right- and left-handed screws, and two sliders on which the silicone rubber chamber is mounted. The screw shaft drives these two sliders in opposite directions, and a stepping motor controls their displacements. Thus, controlled uniaxial strain can be applied to the silicone rubber substrate on which osteoblastic cells are plated.

Cells were plated in a 4 cc (inner dimensions: 20 x 20 x 10 mm) silicone rubber chamber (Scholertec, Japan). The bottom of the chamber is made of a thin transparent silicone rubber sheet with a thickness of 100  $\mu\text{m}$ , through which cells can be observed using an inverted microscope system. The inner surface of the chamber was treated with 5 M sulfuric acid for 30 min to promote cell adhesion to the substrate. Prior to the experiment, the chamber was washed with distilled water and sterilized in an autoclave.

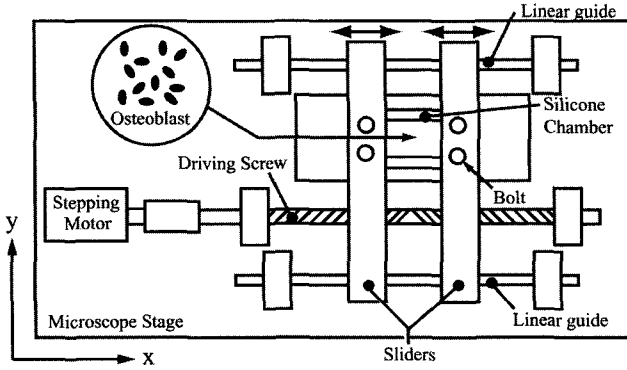


Figure 2. A schematic of experimental apparatus. The apparatus was mounted on an inverted microscope. The silicone rubber chamber in which cells were seeded was mounted on the two parallel sliders. Sliders were driven by a right- and left-handed screw shaft connected to the stepping motor, and controlled uniaxial strain was applied to the chamber [23].

#### 2.4 Evaluation of axial strain of stress fiber

In this study, we evaluated axial strain of the stress fibers as well as the magnitude of the strain applied to a whole cell body. Cytoskeletal actin stress fibers in osteoblastic cells mainly align along the long axis of the cell [4]. Therefore, the axial fiber strain depends on its relative angle to the direction of strain release of the silicone rubber substrate. The cellular axis was determined as the major axis of an ellipse fitted to the cell shape determined using image-processing software (Image Pro Plus; Media Cybernetics), as shown in Fig. 3, the following procedure. First, the obtained fluorescent image (Fig. 3(a)) was binarized to clarify the cell outline (Fig. 3(b)). Secondly, the ellipse fitted to the outline was calculated, and the angle between the major axis of the ellipse and the direction of strain release was defined as  $\theta$  ( $0 < \theta < 90$  deg) (Fig. 3(c)). The released axial strain of the stress fibers,  $\epsilon_{SF}$ , was calculated based on the change of the gauge lengths of the chamber,  $l_0$  and  $l$ , and the stress fiber orientation angle,  $\theta$ , as shown in Fig. 4(a).

$$\epsilon_{SF} = \frac{l_F - l_{F0}}{l_{F0}}, \quad \begin{cases} l_{F0} = \left\{ l_0^2 + \left( l \tan \theta / (\nu(l_0 - l) / l_0 + 1) \right)^2 \right\}^{1/2} \\ l_F = l / \cos \theta \end{cases} \quad (1)$$

Here,  $\nu$  is an apparent Poisson's ratio defined as  $-\epsilon_y / \epsilon_x$  at  $\epsilon_{sub} = 0.30$ . The substrate was supported by the lateral wall of the chamber, however, the substrate actually deforms elastically along the perpendicular direction to the direction of strain release because of Poisson's effect. The constant  $\nu$  at  $\epsilon_{sub} = 0.30$  was measured as 0.24. The relationship between the released axial strain of the stress fibers,  $\epsilon_{SF}$ , and the angle of stress fiber orientation,  $\theta$ , is plotted in Fig. 4(b).

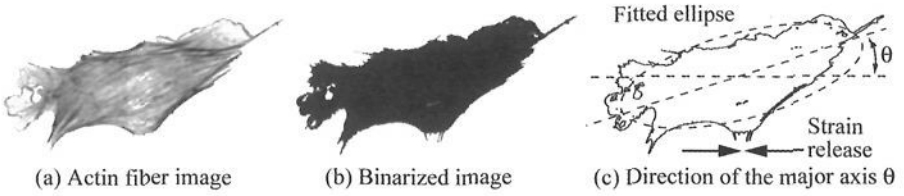


Figure 3. Procedure to define the cellular axis. (a) Fluorescent image of actin stress fibers in a single cell. (b) The image was binarized to clarify the cell outline. (c) The major axis of an ellipse fitted to the cellular outline was defined as the cellular axis. The angle between the direction of strain release and the cellular axis was defined as  $\theta$  ( $0 < \theta < 90$  deg.).

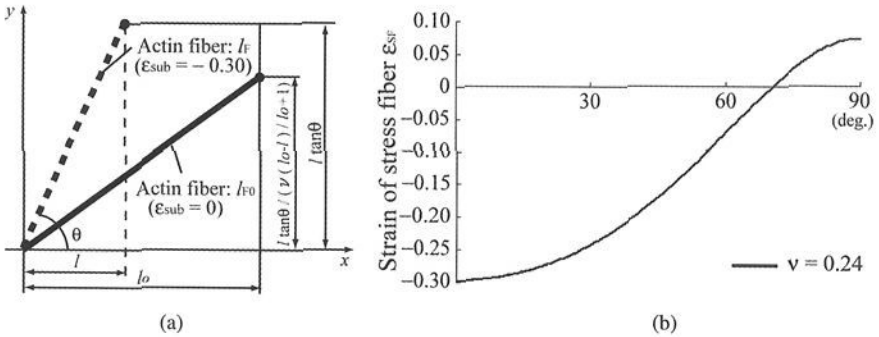


Figure 4. The axial strain of the stress fiber  $\epsilon_{SF}$  was calculated. Although uniaxial compressive strain was applied to the chamber, the substrate deformed in the direction perpendicular to the direction of strain release because of Poisson's effect.

### 2.5 Experimental protocol

Osteoblastic cells were plated on the uniaxially prestretched silicone rubber substrate in the chamber. The experimental procedure is shown in Fig. 5. In the initial prestretched state, the gauge length was defined as  $l_0$  (Fig. 5(a)). The chamber was shortened to the length of  $l$  at  $t = 0$  min (Fig. 5(b)). Consequently, the silicone rubber substrate was shortened to a state where strain was defined as  $\epsilon_{sub} = (l - l_0) / l_0$ . In this study, the released strain was set as  $\epsilon_{sub} = 0.30$  at a rate of 0.045/sec. The cell shape deforms as the substrate deforms, because osteoblastic cells adhere to the surface of the silicone rubber substrate. The cellular deformation causes the release of the preexisting intracellular tension in the stress fibers which leads to an unbalance of the mechanical equilibrium state in the cytoskeletal fiber structures. This mechanical perturbation will induce the reorganization of the stress fiber structure as shown in Fig. 5(e). The amount of actin stress fibers in the cell after the release of intracellular tension was evaluated at  $t = 15$  min (Fig. 5(c)) and analyzed in terms of the strain magnitude along the fiber axial direction  $\epsilon_{SF}$ .

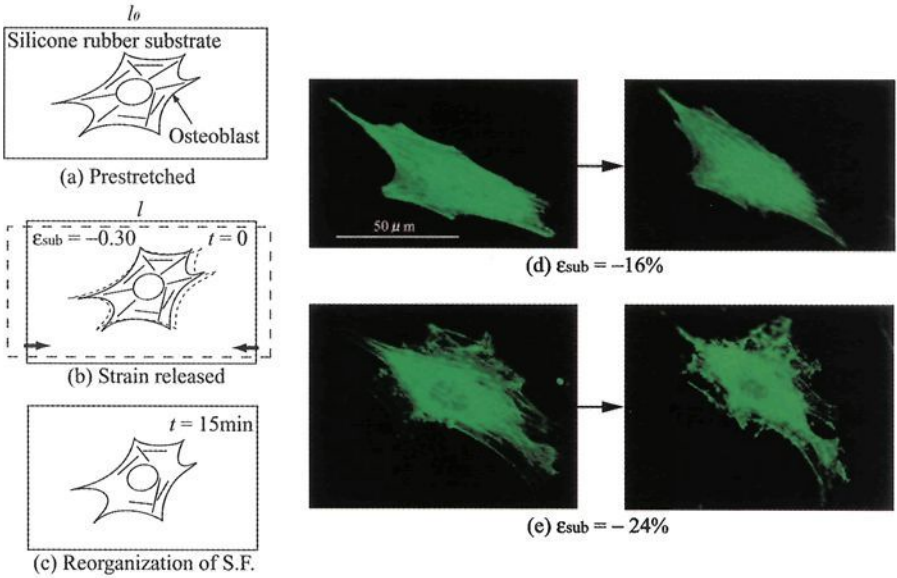


Figure 5. Schematic of experimental procedure. (a) Osteoblastic cells were plated on the prestretched silicone rubber substrate in the chamber with the gauge length  $l_0$ . (b) Tensile strain on the substrate was released to the gauge length  $l$  at  $t = 0$ . (c) The change of stress fiber (SF) structure in the reorganization process was observed at  $t = 15\text{min}$ . Strain applied to the substrate,  $\epsilon_{\text{sub}} = (l - l_0) / l_0$ , was  $-0.30$ . (d), (e) After elastic deformation, the actin fiber structure reorganized depending on the fiber strain  $\epsilon_{\text{SF}}$ . (Fluorescent image of the stress fibers were labeled by EGFP).

### 3 Results

Fluorescent images of the actin stress fibers at the bottom level in the cell are observed. In a normal cell, without any mechanical perturbation, stress fibers spread throughout the whole cell making dense network-like structure, as shown in Fig. 1. The stress fiber network has a characteristic aligned structure, the orientation of which corresponds to the major axis of the cell. Contrary to this, in a cell with strain release ( $\epsilon_{\text{sub}} = 0.30$ ), the fiber structure can be observed only in the peripheral region of the cell. In the center region of the cell, the fiber network structure cannot be observed clearly. This result revealed that strain release induces disassembly of the stress fibers as the initial phase of the reorganization process. However, not all the cells responded in this manner. For example, a cell that aligned perpendicular to the direction of strain release did not show significant disassembly of the stress fibers. That is, even though compressive strain of the same magnitude was applied to the whole cell body, not all of the cells exhibited stress fiber disassembly. This result

suggests that the release of axial fiber strain is a key determinant of the dynamic stability of the stress fiber structure.

Figure 6 shows the average fluorescence intensity of the actin stress fibers labeled by Rhodamine-Phalloidin for cells responding to different magnitudes of released axial fiber strain after 15 min. In each groups, the number of cells which were used for analysis was  $n = 13$ . Fluorescence intensities of the cells with released axial fiber strain  $\epsilon_{SF} = -0.20 \sim 0.00$  did not show any significant difference from that of the control cells. In addition, the cells with tensile axial fiber strain  $\epsilon_{SF} = 0.00 \sim 0.10$  also did not show any significant difference. In contrast, fluorescence intensities of the cells with  $\epsilon_{SF} = -0.30 \sim -0.20$  significantly decreased ( $p < 1.0 \times 10^{-7}$ ,  $t$ -test). This result demonstrates that axial strain release along the fibers is an important factor in the fiber stability that relates to cytoskeletal actin stress fiber reorganization. Quantitative evaluation of the axial strain magnitude enabled us to posit that there exists a threshold value at which fiber disassembly is induced; its value can be estimated to be about  $\epsilon_{SF} = -0.20$ .

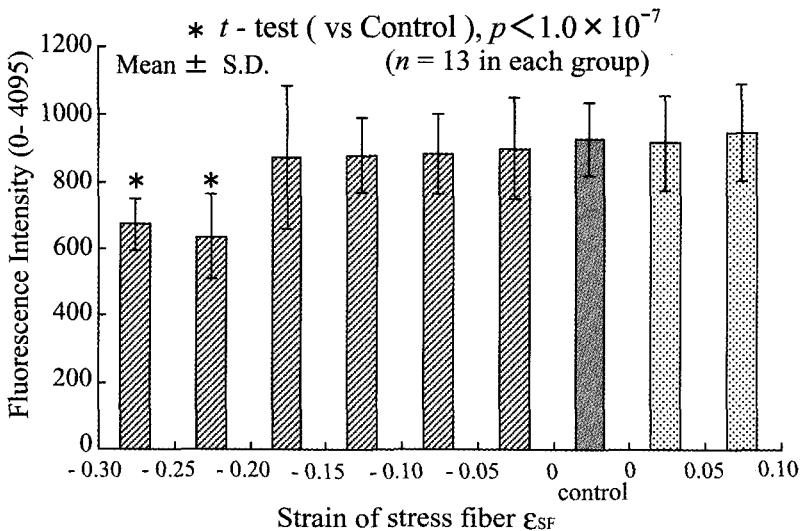


Figure 6. Relationship between the axial strain of the stress fibers ( $\epsilon_{SF}$ ) and the average fluorescence intensity of the observed actin stress fibers. The fluorescence intensity was recorded using a PC, in a 12-bit digitized format, minimum 0 to maximum 4095. In each groups, number of cells which were used for analysis was  $n = 13$ . There are no significant differences in fluorescence intensity between cells with axial strain magnitude of  $\epsilon_{SF} = -0.10 \sim 0.20$  and the control cells. In contrast, there are significant decrease in fluorescence intensity in cells with axial strain magnitude of  $\epsilon_{SF} = -0.20 \sim -0.30$ .

## 4 Discussion

In many kinds of cells, reorganization of the stress fiber structure induced by changes in the mechanical environment has been reported under quantitatively controlled mechanical strain conditions [24-26]. We found, in this study, that the threshold magnitude of the axial fiber strain that induced stress fiber disassembly was approximately  $-0.20$ . However, other researchers have reported [24,25], for example, that cyclic stretch deformation of a magnitude of approximately  $0.10$  activated biochemical signals that modulate the reorganization of the cytoskeletal actin structure, which involve integrin-related signaling paths [24] and intracellular calcium signaling paths [25]. One possible reason for the difference in the strain magnitude between our result and others is the difference in the form of the applied deformation: cyclic and transient. In addition, the observed phenomena themselves differ slightly. That is, other researchers observed the stress fiber structure after the completion of the reorganization, whereby the fiber orientation had been rearranged [26]. On the contrary, we focused on the disassembly of the stress fibers, which can be considered as the initial phase of the reorganization process. In actin stress fibers, polymerization and depolymerization of monomeric actin molecules take place continuously, and the structure is maintained under the dynamic equilibrium of these coupling assembly and disassembly reactions. Therefore, results in other studies likely include the influence of assembly factors that act in later phases of reorganization.

Many studies have indicated that osteoblastic cells can sense mechanical stimuli to which they respond in various ways. Such cellular responses arise due to the intracellular transmission of the mechanical stimulation into biochemical signaling cascades. In the same way, the disassembly of the stress fibers observed in this study seems to appear due to such activation of biochemical signaling. Therefore, there is a possibility that the threshold strain magnitude evaluated in this study only indicates the threshold of cellular mechano-sensitivity, that is, the threshold mechanical value at which biochemical signaling cascades are activated. However, in this study, there were two groups of cells, those exhibiting disassembly of stress fibers and those that did not, even though we applied uniaxial compressive strain of the same magnitude ( $\epsilon_{\text{sub}} = -0.30$ ) to the whole cell body. This result suggests that, not the strain applied to the cell body, but the axial fiber strain is the key determinant of stress fiber stability. In addition, in another experimental study [20], we proposed an experimental technique by which we can selectively apply local contraction to release the intracellular tension of the targeted stress fiber in a single cell. The result observed in this experiment revealed that only the tension-released stress fiber was disassembled in a single cell, even though biochemical signals, such as intracellular calcium signaling are activated in the whole cell body. This result also supports our suggestion that axial strain release is the key mediator of stress fiber stability.

We have shown that axial strain release of the stress fibers induces disassembly of the stress fiber structure, and that there is a threshold strain magnitude for the initiation of this phenomenon. It is important to discuss the physical meaning of the threshold strain magnitude. In the reorganization process, many biochemical factors play important roles in the modulation of the actin structure. It is known that some proteins sever filaments by directly associating with the actin filament itself, while some proteins inhibit the actin polymerization by capping the plus end of the filaments, and other proteins modulate the balance between actin polymerization and depolymerization by associating with the monomeric actin molecule pool in cytosol [27]. Our results revealed that the axial fiber strain is the key determinant of the filament stability, so that the proteins directly associating with the stress fibers is suggested to be a main player in this disassembly mechanism. For example, a new hypothesis can be proposed here: the release of axial fiber strain might induce the conformational change of the actin filament or monomeric actin molecule itself, and this conformational change consequently might affect the affinity of the actin depolymerizing factors with actin filament. The examination of this hypothesis will be the next challenge to further the understanding of the mechanics-related cytoskeletal stress fiber dynamics.

## **Acknowledgments**

I wish to thank Mr. M. Matsuo for his technical assistance, and Prof. Y. Tomita at Kobe University and Prof. M. Hojo at Kyoto University for their helpful comments. This work was supported financially in part by Grants-in-Aid for Scientific Research on Priority Areas 15086211 from the Ministry of Education, Culture, Sports, Science and Technology of Japan.

## **References**

1. Duncan, R.L., Turner, S.H., 1995. Mechanotransduction and the functional response of bone to mechanical strain. *Calcified Tissue International* 57, 344-358.
2. Duncan, R.L., Akanbi, K.A., Frach-Carson, M.C., 1998. Calcium signals and calcium channels in osteoblast cells. *Seminars in Nephrology* 18, 178-190.
3. Toma, C.D., Ashkar, S., Gray, M.L., Schaffer, J.L., Gerstenfeld, L.C., 1997. Signal transduction of mechanical stimuli is dependent on microfilament integrity: Identification of osteopontin as a mechanically induced gene in osteoblasts. *Journal of Bone Mineral Research* 12-10, 1626-1636.
4. Adachi, T., Sato, K., Tomita, Y., 2003. Directional dependence of osteoblastic calcium response to mechanical stimuli. *Biomechanics and Modeling in Mechanobiology* 2-2, 73-82.



5. Buckley, M.J., Banes, A.J., Levin, L.G., Sumpio, B., Sato, M., Jordan, R., Gilbert, J., Link, G.W., Tran Son Tay, R., 1998. Osteoblasts increase their rate of division and align in response to cyclic, mechanical tension in vitro. *Bone and Mineral* 4-3, 225-236.
6. Wang, H.-C.J., Grood, E.S., Florer, J., Wenstrup, R., 2000. Alignment and proliferation of MC3T3-E1 osteoblasts in microgrooved silicone substrata subjected to cyclic stretching. *Journal of Biomechanics* 33, 729-735.
7. Neidlinger-Wilke, C., Grood, E.S., Wang, J.H.-C., Brand, R.A., Claes, L., 2001. Cell alignment is induced by cyclic changes in cell length: Studies of cell grown in cyclically stretched substrates. *Journal of Orthopaedic Research* 19, 286-293.
8. Chen, N.X., Ruder, K.D., Pavalko, F.M., Turner, C.H., Burr, D.B., Qiu, J., Duncan, R.L., 2000.  $\text{Ca}^{2+}$  regulates fluid shear-induced cytoskeletal reorganization and gene expression in osteoblasts. *American Journal of Physiology. Cell Physiology* 278, C989-C997.
9. Costa, K.D., Hucker, W.J., Yin, F.C.-P., 2002. Buckling of actin stress fibers: A new wrinkle in the cytoskeletal tapestry. *Cell Motility and the Cytoskeleton* 52, 266-274.
10. Huang, S., Ingber D.E., 1999. The structural and mechanical complexity of cell-growth control. *Nature Cell Biology* 1, E131-138.
11. Pelham, R., Wang, Y.L., 1997. Cell locomotion and focal adhesions are regulated by substrate flexibility. *Proceedings of National Academy Science of USA* 94, 13661-13665.
12. Shyy, J., Chien, S., 1997. Role of integrins in cellular responses to mechanical stress and adhesion. *Current Opinion in Cell Biology* 9, 707-713.
13. Harris, A., Stopak, D., Wild, P., 1981. Fibroblast traction as a mechanism for collagen morphogenesis. *Nature* 290, 249-251.
14. Zhong, C., Chrzanowska-Wodnicka, M., Brown, J., Shaub, A., Belkin, A., Burrige, K., 1998. Rho-mediated contractility exposes a cryptic site in fibronectin and induces fibronectin matrix assembly. *Journal of Cell Biology* 141, 539-551.
15. Grinnell, F., Zhu, M., Carlson, M., and Abrams, J., 1999. Release of mechanical tension triggers apoptosis of human fibroblasts in a model of regressing granulation tissue. *Experimental Cell Research* 248, 608-619.
16. Langanger, G., Moeremans, M., Dancels, G., Sobieszek, A., De Brabander, M., De Mey, J., 1986. The molecular organization of myosin in stress fibers of cultured cells. *Journal of Cell Biology* 102, 200-209.
17. Burrige, K., 1981. Are stress fibers contractile?, *Nature* 294, 691-692.
18. Kojima, H., Ishijima, A., Yanagida, T., 1994. Direct measurement of stiffness of single actin filaments with and without tropomyosin by in vitro manipulation. *Proceedings of National Academy of Science USA* 91, 12962-12966.
19. Neumann, T., Fauver, M., Pollack, G., 1998. Elastic properties of isolated thick filaments measured by nanofabricated cantilevers. *Biophysical Journal* 75, 938-947.

20. Sato, K., Adachi, T., Tomita, Y., 2004. Reorganization of stress fibers induced by selective tension release in osteoblastic cell. In Proceedings of the 16th Bioengineering Conference JSME 03-38, 9-10.
21. Galbraith, C. G., Sheetz, M. P., 1997. A micromachined device provides a new bend on fibroblast traction forces. Proceedings of National Academy of Science USA 94, 9114-9118.
22. Dembo, M., Wang, Y. L., 1999. Stresses at the cell-to-substrate interface during locomotion of fibroblasts. Biophysical Journal 76, 2307-2316.
23. Sato, K., Adachi, T., Matsuo M., Tomita, Y., 2005. Quantitative evaluation of threshold fiber strain that induces reorganization of cytoskeletal actin fiber structure in osteoblastic cells. Journal of Biomechanics 38, 1895-1901.
24. Gunst, S., Tang, D., Saez, A., 2003. Cytoskeletal remodeling of the air smooth muscle cell: a mechanism for adaptation to mechanical forces in the lung. Respiratory physiology and Neurobiology 137, 151-168.
25. Naruse, K., Sokabe, M., 1993. Involvement of stretch-activated ion channels in  $Ca^{2+}$  mobilization to mechanical stretch in endothelial cells. American Journal of Physiology 264, C1037-1044.
26. Yoshigi, M., Clark, E., Yost, H., 2003. Quantification of stretch-induced cytoskeletal remodeling in vascular endothelial cells by image processing. Cytometry Part A, 55A, 109-118.
27. Bray, D., 2001. Cell movements -From molecules to motility- 2nd edition, Garland, New York, pp. 63-81.

# MORPHOLOGY OF ENDOTHELIAL CELLS IN RESPONSE TO HYDROSTATIC PRESSURE

M. SATO

*Department of Biomengineering and Robotics, Tohoku University,  
6-6-01 Aoba-yama, Sendai 980-8579, Japan  
E-mail: sato@bml.mech.tohoku.ac.jp*

Morphological responses of cultured bovine endothelial cells (ECs) exposed to hydrostatic pressure were investigated. ECs were exposed to physiological blood pressure under a hydrostatic head of culture medium for 24 h. Pressured ECs exhibited marked elongation and orientation with the random direction, together with development of centrally located, thick stress fibers. Pressured ECs also exhibited multilayered structure unlike under control conditions. The area and the shape index value significantly decreased after exposure to hydrostatic pressure, which was in good agreement with the results from conventional flow-imposed experiments. In contrast, a tortuosity index, which was newly introduced to represent cell shape tortuosity, significantly increased for pressured ECs, while sheared ECs had no difference in tortuosity index from control. In addition, pressured ECs aligned with no predominant direction, while sheared ECs aligned in the flow direction. These results indicate that ECs can respond very specifically to the type of imposed mechanical stimuli such as hydrostatic pressure and fluid shear stress.

## 1 Introduction

Vascular endothelial cells (ECs) play important roles in physiology and pathology of blood vessel walls. ECs have a large variety of physiological functions to support our life, for example, regulation of permeability between blood and surrounding tissues, coagulation of blood, transmigration of leukocytes, and regulation of vessel diameter. For their anatomical location, ECs are exposed to hemodynamic forces *in vivo*: shear stress due to blood flow and hydrostatic pressure due to blood pressure. These mechanical forces are important factors of remodeling in EC morphology [1]. Morphological changes elicited by mechanical stresses are known to influence several aspects of EC biology that are critical to normal endothelium functions [2]. Therefore, the effects of hemodynamic forces on EC morphology and cytoskeletal structure have been studied.

A large number of studies have previously been reported to evaluate the effects of shear stress [3-5] on EC structure because blood vessels would have experienced complex blood flow such as boundary layer separation and secondary flow in the preferential regions of atherosclerosis. For example, Nerem et al. [3] have quantified time course of changes in morphology of bovine aortic ECs exposed to shear stress and have shown that ECs elongated and aligned to the flow direction depending on the level of shear stress and exposure duration. In contrast, few studies have been reported to evaluate the effects of hydrostatic pressure on EC morphology so far.

Acevedo et al. [6] have reported that after exposure to hydrostatic pressure of 12 mm Hg for 7 days, bovine pulmonary artery ECs showed elongation without predominant cell orientation and the cytoskeletal reorganization with the formation of multilayer. Salwen et al. [7] have also demonstrated elongation and multilayering of bovine pulmonary artery ECs exposed to sustained hydrostatic pressure of 8 mm Hg for 7 days. These studies used pulmonary artery ECs, and therefore in the pressure range of several mm Hg and higher. From the viewpoint of vascular disease such as atherosclerosis, it would be necessary to use arterial ECs in the pressure range of around 100 mm Hg. Sumpio et al. [8] have reported that bovine aortic ECs under sub-confluent conditions were elongated and randomly orientated after exposure to hydrostatic pressure of 80 mm Hg.

In this report, I summarized our published data [9] on cytoskeletal structures of confluent bovine aortic ECs exposed to hydrostatic pressures of 50, 100 and 150 mm Hg for 24 h. In addition, since shear stress together with hydrostatic pressure affects EC morphology *in vivo*, we also compared pressured ECs with sheared ECs in morphology to examine the morphological dependence of ECs on different mechanical stimuli.

## 2 Methods

### 2.1 Endothelial cells

ECs were obtained from bovine thoracic aortas and cultured according to standard cell culture techniques. The culture medium consisted of Dulbecco's Modified Eagle medium (Invitrogen, USA) supplemented with 10% heat-inactivated fetal bovine serum (JRH Biosciences, USA), and penicillin-streptomycin (Invitrogen, USA). For hydrostatic pressure-imposed experiments, ECs were plated on a cell culture dish of 35mm in diameter (Asahi Techno Glass, Japan) and cultured until reaching confluence.

### 2.2 Hydrostatic pressure-imposed experiments

The hydrostatic pressure-imposed system consists of a damping chamber, a flow chamber, a reservoir, and a roller pump (Master Flex, USA). These are connected with silicone tubes. The flow chamber is composed of the cell culture dish, an I/O unit, and a gasket with the thickness of 1mm. The height of the reservoir can be adjustable to apply hydrostatic pressure to EC monolayer in the flow chamber. Pulsatile part of fluid flow produced by the roller pump is eliminated by a damping chamber. During experiments, the temperature of culture medium was maintained at 37°C by soaking the damping chamber in a thermostatic chamber and pH by pumping mixed gas (5% CO<sub>2</sub>/ 20% O<sub>2</sub>/ 75% N<sub>2</sub>). Using this system, hydrostatic pressure of 50, 100 and 150 mm Hg was applied to ECs for 24 h to roughly

represent diastolic, mean, systolic blood pressures. It should be noted that very slow fluid flow with shear stress less than 0.1 Pa was applied to ECs to perfuse nutrients and oxygen. It has been confirmed that shear stress less than 0.5 Pa does not induce any morphological changes in ECs [10]. In a separate study, we performed conventional flow-imposed experiments to compare with hydrostatic pressure-imposed experiments. A detailed description of flow-imposed experiments has been reported elsewhere [11, 12]. A fluid shear stress of 2 Pa was applied to EC monolayer for 24 h using the same experimental system. As control, ECs were statically cultured in a standard incubator under atmospheric pressure.

### 2.3 Fluorescence staining

The fluorescence staining of F-actin filaments was performed as follows. Briefly, ECs after exposure to hydrostatic pressure were fixed with 10 % formaldehyde for 5 min. Then, ECs were stained with 150 nM concentration of rhodamine-phalloidin for 20 min. A confocal laser scanning microscope (Olympus, Japan) was used to observe distribution of F-actin filaments of ECs in all experimental conditions.

### 2.4 Morphological analysis

Morphological analysis was performed on ECs to evaluate parameters such as area, the shape index (SI) [13], a tortuosity index and the angle of cell orientation.

Figure 1 shows the protocol for EC morphological analysis. The cell outline was manually extracted by tracing outsides of peripheral thick actin filaments in fluorescent images with the public domain NIH Image program version 1.62 (National Institute of Health, USA) (a). Cell area and cell perimeter were then measured automatically (b). In addition, an equivalent ellipse for the cell outline, which has the equal area and the equal moment of inertia corresponding to the extracted cell shape, was also determined (c). The angle of cell orientation is defined as the deviation of the major axis of equivalent ellipse from the flow direction. For control cells, the horizontal direction from left to right in the images was defined as 0°. The shape index is defined as follows.

$$\text{Shape index} = 4\pi A / P^2 \quad (1)$$

where  $A$  is the cell area,  $P$  the cell perimeter. The shape index is defined as 1.0 for the circle and approaches zero for highly elongated shape. The tortuosity index is newly defined [9] as follows.

$$\text{Tortuosity index} = P / P' \quad (2)$$

where  $P$  is the cell perimeter and  $P'$  the equivalent ellipse perimeter of the cell. The tortuosity index increases from 1.0 when the cell shape becomes more tortuous, while the tortuosity index is 1.0 when the circle or the ellipse.

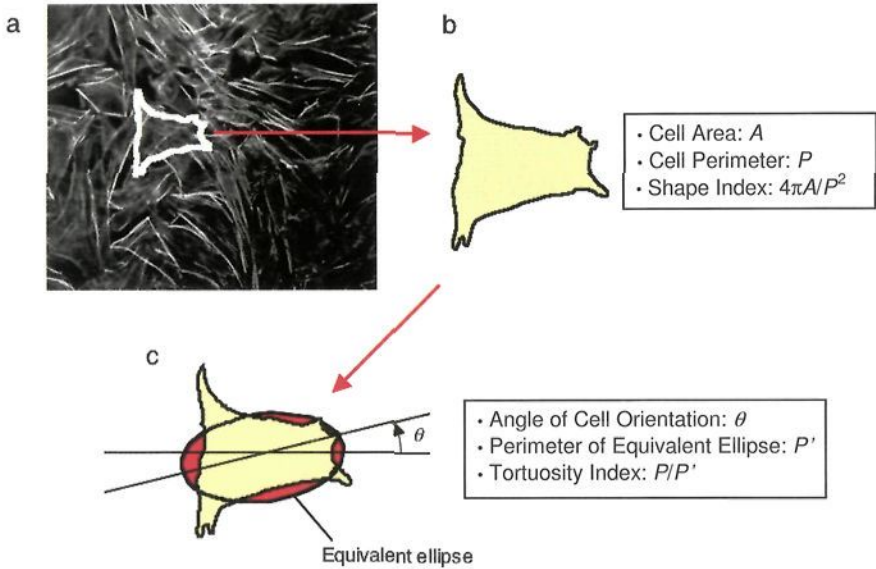


Figure 1. The protocol of determining morphological parameters of ECs. Reprinted from [9] with permission from JSME.

### 2.5 Statistical analysis

Statistical comparisons were made using unpaired Student's  $t$ -test and unpaired Welch's  $t$ -test for equal variance and unequal variance, respectively. A value of  $p < 0.05$  was considered significant in all analyses. Statistical data were shown in terms of the mean  $\pm$  standard deviation (mean  $\pm$  SD).

## 3 Results

Time course of changes in morphology of ECs under sheared and pressured conditions was observed with a phase contrast microscope, as shown in Fig. 2. The same cell is enclosed with black line in the center of each figure. At 3 h, pressured ECs seemed to contract without any apparent elongation (b). The same tendency was observed for sheared ECs (f). At 6 h, ECs showed an increase in cell areas (c, g). At 24 h, sheared ECs then elongated and oriented in the direction of flow (h), while pressured ECs elongated and randomly oriented (d). It should be noted that ECs

showed active migration during exposure to hydrostatic pressure and shear stress. Interestingly, some of pressured ECs repeated this time course of changes several times during 24 h.

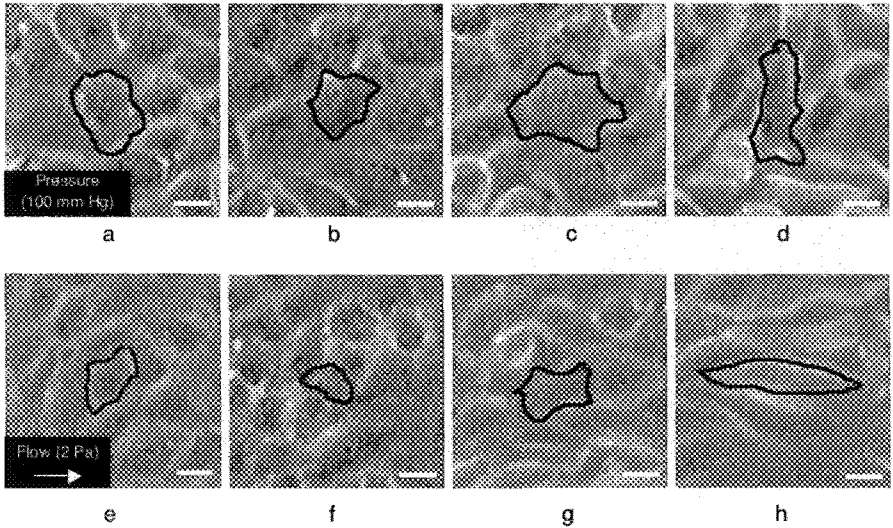


Figure 2. Typical morphological changes in ECs exposed to hydrostatic pressure of 100 mm Hg (a, b, c, d) and shear stress of 2 Pa (e, f, g, h). (a, e) 0h, (b, f) 3 h, (c, g) 6 h and (d, h) 24 h. Bar = 20  $\mu$ m. Reprinted from [9] with permission from JSME.

Typical fluorescence images of rhodamine-phalloidin stained ECs are shown in Fig. 3 for (a) control, (b) hydrostatic pressure of 100 mm Hg for 24 h, and (c) shear stress of 2 Pa for 24 h. Similar images to hydrostatic pressure of 100 mm Hg were obtained for 50 and 150 mm Hg hydrostatic pressure. For control cells, ECs exhibited a rounded shape, and thin and short F-actin filaments were observed centrally with web-like configurations. In contrast, exposure to hydrostatic pressure resulted in cell elongation with no predominant orientation. Distinctive differences were also seen in the F-actin filament structures. Pressured ECs exhibited centrally (arrow head) and peripherally (arrows) located long and thick filaments, which aligned with the cell major axis. Moreover, the cells proliferated in the three-dimensional directions and exhibited multilayered structure. Sheared ECs showed elongation and alignment with the flow direction, together with development of centrally located thick stress fibers. The area, the shape index, the tortuosity index, and the angle of cell orientation are summarized in Table 1 for the three pressured conditions. There were significant differences in the changes in morphological parameters between control and the three pressure conditions.

The area, the shape index, and the tortuosity index are summarized in Fig. 4 for control, pressured, and sheared ECs. Both the area and the shape index significantly

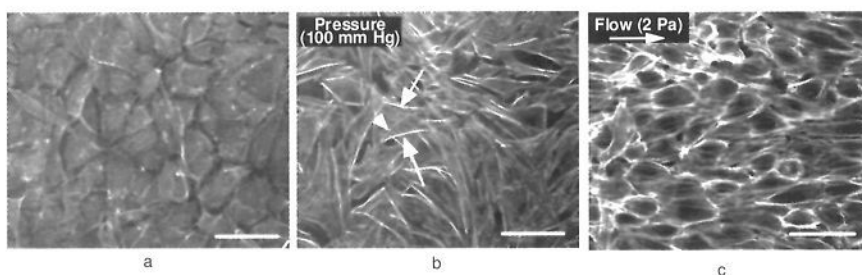


Figure 3. Typical fluorescence images of rhodamine-phalloidin stained ECs for (a) control, (b) hydrostatic pressure of 100 mm Hg for 24 h, (c) shear stress of 2 Pa for 24 h. Bar = 50  $\mu\text{m}$ . Arrow and arrow head represent actin filaments located peripherally and centrally, respectively. Reprinted from [9] with permission from JSME.

Table 1. Morphological parameters of ECs exposed to hydrostatic pressure of 50, 100 and 150 mm Hg. \*  $p < 0.05$  vs. control. Reprinted from [9] with permission from JSME.

Pressure	Area [ $\mu\text{m}^2$ ]	Shape Index	Tortuosity Index	Angle of cell orientation [deg]
Control	718 $\pm$ 178	0.86 $\pm$ 0.06	1.04 $\pm$ 0.03	0.6 $\pm$ 50.2
50 mm Hg	641 $\pm$ 126*	0.46 $\pm$ 0.10*	1.32 $\pm$ 0.14*	16.1 $\pm$ 59.8
100 mm Hg	620 $\pm$ 98*	0.36 $\pm$ 0.16*	1.27 $\pm$ 0.14*	12.2 $\pm$ 48.0
150 mm Hg	638 $\pm$ 107*	0.51 $\pm$ 0.10*	1.26 $\pm$ 0.10*	-1.7 $\pm$ 57.4

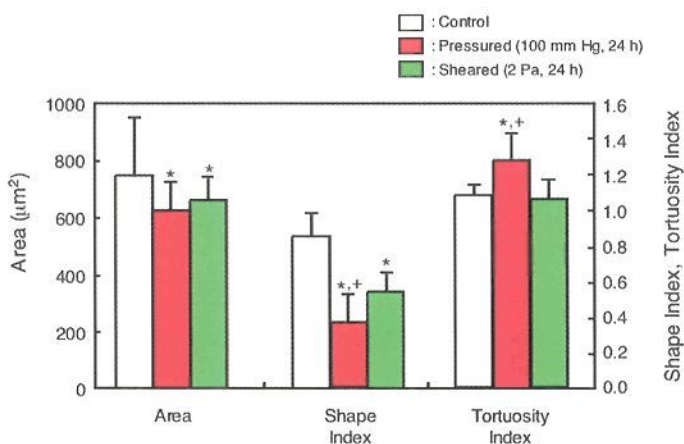


Figure 4. Morphological parameters of ECs exposed to hydrostatic pressure of 100 mm Hg for 24 h and shear stress of 2 Pa for 24 h. \*  $p < 0.05$  vs. control. +  $p < 0.05$  vs. sheared. Reprinted from [9] with permission from JSME.



decreased under pressured and sheared conditions. In contrast, the tortuosity index for pressured cells significantly increased compared with control. There are also significant differences in shape index and tortuosity index between sheared and pressured conditions ( $p < 0.05$ ).

Distributions of the angle of cell orientation are shown in Fig. 5 for the three groups. The angle for pressured ECs was distributed almost uniformly, which was similar to that for control. In contrast, the SD for sheared ECs was significantly smaller than that for the other two groups and centered nearly on the  $0^\circ$ .

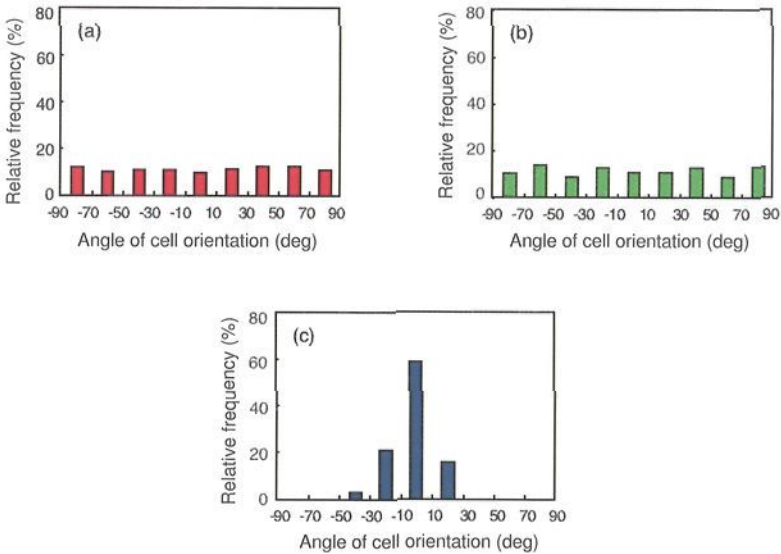


Figure 5. Histograms of angle of cell orientation. (a) control, (b) hydrostatic pressure of 100 mm Hg for 24 h, and (c) shear stress of 2 Pa for 24 h. Reprinted from [9] with permission from JSME.

#### 4 Discussion

The present study investigated morphological changes and cytoskeletal rearrangement of cultured ECs exposed to physiological hydrostatic pressures of 50, 100 and 150 mm Hg for 24 h. These results were compared with those obtained from a conventional flow-imposed experiment. For the result of time course of change in morphology, ECs firstly showed contraction after exposure to shear stress and hydrostatic pressure. As following changes, ECs elongated and oriented to the flow direction under sheared condition. In contrast, pressured ECs also elongated

but showed no predominant orientation. The observation of cytoskeletal structures clarified detail differences in morphology between sheared and pressured ECs. Under hydrostatic pressure, ECs exhibited long and thick filaments, concomitant elongation with no predominant orientation, and multilayering (Fig. 3b). In contrast, sheared ECs elongated and aligned with the flow direction, developing thick stress fibers (Fig. 3c). Thus, ECs responded uniquely in accordance to each mechanical stimulus. Among the three pressure conditions, the same characteristic of morphology was observed and morphological analysis showed no significant differences (Table 1).

Sumpio et al. [8] reported that ECs were elongated and aligned randomly under 80 mm Hg for 9 days but did not form multilayer. In their experiment, since ECs were exposed to hydrostatic pressure after cells were seeded and allowed to attach for 24 h, ECs did not reach confluent. It has also been known that ECs form cell to cell contact, *i.e.* intercellular adhesion, in confluent conditions. Therefore, intercellular adhesion may have an important role in morphological response of ECs to hydrostatic pressure.

Acevedo et al. [6] and Salwen et al. [7] have exposed bovine pulmonary artery ECs to up to 12 mm Hg for 7 days and have shown the EC elongation and the formation of multilayer. Although there were differences in pressure level and exposure time between present study and their studies, the similar tendency such as multilayering was obtained. This result may indicate that multilayering does not depend on locations where ECs exist, but depends on cell density conditions together with the combined effects of shear stress and hydrostatic pressure.

Under pressured conditions, the area and shape index significantly decreased, which showed the similar tendency to those under sheared conditions (Fig. 4). Although the tortuosity index significantly increased under pressured conditions, the index was almost constant under sheared conditions. In addition, distributions of the angle of cell orientation were quite different between the two mechanical conditions (Fig. 5). In the previous study [11], Ohashi et al. have suggested through numerical simulations that F-actin filaments might be rearranged in accordance to intracellular stress distributions under flow conditions, *i.e.* development of stress fibers could be observed around a region of stress concentration. To take this into consideration, the mechanism of cell responses to hydrostatic pressure can be assumed as follows. When exposure to hydrostatic pressure, nonuniformity in intracellular stress state occurs or increases due to nonuniformity in initial cell morphology and cytoskeletal structure. Then, the cytoskeleton develops to reduce the stress concentrations, followed by cell elongation until desired stress state will be reached. Since this is just the hypothesis, it requires further study to elucidate the mechanism.

ECs do not continue to grow after they have formed a confluent monolayer, which is known as contact inhibition. However, in this study, pressured ECs piled up on top of one another and formed multilayer unlike under *in vivo* conditions. Vascular endothelial growth factor (VEGF), which is an endothelium-specific

mitogen, may associate with multilayering of ECs. It is known that VEGF induces EC proliferation, migration and differentiation. Confluent ECs were found to respond poorly to the proliferative signals of VEGF [14]. It was also shown that gene expression of VEGF-2 is pressure sensitive [15]. Taken together, hydrostatic pressure might enhance synthesis of VEGF production of ECs and then increase cell proliferation. In addition, it was reported that VEGF stimulates dephosphorylation of catenins, which associate with VE-cadherin and localize to adherens junctions [16]. Adherens junctions, which mechanically connect and provide the structural base for interendothelial mechanical stability, have an important role in contact inhibition. Pressure-induced VEGF may decrease formation of adherens junction and induce inefficiency in contact inhibition, resulting in multilayering of ECs. On the other hand, it was demonstrated that physiological arterial shear stress of 1.5 Pa decreased VEGF synthesis of porcine arterial ECs [17]. Although, *in vivo*, ECs are exposed to both shear stress and hydrostatic pressure, multilayering has never been observed as far as our knowledge. The combined effect may alter the role of VEGF to ECs, but the mechanism is still unclear.

## Acknowledgments

I wish to thank Drs. T. Ohashi and N. Sakamoto and Mr. Y. Sugaya for their superb researches adopted in this paper. This work was supported financially in part by the Grants-in-Aid for Scientific Research (A) 14208100, Priority Areas 15086203 and the 21st Century Programme “Future Medical Engineering Based on Biotechnology” granted to the Tohoku University by the Ministry of Education, Culture, Sports, Science and Technology (MEXT) in Japan.

## References

1. Nerem, R.M., 1993. Hemodynamics and the vascular endothelium. *Trans. ASME J. Biomech. Eng.* 115, 510–514.
2. Davies, P.F., 1995. Flow-mediated endothelial mechanotransduction. *Physiol. Rev.* 75, 519–560.
3. Nerem, R.M., Levesque, M.J., Cornhill, J.F., 1981. Vascular endothelial morphology as an indicator of the pattern of blood flow. *Trans. ASME J. Biomech. Eng.* 103, 172-176.
4. Kataoka, N., Ujita, S., Sato, M., 1998. Effect of flow direction on the morphological response of cultured bovine aortic endothelial cells. *Med. Biol. Eng. Comp.* 36, 122–128.
5. Levesque, M.J., Nerem, R.M., 1985. The elongation and orientation of cultured endothelial cells in response to shear stress. *Trans. ASME J. Biomech. Eng.* 107, 341–347.

6. Acevedo, A.D., Bowser, S.S., Gerritsen, M.E., Bizios, R., 1993. Morphological and proliferative responses of endothelial cells to hydrostatic pressure: Role of fibroblast growth factor. *J. Cell. Physiol.* 157, 603–614.
7. Salwen, S.A., Szarowski, D.H., Turner, J.N., Bizios, R., 1998. Three-dimensional changes of the cytoskeleton of vascular endothelial cells exposed to sustained hydrostatic pressure. *Med. Biol. Eng. Comput.* 36, 520–527.
8. Sumpio, B.E., Widmann, M.D., Ricotta, J., Awolesi, M.A., Watase, M., 1994. Increased ambient pressure stimulates proliferation and morphologic changes in cultured endothelial cells. *J. Cell. Physiol.* 158, 133–139.
9. Sugaya, Y., Sakamoto, N., Ohashi, T., Sato, M., 2003. Elongation and random orientation of bovine endothelial cells in response to hydrostatic pressure: comparison with response to shear stress. *JSME Int. J., Ser C*, 46, 1248-1255.
10. Dewey, C.F., Jr., Bussolari, S.R., Gimbrone, M.A.Jr., Davies, P.F., 1981. The dynamic response of vascular endothelial cells to fluid shear stress. *J. Biomech. Eng.* 103, 177–184.
11. Ohashi, T., Sugawara, H., Matsumoto, T., Sato, M., 2000. Surface topography measurement and intracellular stress analysis of cultured endothelial cells exposed to fluid shear stress. *JSME Int. J. Ser. C* 43, 780-786.
12. Sato, M., Nagayama, K., Kataoka, N., Sasaki, M., Hane, K., 2000. Local mechanical properties measured by atomic force microscopy for cultured bovine endothelial cells exposed to shear stress. *J. Biomech.* 33, 127–135.
13. Cornhill, J.F., Levesque, M.J., Herderick, E.E., Nerem, R.M., Kilman, J.W., Vasco, J.S., 1980. Quantitative study of the rabbit aortic endothelium using vascular casts. *Atherosclerosis* 35, 321–337.
14. Grazia, L.M., Zanetti, A., Corada, M., Takahashi, T., Balconi, G., Braviario, F., Orsenigo, F., Cattelino, A., Kemler, R., Daniel, T.O., Dejana, E., 2003. Contact inhibition of VEGF-induced proliferation requires vascular endothelial cadherin,  $\beta$ -catenin, and the phosphatase DEP-1/CD148. *J. Cell. Biol.* 161, 793–804.
15. Shin, H.Y., Smith, M.L., Toy, K.J., Williams, P.M., Bizios, R., Gerritsen, M.E., 2002. VEGF-C mediates cyclic pressure-induced endothelial cell proliferation. *Physiol. Genomics.* 11, 245–251.
16. Wong, E.Y., Morgan, L., Smales, C., Lang, P., Gubby, S.E. and Staddon, J.M., 2000. Vascular endothelial growth factor stimulates dephosphorylation of the catenins p120 and p100 in endothelial cells. *Biochem. J.* 346, 209–216.
17. Conklin, B.S., Zhong, D-S., Zhao, W., Lin, P.H., Chen, C., 2002. Shear stress regulates occludin and VEGF expression in porcine arterial endothelial cells. *J. Sur. Res.* 102, 13–21.

# MECHANOSENSING IN INTESTINAL VILLI: ATP SIGNALING IN SUBEPITHELIAL FIBROBLASTS NETWORK

K. FURUYA<sup>1</sup>, S. FURUYA<sup>2</sup> AND M. SOKABE<sup>1,3,4</sup>

<sup>1</sup>Cell-mechanosensing Project, ICORP and SORST, Japan Science and Technology Agency, Nagoya 466-8550, Japan; <sup>2</sup>Center for Brain Experiment and <sup>3</sup>Department of Molecular Physiology, National Institute for Physiological Sciences, Okazaki 444-8585, Japan;

<sup>4</sup>Department of Physiology, Nagoya University Graduate School of Medicine, Nagoya, 466-8550, Japan

E-mail: furuya@med.nagoya-u.ac.jp

Uptake of food, water and nutrients may cause mechanical stress on the intestinal villi that regulates villous and intestinal motilities and digestive functions. However, the mechanism of mechanosensing in intestine is not yet clear. We pay attention a cellular system, subepithelial fibroblasts, that form a cellular network just under the epithelium of the gastrointestinal tract. Using primary cultured cells isolated from rat duodenal villi, we previously found that subepithelial fibroblasts had many kinds of receptors for vaso- and neuro-active substances, such as endothelins (ETs), ATP, serotonin, and that they reversibly changed cell morphology between flat and stellate-shape depending on intracellular cAMP levels. Recently we found that subepithelial fibroblasts were sensitive to mechanical stress such as “touching” and “stretching”. Mechanical stimulations evoked Ca<sup>2+</sup>-increase in the cells and ATP-release from the cells. The released ATP activated P2Y1 type ATP receptors on the surrounding cells and propagated Ca<sup>2+</sup>-waves through the network. Concomitant with Ca<sup>2+</sup>-waves, a transient contraction of the network was observed. ATP-release and Ca<sup>2+</sup> signaling were cell-shape dependent, i.e., they were abolished in stellate-shaped cells treated with dBcAMP, and recovered or further enhanced in re-flattened cells treated with ETs. From these unique properties, we propose that subepithelial fibroblasts work as a mechano-sensor in the intestine, and as a regulator of mechanical property and movement of the villi.

## 1 Introduction

The gastrointestinal tract is not only regarded as a digestive and an immune organ but also as a sensory organ [1]. Food and water uptake and their digestion may give rise to chemical and mechanical signals that induce the peristaltic reflex in the gut. Chemical and mechanical signals control motility, secretion and immune defenses in local and/or central neural and/or non-neural pathways [1, 2, 3]. Even in isolated gut, distension caused by intraluminal hydrostatic pressure induces peristalsis [4] and there seems to exist mechano-sensors in mucosa, submucosa and muscle layer including myenteric plexus. However, the mechanosensing machinery is not yet fully elucidated.

The luminal surface of the intestine forms villous structure (Figure 1A). The intestinal villi are not simple amplifiers of the mucosal surface to absorb nutrients, but rather are functional units which resolve contradictory functional demands such

as a smooth transfer and a long-term folding of the content of digesting food. Although the fact that intestinal villi exhibit motility was first noted in 19th century, how these flexible, graceful and bendable properties of intestinal villi are achieved is still obscured [5, 6, 7, 8].

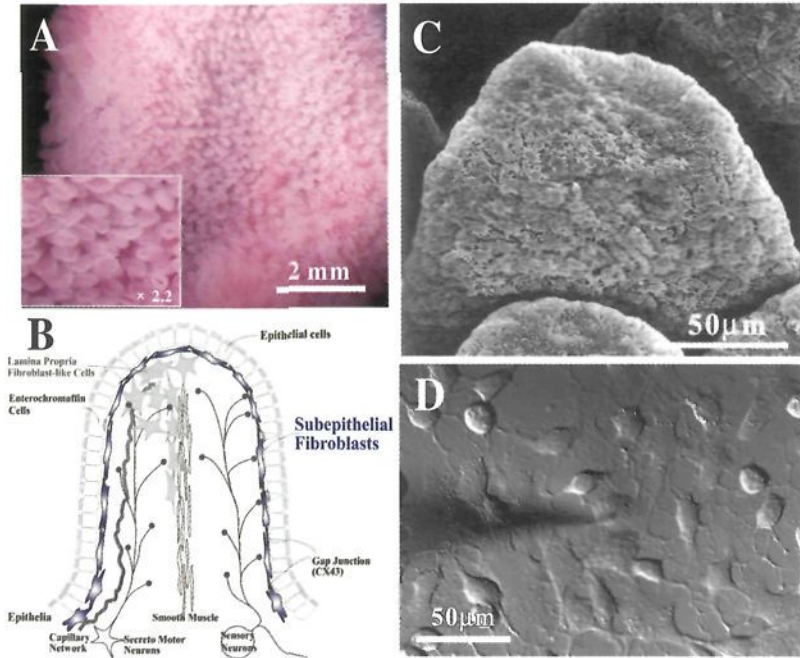


Figure 1. Intestinal villi and subepithelial fibroblasts. **A:** Villous structure covering all over inner surface of intestine (mouse duodenum). Shapes of villi exhibit two forms, fingerlike and leaflike, depending on the species. Rat and mouse we used here have the leaflike villi. **B:** A schema of intestinal villi. Subepithelial fibroblasts locate just under the epithelium and form a cellular network. The network connects with epithelium, capillary, smooth muscle and neural networks. **C:** Scanning electron micrograph of rat intestinal villi in which the epithelium was removed by osmic acid maceration method [12]. Subepithelial fibroblasts network is exposed. Photo is courtesy of Dr Terumasa Komuro with copyright permission of Arch Histol Cytol (53 (1990): 1-21). **D:** Light micrograph (Nomarski differential interference contrast image) of subepithelial fibroblasts in primary culture isolated from rat duodenum. The method of culture was described in [13].

Subepithelial fibroblasts form a cellular network just under the epithelium of the gastrointestinal tract (Figure 1B). They have flattened cell bodies with numerous long, attenuated cell processes, are rich in  $\alpha$ -smooth muscle actin ( $\alpha$ -SMA), communicate via gap junctions and their cellular network ensheaths lamina propria of intestinal villi, just like a nylon stocking (Figure 1C) [9, 10, 11, 12]. Subepithelial fibroblasts communicate with epithelium, blood vessels, smooth muscles and neural networks (Figure 1B). We established a primary culture method of subepithelial



fibroblasts isolated from rat duodenal villi (Figure 1D) [13]. Using the cultured cells, we found that subepithelial fibroblasts express many kinds of receptors for vaso- and neuro-active substances, such as endothelins (ETs), substance-P, serotonin (5HT), angiotensin II and ATP, and that they form a syncytium via functional gap junctions [13, 14, 15]. Furthermore, subepithelial fibroblasts change cell morphology drastically and reversibly between flat morphology with broad cell processes (flat-shape) and round cell body with thin cell processes (stellate-shape) depending on intracellular cAMP levels (Figure 2) [13]. The 'Flat-shape' is maintained by a numerous actin fibers in the cell, and the cell possesses contractility. On the other hands, in stellate shaped cells such dense actin fibers are de-polymerized [13].

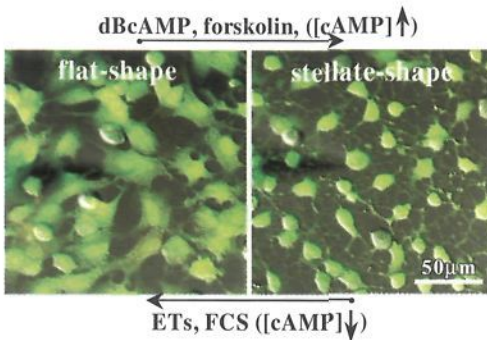


Figure 2. Cell shape changes in subepithelial fibroblasts. Subepithelial fibroblasts change their cell shape between flat morphology with broad cell processes (flat-shape, left image) and round cell body with thin cell processes (stellate-shape, right image) within 10 min depending on intracellular cAMP level. Nomarski images with indo-1 fluorescence.

Recently, we revealed that subepithelial fibroblasts are highly sensitive to mechanical stimulations, such as 'touch' and 'stretch', and release ATP by the stimulations, and that the mechano-sensitivities are cell-shape dependent. From these findings, we have proposed that subepithelial fibroblasts are working as a mechano-sensor in the intestinal villi via ATP releasing [16].

ATP and nucleotides are now recognized as important and ubiquitous extracellular messengers in various kinds of tissues and organs [17, 18]. ATP is often released by mechanical stimulations and activates surrounding cells via many subtypes of P2Y metabotropic and P2X ionotropic ATP receptors [19]. The released ATP works as autocrine and paracrine mediators, and play pivotal roles in the mechano-transduction in many tissues and organs; e. g., in blood vessel, blood flow induces ATP release from endothelial cells and ATP enhances mechano-sensitivity to the share stress [20]; in airway, ciliated epithelial cells release ATP by foreign-substances induced mechanical-stress, and enhance salt and water transport, ciliary beat frequency and mucin secretion to increase defense mechanisms [21, 22]; in mammary alveoli, myo- and secretory epithelial cells interact mutually via mechanically released ATP to enhance milk secretion [23, 24]; in tubular and bladder visceral organs, such as intestine [25] and urinary bladder [26, 27], nociceptive mechano-sensory transduction occurs by ATP released from epithelium by the distension or distortion of these organs.

Here, we review our results and discuss the roles of subepithelial fibroblasts in intestinal functions, especially concerning their mechanical properties.

## 2 Mechanosensitive Network of Subepithelial Fibroblasts

We applied two types of mechanical stimulations to the cultured subepithelial fibroblasts isolated from 10 to 12 day old rat duodenum. One is touching a cell with fine glass rod and another is stretching the cells, which are cultured on an elastic chamber made with silicone elastomer [16]. We measured intracellular  $\text{Ca}^{2+}$  changes with indo-1 fluorescence using an UV-laser scanning confocal microscope and released ATP with luciferin-luciferase bioluminescence using a luminometer or a luminescence imaging system.

### 2.1 Touch induced $\text{Ca}^{2+}$ -waves and ATP release

The touching of a subepithelial fibroblast with a fine glass rod induced an intracellular  $\text{Ca}^{2+}$  increase in the cells and the  $\text{Ca}^{2+}$  increase propagated to surrounding cells (intercellular  $\text{Ca}^{2+}$  waves).  $\text{Ca}^{2+}$  wave propagations were reversibly blocked by MRS2179 (100  $\mu\text{M}$ ), an inhibitor of P2Y1, but not by CBX (100  $\mu\text{M}$ ), a gap junction blocker (Figure 3).  $\text{Ca}^{2+}$  waves propagated to separate cells where no physical contact existed between the cells [16]. These results strongly suggest that touch induced a release of nucleotides from stimulated cells, which activated P2Y1 receptors in surrounding cells.

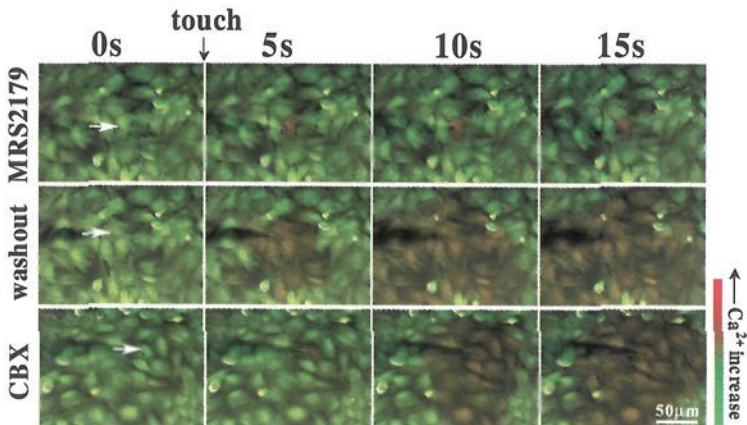


Figure 3. Mechanical stimulation (touch) induces  $\text{Ca}^{2+}$  waves in subepithelial fibroblasts.  $\text{Ca}^{2+}$  waves were suppressed in MRS2179 (100  $\mu\text{M}$ ), a P2Y1 ATP receptor blocker (upper panel), and recovered after the washout (middle).  $\text{Ca}^{2+}$  waves were not affected by CBX (100  $\mu\text{M}$ ), a gap junction blocker (lower).  $\text{Ca}^{2+}$  changes were measured by indo-1 fluorescence using an UV-laser confocal microscope. Two fluorescence images of indo-1 (F405 as red, F480 as green) were superimposed onto Nomarski images.



To confirm the result, we measured the touch induced ATP release using an imaging system of luciferin-luciferase bioluminescence. By touching a cell briefly, intense luminescence occurred and it diffused to the surroundings (Figure 4), indicating ATP is released from the touched cells. For the ATP receptor subtype, histochemical, RT-PCR, western blotting and  $\text{Ca}^{2+}$  response analyses indicated P2Y1 is a dominant functional subtype [16].

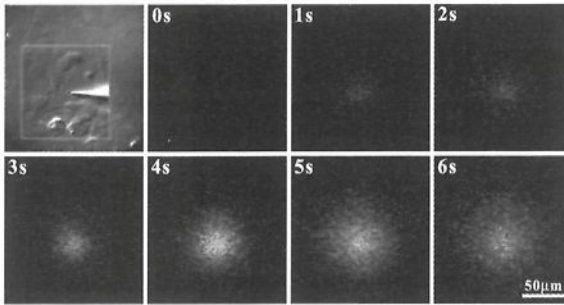


Figure 4. Touch induces ATP release in subepithelial fibroblasts. ATP-release is visualized by luciferin-luciferase bioluminescence using a luminescence imaging system, where the luminescence is amplified using an image intensifier and a high-sensitive cooled CCD camera. Top-left Nomarski image is observed simultaneously with the luminescence using IR illumination.

So, mechanical stimulation (touching) of subepithelial fibroblasts induces ATP release and the released ATP activates P2Y1 on surrounding cells. These processes form propagating intercellular  $\text{Ca}^{2+}$  waves in subepithelial fibroblasts and may work as important messenger in the villi.

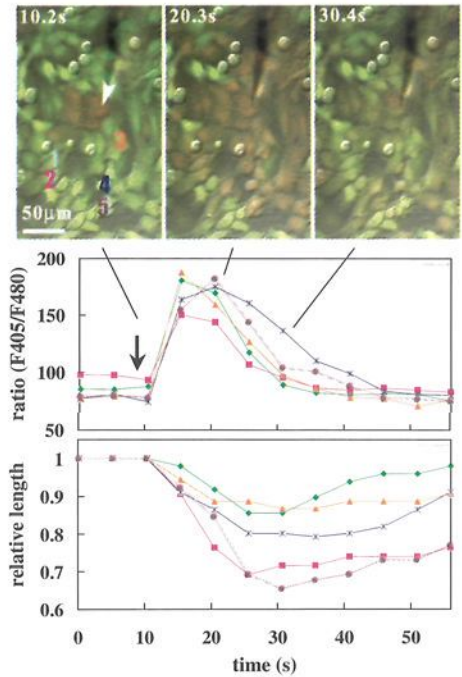


Figure 5. Propagating contractions of subepithelial fibroblasts. Following the touch evoked  $\text{Ca}^{2+}$  waves brief cell contractions were observed. The  $\text{Ca}^{2+}$  change and the contraction in each cell (shown by different colors in upper left figure) were shown in middle and bottom traces, respectively. Cell contractions were measured by the shortening of cell-length. Contractions occur with about 10 s delays after the  $\text{Ca}^{2+}$  change.

## 2.2 Contractile network

When a subepithelial fibroblast was stimulated by touch, concomitantly with  $\text{Ca}^{2+}$  wave propagation, transient cellular contractions were sometimes propagated (Figure 5). Cell contractions reached maximum at about 10 s delay after the peak of  $\text{Ca}^{2+}$  increase. Application of ATP (0.1-100  $\mu\text{M}$ ) and ETs (0.1-10 nM) also induced transient contraction following the  $\text{Ca}^{2+}$  increase. These transient and brief cellular contractions of subepithelial fibroblast networks may affect mechanical properties of villi and may cause the villous motility in a part.

## 2.3 Stretch induced $\text{Ca}^{2+}$ responses and ATP release

Another type of mechanical stimulation, stretching (10-60%, 3 s) of cells cultured on silicone elastomer also induced  $\text{Ca}^{2+}$  increase (Figure 6B, lower panel). The response was transient and disappeared after a few tens of seconds. The number of responsive cells increased dependant on an increase in stretch length [16].

Simultaneously to the  $\text{Ca}^{2+}$  measurement, we measured ATP content in perfusates using luciferin-luciferase bioluminescence and detected clear ATP release by stretch (Figure 7). So, subepithelial fibroblasts respond to stretch and release ATP. This stretch sensitivity may serve in mechanosensing in the intestinal villi.

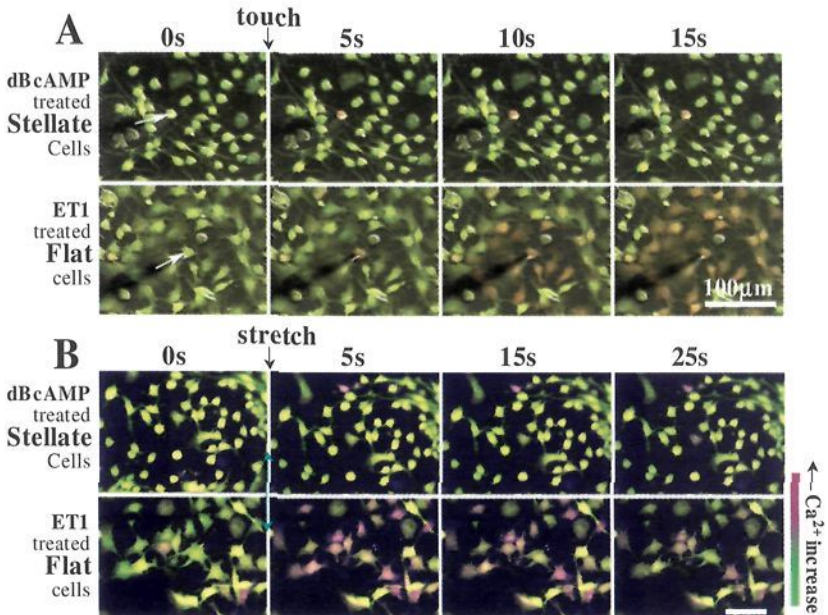


Figure 6. Cell-shape dependent mechanosensitivity. Mechanical stimulations, touch (A) and stretch (B), induced- $\text{Ca}^{2+}$ -responses and -waves in subepithelial fibroblasts were suppressed in dBcAMP treated stellate-shaped cells (upper panels in both A and B) and recovered in ET1-treated flat-shaped cells (lower panels in both A and B).

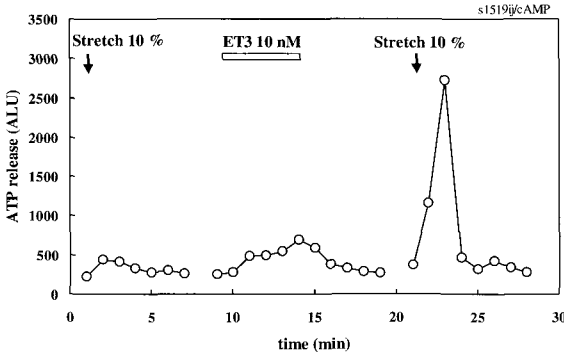


Figure 7. Stretch induced ATP releases were suppressed in dBcAMP-treated stellate-shaped cells and recovered or enhanced further in ET-treated flat shaped cells. ATP contents in perfusate were measured at every minute by luciferin-luciferase bioluminescence using a luminometer.

#### 2.4 Cell shape dependent mechanosensitivity

As shown in above (Figure 2), subepithelial fibroblasts change their cell shape from flat-shape to stellate shape depending on intracellular cAMP level. We found that the mechano-sensitivities were highly cell-shape dependent. Mechanically (touch: Figure 6A and stretch: Figure 6B) induced  $\text{Ca}^{2+}$  signaling was abolished in stellate-shaped cells treated with dBcAMP (Figure 6A upper, 6B upper panels), and recovered in re-flattened cells treated with endothelin (Figure 6A lower, 6B lower panels). The ATP release was suppressed in stellate-shaped cells and recovered or further enhanced in re-flattened cells (Figure 7). The response to ATP also decreased in stellate-shaped cells [16].

These findings indicate that cAMP-mediated intracellular signaling causes cell-shape change, which accompanies the changes in mechano- and ATP sensitivities.

### 3 Roles of Subepithelial Fibroblasts in Intestinal Villi

Subepithelial fibroblasts secrete extracellular matrices and form basal lamina under the epithelium. It is now being recognized that subepithelial fibroblasts play major roles in the regulation of proliferation, migration, transepithelial resistance and secretory responses of epithelial cells, and in the regulation of inflammatory and injury responses in the gut [28, 29]. From the unique mechanical properties of subepithelial fibroblasts we found, some additional physiological functions are considered.

#### 3.1 Barrier/Sieve functions

Under basal lamella, dense collagenous fibrils and subepithelial fibroblasts networks form subepithelial reticular sheets [12, 30]. Basal lamina and subepithelial reticular sheets work together as a sieve for various substances and immune cells. In addition to their direct sieve function, they may control the permeability of epithelium to ions, nutrients and water by releasing various cytokines, such as TGF- $\beta$ , TNF- $\alpha$ , HGF,

PGEs. These cytokines are secreted from subepithelial fibroblasts [31] and modify the assembly of tight junctions of epithelium to change their permeability [32, 33]. So, the subepithelial fibroblast network may work as a barrier or sieve by itself and by controlling the epithelium in the intestinal villi (Figure 8A). Subepithelial fibroblasts change their shape quickly and dramatically by ETs applications depending on intracellular cAMP levels, suggesting that the barrier or sieve properties are controlled locally and dynamically in the villi.

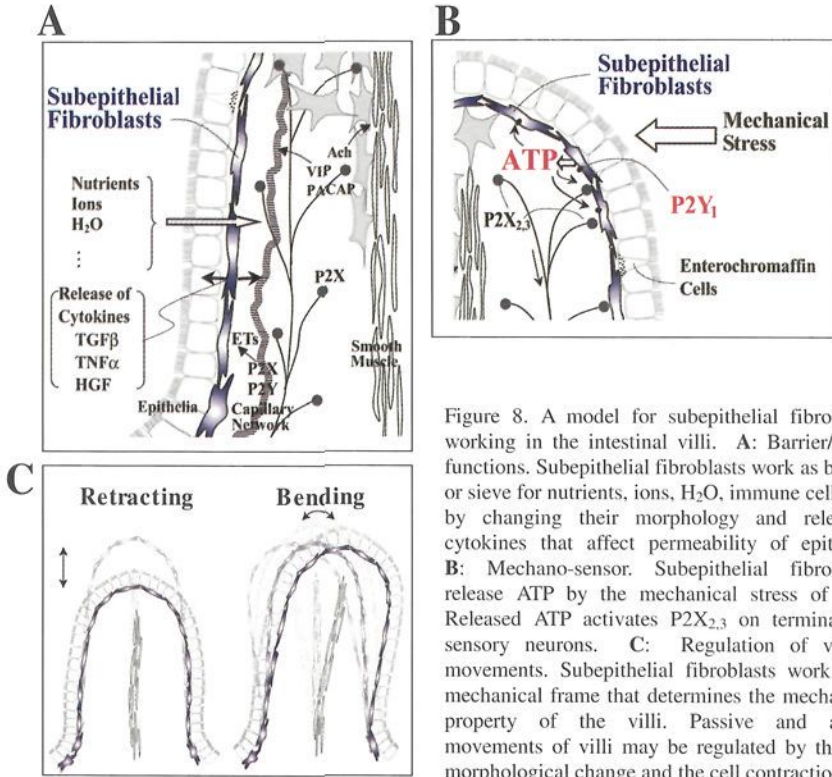


Figure 8. A model for subepithelial fibroblasts working in the intestinal villi. **A:** Barrier/Sieve functions. Subepithelial fibroblasts work as barrier or sieve for nutrients, ions, H<sub>2</sub>O, immune cells etc. by changing their morphology and releasing cytokines that affect permeability of epithelia. **B:** Mechano-sensor. Subepithelial fibroblasts release ATP by the mechanical stress of villi. Released ATP activates P2X<sub>2,3</sub> on terminals in sensory neurons. **C:** Regulation of villous movements. Subepithelial fibroblasts work as a mechanical frame that determines the mechanical property of the villi. Passive and active movements of villi may be regulated by the cell morphological change and the cell contraction.

### 3.2 Mechanosensor in the intestinal villi

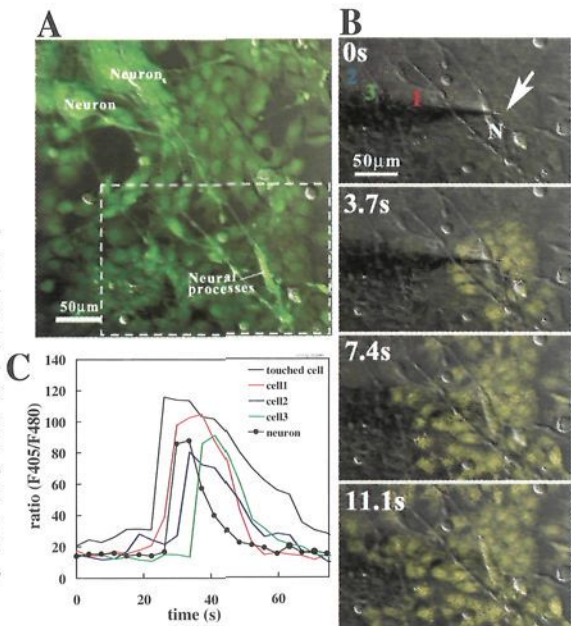
Food and water intake give rise to mechanical signals that induce the villous motility and the peristaltic movement in the gut, meaning that the intestine is a mechanosensing organ. There seems to be several mechanosensors located in mucosa, submucosa and muscle layer including myenteric plexus. In the mucosa, it was suggested that luminal stimuli release sensory mediators from mucosal epithelium, which then activate nerve terminals of sensory neurons [2, 34, 35]. Cholecystokinin and serotonin are reported to be chemo-mediators that excite nerve



terminals in mucosal sensory neurons, and are released by luminal stimuli [36, 37]. ATP is also reported to activate nerve terminals of intrinsic sensory neurons via P2X2 and/or P2X3 [3, 38, 39, 40]. In P2X2 or P2X3 gene deleted mice, the intraluminal pressure-induced peristalsis was inhibited [39, 40]. The source of ATP in mucosa is thought to be released from enterochromaffin and from epithelial cells by mechanical stress of the intestine [34, 35]. However, there is a considerable distance from epithelial to neuronal termini. Between them, there exist basal lamina and also a network of subepithelial fibroblasts that are sensitive to serotonin and ATP [14]. Furthermore, subepithelial fibroblasts are sensitive to mechanical stress and release ATP as shown herein. From their location and from their displayed characteristics, subepithelial fibroblasts are thought to plausibly be the mechanosensor in the intestinal villi (Figure 8). Actually, nerve terminals are located near subepithelial fibroblasts in the villi [9, 10].

To confirm the idea, we co-cultured neural cells (NG108-15 cells) on subepithelial fibroblasts (Figure 9).  $\text{Ca}^{2+}$  waves induced mechanically in subepithelial fibroblasts propagated to and activated the neuron (Figure 9). So, we propose that subepithelial fibroblasts release ATP upon stretch or distension of villi and that the ATP acts on P2X2 and/or P2X3 receptors on intrinsic sensory enteric neurons to regulate peristalsis and on extrinsic sensory neurons originating in dorsal root ganglion to induce nociception. In urinary bladder, similar mechanism is working for nociception of bladder fullness, although the mechanosensing or ATP releasing cells are thought to be epithelial cells [26, 27].

Figure 9. Propagation of  $\text{Ca}^{2+}$  signal from subepithelial fibroblasts to the neuron. **A:** Co-culture of differentiated NG108-15 neural cells and subepithelial fibroblasts. Neurons with well-developed processes are seen on subepithelial fibroblasts. **B:** Touching of subepithelial fibroblasts evoked  $\text{Ca}^{2+}$  waves (yellow parts). The  $\text{Ca}^{2+}$  signal spread to the neural processes (N). **C:** Traces show  $\text{Ca}^{2+}$  increase in several subepithelial fibroblasts and the neuron.



### 3.3 Regulation of mechanical properties and movements of the villi

Subepithelial fibroblasts are rich in  $\alpha$ -smooth muscle actin and their cellular networks ensheath the lamina propria of intestinal villi as a contractile network. So, they may work as a mechanical frame to keep the flexible structure and contractility of the villi (Figure 8C). We think the structure and mechanical properties of villi are kept by not only smooth muscle in lamina propria but also subepithelial fibroblast networks. Further, this mechanical frame is not static and the properties may be regulated by the morphological changes of subepithelial fibroblasts.

We showed that subepithelial fibroblasts made transient (10-20 s) contractions synchronizing to  $\text{Ca}^{2+}$  wave propagations (Figure 5). The contractions were due to the released ATP. Application of ETs also induced brief but oscillatory contraction in subepithelial fibroblasts. The intestinal villi are known to move spontaneously with retraction-extension and bending modes (Figure 8C) [8]. Contractility of subepithelial fibroblast networks may regulate such villous motility [9].

The roles of intestinal villi are not only to expand the area of absorption but also to transport smoothly and slowly the contents (chyme), which are the mixture of solid and fluid. So, mechanical properties of intestinal villi must be flexible and regulated dynamically. These extra-ordinary mechanical properties may be achieved by dynamical networks of subepithelial fibroblasts.

## 4 Summary

Subepithelial fibroblast networks form a syncytium under the epithelium in the villi, respond to many kinds of baso- and neuro- active substances, and change shape rapidly or contract transiently. They are also highly sensitive to mechanical stress and release ATP. Subepithelial fibroblast networks are not only connected with lamina propria fibroblast-like cells, but also closely contact the capillary network, sensory and motor neuronal networks, smooth muscles, and epithelium in the villi. Subepithelial fibroblasts communicate among these cell systems via ATP release and other humoral factors. From these views, we consider that subepithelial fibroblasts work as (1) barrier/sieve, (2) mechano-sensor and (3) mechanical frame in the villi. These functions are likely regulated locally and dynamically in the villi by rapid cell-shape changes and contraction, and cell-shape dependent mechano-sensitivities, which may play crucial roles in intestinal functions.

## Acknowledgments

This work was supported in part by Grants-in Aid for Scientific Research 13480216, Scientific Research on Priority Areas 15086270, and Creative Scientific Research

16GS0308 from the Ministry of Education, Culture, Sports, Science and Technology of Japan, and a grant from Japan Space Forum to MS.

## References

1. Furness, J. B., Wolfgang, A. A., Kunze, A., Clerc, N., 1999. Nutrient tasting and signaling mechanisms in the gut. II. The intestine as a sensory organ: neural, endocrine, and immune responses. *Am. J. Physiol.* 277, G922-G928.
2. Buchan, A. M., 1999. Nutrient tasting and signaling mechanisms in the gut. III. Endocrine cell recognition of luminal nutrients. *Am. J. Physiol.* 277, G1103-G1107.
3. Furness, J. B., Jones, C., Nurgali, K., Clerc, N., 2004. Intrinsic primary afferent neurons and nerve circuits within the intestine. *Prog. Neurobiol.* 72, 143-164.
4. Tsuji, S., Anglade, P., Ozaki, T., Sazi, T., Yokoyama, S., 1992. Peristaltic movement evoked in intestinal tube devoid of mucosa submucosa. *Jpn. J. Physiol.* 42, 363-375.
5. Hambleton, B. F., 1914. Note upon the movements of the intestinal villi. *Am. J. Physiol.* 34, 446-447.
6. Lee, J., 1971. Contraction of villi and fluid transport in dog jejunal mucosa in vitro. *Am J Physiol* 221, 488-495.
7. Womack, W. A., Barrowman, J. A., Graham, W. H., Benoit, J. N., Kvietyts, P. R., Granger, D. N., 1987. Quantitative assessment of villous motility. *Am. J. Physiol.* 252, G250-6.
8. Womak, W. A., Kvietyts, P. R., Granger D. N., 1989. Villous motility. In: *Handbook of Physiology. The Gastrointestinal System. Motility and Circulation.* sect. 6, vol. I, pt. 2, pp. 975-986. Bethesda: Am. Physiol. Soc.
9. Güldner, F. H., Wolff, J. R., Keyserlingk, D. G., 1972. Fibroblasts as a part of the contractile system in duodenal villi of rat. *Z. Zellforsch. Mikrosk. Anat.* 135, 349-360.
10. Desaki, J., Fujiwara, T., Komuro, T., 1984. A cellular reticulum of fibroblast-like cells in the rat intestine: scanning and transmission electron microscopy. *Arch. Histol. Jpn.* 47, 179-186.
11. Joyce, N. C., Haire, M. F., Palade, G. E., 1987. Morphological and biochemical evidence for a contractile cell network within the rat intestinal mucosa. *Gastroenterol.* 92, 68-81.
12. Komuro, T., Hashimoto, Y., 1990. Three-dimensional structure of the rat intestinal wall (mucosa and submucosa). *Arch. Histol. Cytol.* 53, 1-21.
13. Furuya, S., Furuya, K., 1993. Characteristics of cultured subepithelial fibroblasts of rat duodenal villi. *Anat. Embryol.* 187, 529-538.
14. Furuya, K., Furuya, S., Yamagishi, S., 1994. Intracellular calcium responses and shape conversions induced by endothelin in cultured subepithelial fibroblasts of rat duodenal villi. *Pflügers Arch.* 428, 97-104.

15. Furuya, S., Furuya, K., Sokabe, M., Hiroe, T., Ozaki, T., 2005. Characteristics of cultured subepithelial fibroblasts in the rat small intestine; II: Localization and functional analysis of endothelin receptors and cell-shape independent gap junction permeability. *Cell Tissue Res.* 319, 103-119.
16. Furuya, K., Sokabe, M., Furuya, S., 2005. Characteristics of subepithelial fibroblasts as a mechano-sensor in the intestine: cell-shape-dependent ATP release and P2Y1 signaling. *J. Cell Sci.* 118, 3289-3304.
17. Abbracchio, M. P., Williams, M., 2001. Purinergic and pyrimidinergic signalling I, II Handbook of experimental pharmacology 151/I,II. Berlin: Springer-Verlag.
18. Burnstock, G., Knight, G. E., 2004. Cellular distribution and functions of P2 receptor subtypes in different systems. *Int. Rev. Cytol.* 240, 31-304.
19. Schwiebert, E. M., 2000. Extracellular ATP-mediated propagation of  $Ca^{2+}$  waves. Focus on "Mechanical strain-induced  $Ca^{2+}$  waves are propagated via ATP release and purinergic receptor activation" *Am. J. Physiol.* 279, C281-C283.
20. Yamamoto, K., Korenaga, R., Kamiya, A., Ando, J., 2000. P2X(4) receptors mediate ATP-induced calcium influx in human vascular endothelial cells. *Am. J. Physiol.* 279, H285-292.
21. Hansen, M., Boitano, S., Dirksen, E. R., Sanderson, M. J., 1993. Intercellular calcium signaling induced by extracellular adenosine 5'-triphosphate and mechanical stimulation in airway epithelial cells. *J. Cell Sci.* 106, 995-1004.
22. Homolya, L., Steinberg, T. H., Boucher, R. C., 2000. Cell to cell communication in response to mechanical stress via bilateral release of ATP and UTP in polarized epithelia. *J. Cell Biol.* 150, 1349-60.
23. Furuya, K., Nakano, H., Enomoto, K., 1997. Cause and roles of mechanical stress in mammary gland. In *Cell Volume Regulation*, (ed. Okada Y.). pp. 85-91. Amsterdam: Elsevier.
24. Nakano, H., Furuya, K., Yamagishi, S., 2001. Synergistic effects of ATP on oxytocin-induced intracellular  $Ca^{2+}$  response in mouse mammary myoepithelial cells. *Pflügers Arch.* 442, 57-63.
25. Burnstock, G., 2001b. Purinergic signalling in gut. In *Purinergic and pyrimidinergic signalling II. Cardiovascular, respiratory, immune, metabolic and gastrointestinal tract function.* (ed. Abbracchio, M. P. and Williams, M.) Handbook of experimental pharmacology 151/II. pp. 141-204. Berlin: Springer-Verlag.
26. Cockayne, D. A., Hamilton, S. G., Zhu, Q. M., Dunn, P. M., Zhong, Y., Novakovic, S., Malmberg, A. B., Cain, G., Berson, A., Kassotakis, L., et al., 2000. Urinary bladder hyporeflexia and reduced pain-related behavior in P2X3-deficient mice. *Nature* 407, 1011-1015.
27. Vlaskovska, M., Kasakov, L., Rong, W., Bodin, P., Bardini, M., Cockayne, D. A., Ford, A. P., Burnstock, G., 2001. P2X3 knock-out mice reveal a major sensory role for urothelially released ATP. *J. Neurosci.* 21, 5670-5677.



28. Powell, D. W., Mifflin, R. C., Valentich, J. D., Crowe, S. E., Saada, J. I., West, A. B., 1999a. Myofibroblasts. I. Paracrine cells important in health and disease. *Am. J. Physiol.* 277, C1-C9.
29. Powell, D. W., Mifflin, R. C., Valentich, J. D., Crowe, S. E., Saada, J. I., West, A. B., 1999b. Myofibroblasts. II. Intestinal subepithelial fibroblasts. *Am. J. Physiol.* 277, C183-C201.
30. Komuro, T., 1985. Fenestrations of the basal lamina of intestinal villi of the rat. Scanning and transmission electron microscopy. *Cell Tissue Res.* 239, 183-188.
31. Valentich, J. D., Popov, V., Saada, J. I., Powell, D. W., 1997. Phenotypic characterization of an intestinal subepithelial myofibroblast cell line. *Am. J. Physiol.* 272, C1513-C1524.
32. Beltinger, J., McKaig, B. C., Makh, S., Stack, W. A., Hawkey, J., Mahida, Y. R., 1999. Human colonic subepithelial myofibroblasts modulate transepithelial resistance and secretory response. *Am. J. Physiol.* 277, C271-C279.
33. Walsh, S. V., Hopkins, A. M., Nusrat, A., 2000. Modulation of tight junction structure and function by cytokines. *Adv. Drug Deliv. Rev.* 41, 303-313.
34. Burnstock, G., 2001a. Purine-mediated signalling in pain and visceral perception. *Trends Pharmacol. Sci.* 22, 182-188.
35. Cooke, H. J., Wunderlich, J., Christofi, F. L., 2003. "The force be with you"; ATP in gut mechanosensory transduction. *News Physiol. Sci.* 18, 43-49.
36. Wade, P. R., Chen, J., Jaffe, B., Kassem, I. S., Blakely, R. D., Gershon, M. D., 1996. Localization and function of a 5-HT transporter in crypt epithelia of the gastrointestinal tract. *J. Neurosci.* 16, 2352-2364.
37. Eastwood, C., Maubach, K., Grundy, K. D., 1998. The role of endogenous cholecystokinin in the sensory transduction of luminal nutrient signals in the rat jejunum. *Neurosci. Lett.* 254, 145-148.
38. Bertrand, P. P., Bornstein, J. C., 2002. ATP as a putative sensory mediator: activation of intrinsic sensory neurons of the myenteric plexus via P2X receptors. *J. Neurosci.* 22, 4767-4775.
39. Bian, X., Ren, J., DeVries, M., Schnegelsberg, B., Cockayne, D. A., Ford, A. P., Galligan, J. J., 2003. Peristalsis is impaired in the small intestine of mice lacking the P2X3 subunit. *J. Physiol.* 551, 309-322.
40. Ren, J., Bian, X., DeVries, M., Schnegelsberg, B., Cockayne, D. A., Ford, A. P., Galligan, J. J., 2003. P2X2 subunits contribute to fast synaptic excitation in myenteric neurons of the mouse small intestine. *J. Physiol.* 552, 809-21.

### **III. TISSUE ENGINEERING**

This page is intentionally left blank

# MICROELEMENTS FOR CARTILAGE TISSUE ENGINEERING

K. TSUCHIYA, K. S. FURUKAWA AND T. USHIDA

*Center for Disease Biology and Integrative Medicine, Graduate School of Medicine,  
The University of Tokyo, 7-3-1 Hongo, Tokyo 113-0033, Japan  
E-mail: ushida@m.u-tokyo.ac.jp*

*Biomedical Engineering Laboratory, Graduate School of Engineering,  
The University of Tokyo, 7-3-1 Hongo, Tokyo 113-8656, Japan*

Progress in both cell biology and biomaterial technology has led to the possibility of therapeutic applications of tissue engineering for the repair of cartilage defects. The regulation of cell differentiation and the cell source have been a big challenge for this tissue engineering approach. The re-aggregate approach is an attempt to achieve a more or less complete regeneration of tissues from dispersed cells of a particular origin, under controlled culture conditions. Mesenchymal stem cells (MSCs) are expected to be a useful cell source for cartilage tissue engineering. In order to explore the feasibility of applying these cells, MSC aggregates mixed with chondrocytes were examined. For regulating cell differentiation and forming micro-tissue element of cartilage, rotational culture system was innovated. Rapid and large-scale “microelements of cartilage” were formed in this system.

## 1 Introduction

Chondrocytes in articular cartilage synthesize collagen type II and large sulfated proteoglycans, whereas the same cells cultured in monolayer (2D) dedifferentiate into fibroblastic cells and express collagen type I and small proteoglycans [1]. Cell-cell interaction realized in cell aggregation is thought to play a pivotal role in cell differentiation. Pellet culture system or 3D culture system was developed as a method for preventing the phenotypic modulation of chondrocyte, and promoting the redifferentiation of dedifferentiated one [2, 3]. It is difficult to obtain the required mass of autologous chondrocytes because of the limited availability of donor tissue and donor site morbidity. Mesenchymal stem cells (MSCs) are expected to be a useful cell source for cartilage tissue engineering [4-7]. Chondrogenesis can be induced by culturing MSCs in condensed pellets in defined media *in vitro* [4, 5]. However MSCs can hardly differentiate into chondrocytes after repeated passages. Some strong inductive signals for chondrogenesis are required to differentiate the passage cultured MSCs into chondrocytes. Co-culture of MSCs with mature chondrocytes in one pellet is a strategy that both provides inductive signals and solves the cell source problem.

Because the pellet culture system forms only one cell-aggregate each tube by a centrifugator, the pellet could not be applied to produce a tissue-engineered cartilage and this is a critical issue for cartilage tissue engineering. Previously we reported a

rotational culture system to fibroblast aggregates for skin tissue engineering [8]. In this report, we analyzed the effects of co-cultured MSCs with mature chondrocytes in mixed pellet culture *in vitro* and we showed an effectiveness of a rotational culture for forming a large number of chondrocyte-aggregates at once.

## 2 Methods

### 2.1 Co-culture of MSC with mature chondrocytes

Bovine articular chondrocytes (BCH) were isolated from the shoulder articular cartilage of a four-week old calf. The isolated chondrocytes were cultured for one week and two-passaged BCH were used for assay. Human mesenchymal stem cells (MSCs) were purchased from Poietics, Inc. in the second passage. Thawed cells were cultured with defined growth used for pellet culture after another passage. BCH and MSC were harvested and suspended in chondrogenic medium with TGF- $\beta$  for induction of chondrogenesis. The cell suspensions of MSCs and chondrocytes were mixed at 5 ratios as shown in Table 1. The cells were spun down in polypropylene conical tubes after mixture and maintained with medium changes three times per week. Free-floating pellets were formed within the first 24 h of culture. After 4 weeks post-inoculation in tubes, the pellets were analyzed histologically. The chondrogenic phenotype was evaluated with safranin-O staining.

Cell ratio	MSC	BCH
M	$2.5 \times 10^5$	—
1:2	$2.0 \times 10^5$	$4.0 \times 10^5$
1:1	$2.0 \times 10^5$	$2.0 \times 10^5$
2:1	$2.0 \times 10^5$	$1.0 \times 10^5$
B	—	$1.0 \times 10^6$ (cells)

Table 1. Mixture ratio of mesenchymal stem cell and articular chondrocyte. M, MSC alone; 1:2, 1 volume of MSC to 2 volumes of BCH; 1:1, equal volume of each kind of cells; 2:1, 2 volumes of MSC to 1 volume of BCH; B, BCH alone.[9]

### 2.2 RNA preparation and semi-quantitative RT-PCR of co-culture pellets

Total RNA was prepared from the pellets after 1, 2, 3 and 4 weeks culture. RNA for RT-PCR was converted to cDNA. Semi-quantitative PCR amplification was carried out and gene expression of type I collagen, type II collagen, 18S ribosomal RNA, human  $\beta$ 2 microglobulin and human type II collagen primers were analyzed [9]. Human  $\beta$ 2 microglobulin and type II collagen primers were designed to be human specific, while other primers react to bovine and human equally. The reaction products were resolved by electrophoresis and the blot areas were measured using NIH image software. The ratios of human specific  $\beta$ 2 microglobulin to 18S and type II collagen to type I collagen were calculated.

### 2.3 Rotational culture of chondrocytes

Four-passaged bovine articular chondrocytes were accomplished with our new method by an orbital shaker. Single prepared cells were finally resuspended at  $0.3 \times 10^7$  cells/ml with the chondrogenic medium with or without TGF- $\beta$  for a rotational culture. Five milliliter of the suspension was conducted into a dish (diameter; 35 mm, Costar, NY, USA) fabricated for non-adhesive cell culture. The shaking speed was set at 80 rpm, so that cells could be distributed at the center of the dish [10]. The dishes were placed in a humidified CO<sub>2</sub> incubator. Chondrocyte-aggregates were harvested and measured their diameters.

## 3 Results

### 3.1 Gross Appearance and histological findings of co-cultured pellets

Pellets of the mixed cells were formed and floated in the culture medium within 24 hours (Fig. 1). All pellets showed spherical or oval shapes in the first few days after their formation. The pellets formed from chondrocytes alone and MSC/BCH (mixed pellet) gradually grew bigger and their surfaces became smooth and glossy. The 2:1 pellets gained over twice the size (Fig. 2). The mixed pellets showed a stronger and more homogenous staining as the cell ratio of MSC to BCH increased from 1:2 to 2:1 (Fig. 3). The mixed pellet of 2:1 showed the highest growth, strongest safranin O staining and most homogenous distribution of cartilaginous extracellular matrices (Fig. 4).

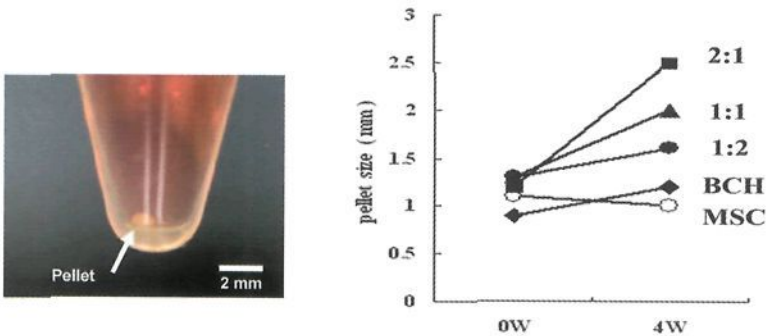


Figure 1 (Left). A Pellet in a 15 ml polypropylene conical tube. Cells aggregated within a day after centrifugation. By tapping, the pellets were detached from the wall of tube and maintained their shape during the culture period.[9]

Figure 2 (Right). Pellet sizes after 1 day and 4 weeks culture. BCH and mixed pellets increased their size while MSC pellets slightly decreased in size. [9]

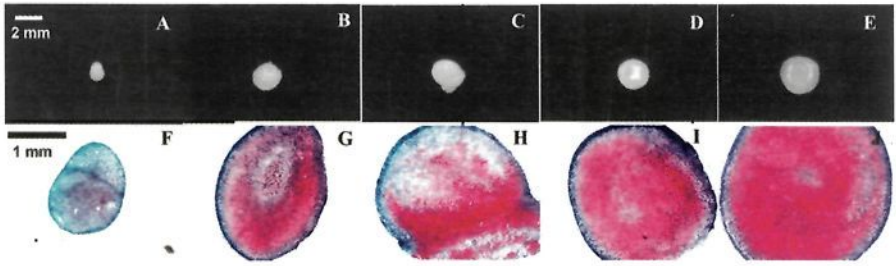


Figure 3. Gross appearance of pellets (A-E) and histological staining with Safranin-O (F-J) after 4 weeks culture. A and F are MSC pellet, B and G are 1:2, C and H are 1:1, D and I are 2:1, E and J are BCH pellets. [9]

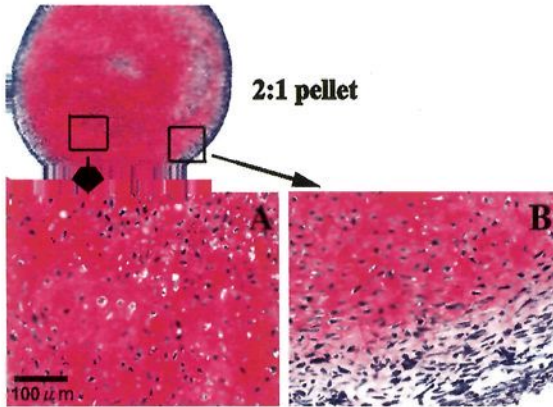


Figure 4. Histological staining with safranin-O of 2:1 pellet at a magnification. Cells in the central part showed a round shape and abundant cartilaginous extracellular matrix while peripheral cells negatively stained and was fibroblast-like. [9]

### 3.2 Cell proportion during co-culture

Human MSC and total cell number were detected by an internal standard by RT-PCR using a  $\beta_2$  microglobulin primer designed specifically for human, and an 18S ribosomal RNA primer designed for a consensus sequence of human and bovine, respectively. The ratio of the two internal standards of mixed pellets was calculated on the basis of MSC only pellets. At the early stage,  $\beta_2$  microglobulin contents in mixed pellets approximately equaled the initial mix ratio. The cell proportion had no significant change during the 4 weeks culture (Fig. 5A), which indicates that the proliferations of both kinds of cells were almost the same.

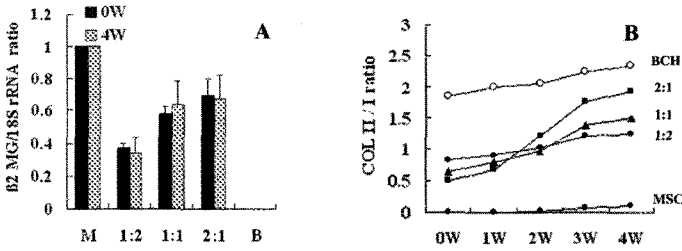


Figure 5. (A) Variation of cell proportion in the pellets during co-culture. The ratio of human specific  $\beta_2$  microglobulin to total 18S rRNA correlates to the proportion of human cells in the pellets. (B) Time course of the ratio of expression of gene encoding type II collagen to that of type I collagen. [9]

### 3.3 Chondrogenic gene expression in MSC pellet and mixed pellets

MSC rarely expressed the gene encoding type II collagen during the first 2 weeks and expressed it slightly after 4 weeks culture, which was contrary to our expectations. Chondrocyte phenotype was evaluated by the ratio of type II collagen to type I collagen gene expression. The ratio of type II collagen to type I collagen gene expression decreased with the increase in percentage of MSC in the pellets. After 4 weeks culture, higher MSC ratio in the mixed pellets showed a higher gene expression ratio of type II to type I collagen (Fig. 5B). A higher content of MSC in the mixed pellets facilitated type II collagen gene expression. Human specific type II collagen gene expression was examined to clarify the origin of the collagen expressed in the mixed pellets. After 4 weeks culture, almost no expression of hCOL II mRNA in either MSC or mixed pellets was detected, while human specific  $\beta_2$  MG mRNA was evident (Figure 6).

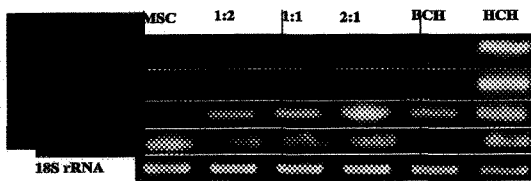


Figure 6. RT-PCR analysis of total RNA isolated from each pellet. Human articular chondrocytes were used for positive controls. Mixed pellets increased in total type II collagen expression after 4 weeks, however human specific type II collagen gene expression level was very low. [9]

### 3.4 Aggregate formation of chondrocytes in rotational culture

The shaking speed was set at 80 rpm, so the cells would be distributed in the center of the dish to augment the frequency of cell-cell contact. Bovine articular chondrocytes started aggregating in few hours and the surfaces of aggregates were irregular, not smooth at initial stage. The diameter of aggregates increased with time and gradually the surfaces became smooth. In 24-36 hours of rotational culture,



aggregates with smooth surface were formed under the condition as shown in Fig. 7. The medium with TGF- $\beta$  made the diameter increase than medium without TGF- $\beta$  (Fig. 7). The diameters of the aggregates distributed in the range from approximately 200  $\mu\text{m}$  to 600  $\mu\text{m}$  (Fig. 8). The results showed that parameters such as culture time and addition of TGF- $\beta$  controlled the diameter.

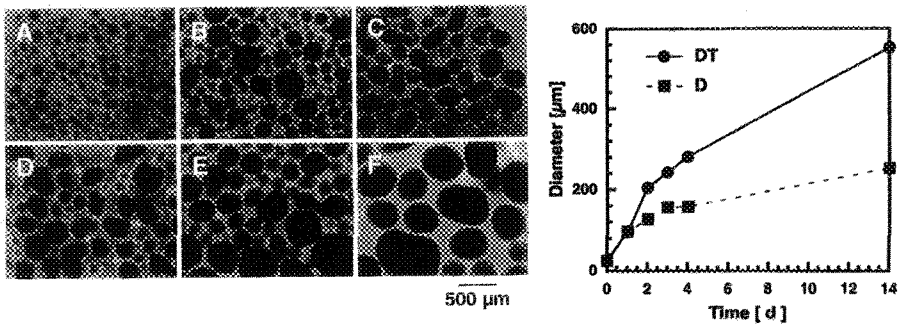


Figure 7 (Left). Effect of incubation time on aggregate formation. [10] (A, D) 2 days, (B, E) 7 days, (C, F) 14 days. (A, B, C) Without TGF- $\beta$ , (D, E, F) with TGF- $\beta$ . Bar= 500  $\mu\text{m}$

Figure 8 (Right). Time course change in diameter of chondrocyte-aggregates. [10] D: Without TGF- $\beta$ , DT: with TGF- $\beta$

## 4 Discussion

### 4.1 Cell source for cartilage tissue engineering

Tissue engineering protocols usually require handling of isolated autologous cells. So far, most approaches to tissue repair by autologous cells use biopsies from healthy sites on contra lateral tissues such as joint cartilage for articular cartilage repair. The shortfalls of these protocols are obvious: the small number of available cells, the morbidity at the donor site and the limited ability of the harvested cells to proliferate and undergo differentiation. Meanwhile, research is increasingly focused on tissue regeneration by relevant precursor or multipotent stem cells [5]. Mesenchymal stem cells isolated from bone marrow are pluripotent cells capable of differentiating into many cell types and may be suitable for autologous articular cartilage repair [6].

### 4.2 Cell-cell interaction is necessary for cell differentiation

Intercellular communication confers on tissues the ability to coordinate several cellular functions, such as the regulation of cell metabolism. Cell-to-cell communication between the same cells in a tissue via gap junctions can also couple

different cell types [11] owing to the molecular compatibility of the connexins expressed [12]. In hepatocytes both gap junctions and paracrine stimulation can support cell-to-cell signaling, suggesting that the two mechanisms might co-operate in controlling tissue homeostasis and in co-coordinating cell responses against changes in the extracellular environment. Homologous and heterologous intercellular communication is critically involved in the development of cartilage during differentiation. In normal cartilage tissue, chondrocytes lose their cell-to-cell communication owing to their rich extracellular matrix. Chondrocytes extracted from cartilage tissue, however, retain the ability to form functional gap junctions in culture [13].

#### 4.3 MSCs affect to up-regulation of the cartilagenous phenotype

There is a possibility that isolated chondrocytes give or receive signals to or from MSCs. If there are agreeable effects on each cell type following mixing of the MSCs with mature chondrocytes, a co-culture system has the potential to be a useful approach to cartilage tissue engineering. In this study we mixed xenogenic cells to clarify the origin of cartilaginous matrix products. It was verified that human and bovine cells coexisted and maintained their initial mixture ratio during the 4 weeks culture. Therefore the changes of cartilage phenotype were not from the change of cell property in the pellets. MSC pellets did not show any positive signals for neocartilage formation. We could not deny the possibility that the passaged MSCs might have lost their chondrogenic capacity during cell proliferation. Despite the low potential of MSCs to differentiate in the present study, the mixed pellets showed up-regulated cartilaginous phenotype as the MSC ratio increased in the mixture. The effects might be derived from the differentiation of MSC and BCH. RT-PCR for the gene encoding human type II collagen did not detect its expression in any pellets, which indicates that MSC did not directly contribute to the up-regulation of cartilaginous matrix production. The increase of type II collagen gene expression and cartilaginous matrix production can be accounted for by the up-regulation of the cartilaginous phenotype of BCH. Redifferentiation of dedifferentiated chondrocytes requires a three-dimensional environment and growth factors to enhance its efficiency. These growth factors are secreted constantly from monolayer cultured MSC or start to secrete in abundance during chondrogenesis. One possible mechanism of co-culture may be that some growth factors secreted from MSC mediate a paracrine effect on BCH and up-regulate their cartilaginous phenotype. Moreover cell-to-cell interactions may be concerned with this effect because additional culture media or trans-well culture did not affect the chondrogenesis of cells in this study (data not shown). Co-culture of MSC and BCH increased the growth of BCH and up-regulated the chondral phenotype of BCH. The co-culture strategy will be useful for *in vitro* expansion of mature chondrocytes without decreasing their differentiation ability.

#### 4.4 Rotational culture system for cartilage tissue elements

For tissue engineering application, we introduced a rotational culture system to achieve a large volume of functional cartilage. In our method, a large number of chondrocyte-aggregates could be formed at once [10]. If the aggregates are inoculated to 3 dimensional scaffolds, the aggregates will outgrow in the scaffolds with keeping the differentiated phenotype, and secretion of matrices. For tissue-engineered cartilage, various kinds of scaffolds (non-woven fiber scaffolds, sponge like scaffolds *etc.*) have been developed thus far. Pore sizes of the scaffolds for tissue-engineered cartilage widely distribute in the range from several  $\mu\text{m}$  to mm [14]. In our experiment, the size of the aggregate could be controlled with some parameters, such as incubation time, and addition of growth factors, *i.e.* TGF- $\beta$ . Therefore, easy inoculation of chondrocyte-aggregates to scaffolds would be realized, adjusting the diameter to pore size of the scaffold. The aggregates formed by our rotational culture method would be widely applied to tissue-engineered products. It is thought that there is possibility to use the aggregates as seeds of differentiated cartilage and act as “microelements of cartilage for tissue engineering”.

#### Acknowledgments

This work was supported by Grant-in-Aid for Scientific Research on Priority Areas 15086205 from the Ministry of Education, Culture, Sports, Science and Technology of Japan.

#### References

1. Schnabel, M., Marlovits, S., Eckhoff, G., Fichtel, I., Gotzen, L., Vecsei, V., Schlegel, J., 2002. Dedifferentiation-associated changes in morphology and gene expression in primary human articular chondrocytes in cell culture. *Osteoarthritis Cartilage* 10, 62-70.
2. Benya, P.D., Shaffer, J.D., 1982. Dedifferentiated chondrocytes reexpress the differentiated collagen phenotype when cultured in agarose gels. *Cell* 30, 215-224.
3. Chen, G., Sato, T., Ushida, T., Hirochika, R., Tateishi, T., 2003. Redifferentiation of dedifferentiated bovine chondrocytes when cultured in vitro in a PLGA-collagen hybrid mesh. *FEBS Lett.* 542, 95-99.
4. Johnstone, B., Hering, T.M., Caplan, A.I., Goldberg, V.M., Yoo, J.U., 1998. In vitro chondrogenesis of bone marrow-derived mesenchymal progenitor cells. *Exp. Cell. Res.* 238, 265-272.
5. Pittenger, M.F., Mackay, A.M., Beck, S.C., Jaiswal, R.K., Douglas, R., Mosca, J.D., Moorman, M.A., Simonetti, D.W., Craig, S., Marshak, D.R., 1999.

- Multilineage potential of adult human mesenchymal stem cells. *Science* 284, 143-147.
6. Yoo, J.U., Barthel, T.S., Nishimura, K., Solchaga, L., Caplan, A.I., Goldberg, V.M., Johnstone, B., 1998. The chondrogenic potential of human bone-marrow-derived mesenchymal progenitor cells. *J. Bone Joint Surg. Am.* 80, 1745-1757.
  7. Wakitani, S., Goto, T., Pineda, S.J., Young, R.G., Mansour, J.M., Caplan, A.I., Goldberg, V.M., 1994. Mesenchymal cell-based repair of large, full-thickness defects of articular cartilage. *J. Bone Joint Surg. Am.* 76, 579-592.
  8. Furukawa, K.S., Ushida, T., Sakai, Y., Suzuki, M., Tanaka, J., Tateishi, T., 2001. Formation of human fibroblast aggregates (spheroids) by rotational culture. *Cell Transplant.* 10, 441-445.
  9. Tsuchiya, K., Chen, G.P., Ushida, T., Matsuno, T., Tateishi, T., 2004. The effect of coculture of chondrocytes with mesenchymal stem cells on their cartilaginous phenotype in vitro. *Mat. Sci. Eng. C-Bio S* 24, 391-396.
  10. Furukawa, K.S., Suenaga, H., Toita, K., Numata, A., Tanaka, J., Ushida, T., Sakai, Y., Tateishi, T., 2003. Rapid and large-scale formation of chondrocyte aggregates by rotational culture. *Cell Transplant.* 12, 475-479.
  11. Rook, M.B., van Ginneken, A.C., de Jonge, B., el Aoumari, A., Gros, D., Jongasma, H.J., 1992. Differences in gap junction channels between cardiac myocytes, fibroblasts, and heterologous pairs. *Am. J. Physiol.* 263, C959-977.
  12. White, T.W., Bruzzone, R., 1996. Multiple connexin proteins in single intercellular channels: connexin compatibility and functional consequences. *J. Bioenerg. Biomembr.* 28, 339-350.
  13. Donahue, H.J., Guilak, F., Vander Molen, M.A., McLeod, K.J., Rubin, C.T., Grande, D.A., Brink, P.R., 1995. Chondrocytes isolated from mature articular cartilage retain the capacity to form functional gap junctions. *J. Bone Miner. Res.* 10, 1359-1364.
  14. Ushida, T., Furukawa, K., Toita, K., Tateishi, T., 2002. Three-dimensional seeding of chondrocytes encapsulated in collagen gel into PLLA scaffolds. *Cell Transplant.* 11, 489-494.

# INTERRELATIONSHIP BETWEEN WATER FILTRATION VELOCITY AND THE THICKNESS OF PSEUDOINTIMA FORMED AT THE WALL OF ARTIFICIAL VASCULAR GRAFTS IMPLANTED IN THE DOG COMMON CAROTID ARTERY

T. KARINO, M. KAICHI AND T. ISHIZAKA

*Laboratory of Biofluid Dynamics, Research Institute for Electronic Science,  
Hokkaido University, North 12, West 6, North District, Sapporo 060-0812, Japan  
E-mail: karino@bfd.es.hokudai.ac.jp*

It is suspected that due to the presence of a filtration flow of water at the vessel wall, concentration polarization of low-density lipoproteins (LDL) occurs at the luminal surface of an implanted graft, leading to an increase in the uptake of LDL by the cells forming a pseudointima, rapid proliferation of the cells, and eventual development of intimal hyperplasia in the graft. Hence we have studied the interrelationship between water filtration velocity at the vessel wall measured before and after implantation of the graft and the thickness of a pseudointima formed in the graft by implanting three kinds of artificial grafts having an approximately the same diameter (3.0 mm) but very different water permeability at the vessel wall into the common carotid artery of the dog and harvesting them at different times postoperatively. It was found that the greater the water filtration velocity measured before and after implantation of the graft, the greater the thickness of the pseudointima formed in the graft, suggesting the importance of the filtration flow of water which cause concentration polarization of LDL at the luminal surface of the implanted graft in the development of intimal hyperplasia.

## 1 Introduction

One of the big problems in carrying out vascular reconstructive procedures using small diameter artificial grafts is the development of intimal hyperplasia that occurs late postoperatively. For implanted grafts, in order to perform the same functions as host arteries for a long time, it is necessary to maintain non-thrombogenicity and prevent narrowing of the vessel lumen due to the development of intimal hyperplasia. It has been shown that the intimal hyperplasia that develops in implanted vein grafts resembles well the pathological change of the vessel wall observed at the early stage of atherosclerosis, and in some advanced cases, intimal hyperplasia develops into atherosclerosis. Thus atherosclerosis and intimal hyperplasia have been studied by many investigators of all over the world and from various points of view, producing numerous numbers of reports on them. It has been shown that intimal hyperplasia develops the slower the flow velocity (the lower the shear rate) [1-5] and the higher the concentration of lipoproteins in blood [6]. As an initial event, it is known that there occurs first an accumulation of low-density lipoproteins (LDL: main carriers of cholesterol in flowing blood) in subendothelial spaces [7-9]. Then it is followed by adhesion of macrophages onto the endothelium and intrusion into the subendothelial

spaces to recover the accumulated LDL, becoming foam cells [10], thus increasing the thickness of the intima at such sites. It has been also reported that the degree of intimal thickening that occurs in autologous vein grafts is lower than that occurs in artificial grafts [11], and in the case of autologous arterial grafts such as the internal mammary artery, gastric artery, and radial artery, intimal thickening hardly occurs [12, 13]. Furthermore, with regard to artificial grafts, it has been reported that the lower the porosity, the lower the degree of intimal thickening [14], and in the case of nonporous grafts, intimal thickening do not occur at all [15]. Here the porosity is used as a synonym of the permeability of the vessel wall to plasma. Although it is not clear whether the porosity plays an important role in the development of intimal hyperplasia even after a pseudointima is formed at the luminal surface of implanted grafts, from our point of view, all the phenomena mentioned above indicate that the lower the permeability of the wall of a graft to water, the lower the degree of intimal thickening formed in the graft.

In our laboratory, we have been carrying out a series of theoretical and experimental study on transport of lipoproteins that carry cholesterol (an important component of cell membranes) from flowing blood to an arterial wall taking an water-permeable nature of an arterial wall into consideration. As a result, we found a new phenomenon that due to a semi-permeable nature of a vascular endothelium which allows the passage of water and water-dissolved ions but not macromolecules such as plasma proteins and lipoproteins, flow-dependent concentration or depletion of plasma proteins and lipoproteins occurs at a blood-endothelium boundary [16-20], affecting the transport of low-density lipoproteins (LDL) which carry an important nutriment "cholesterol" from flowing blood to an arterial wall. Thus if we consider the case of implanting artificial grafts made of synthetic materials, since the water permeability of most of the grafts presently used clinically is incomparably higher than that of a host artery, it is very likely that the water permeability of the grafts remains high even after their implantation *in vivo*. Due to that, the concentration of LDL at the luminal surface of the grafts is elevated compared to that of host artery, resulting in augmented uptake of lipoproteins by the cells forming the pseudointima and eventual development of intimal hyperplasia at such sites. However, there have been no information on water filtration velocity at the wall of implanted grafts and its effects on the development of intimal hyperplasia that occurs in grafts implanted in the arterial system. Therefore we have studied the interrelationship between water filtration velocity at the vessel wall measured before and after the implantation of the graft and the thickness of a pseudointima formed in the grafts by implanting three kinds of artificial vascular grafts having an approximately the same diameter but very different water filtration velocity at the vessel wall into the common carotid artery of the dog and harvesting them at different times after implantation.

## 2 Materials and Methods

### 2.1 The vascular grafts

Three kinds of artificial vascular grafts having an approximately the same diameter (3.0 mm) but very different water filtration velocity at the vessel wall were prepared for implantation experiments. These included the grafts prepared by fixing the dog common carotid artery with glutalaldehyde and detoxifying with glutamic acid by the modification of the method of Grimm et al. [21] (GA graft), commercially available expanded poly-tetra-fluoro-ethylene grafts (ePTFE graft, IMPRA ePTFE graft, Bard Peripheral Vascular, Inc., Tempe, AZ), and polyester grafts (PE graft) which were hand made by wrapping a sheet of polyester cloth on a 3-mm diameter rod and fusing the edges using a plastic-bag sealer. Prior to implantation of the grafts, measurements of the inner diameter and water filtration velocity at the vessel wall were carried out on each graft at a transmural pressure of 100 mmHg and at 37°C by using a cell culture medium which did not contain serum and a head tank system shown in Fig. 1. The results are shown in Table 1.

Table 1. The inner diameter and water filtration velocity measured prior to the implantation of each vascular graft. (100 mmHg, 37°C)

Graft	Inner diameter [mm]	Water filtration velocity [cm/sec]
GA graft	2.7 – 3.2	$1.5 - 2.9 \times 10^{-5}$
ePTFE graft	3.0	$0.5 - 12.5 \times 10^{-2}$
PE graft	3.0	$1.7 - 7.7 \times 10^{-1}$

### 2.2 Procedures for implanting the grafts

Adult male mongrel dogs were used for this experiment. All animal experiments were carried out humanely in conformity with the "Guide for the Care and Use of Laboratory Animals" enunciated by the School of Medicine, Hokkaido University in 1988. The dog was sedated with ketamine hydrochloride by intramuscular injection of the drug and then anesthetized by giving sodium pentobarbital intravenously (30 mg/kg body weight), intubated, and maintained under anesthesia during the whole anastomotic procedures by further occasional administration of the drug. Then under sterile conditions, a median incision was made on the neck, and

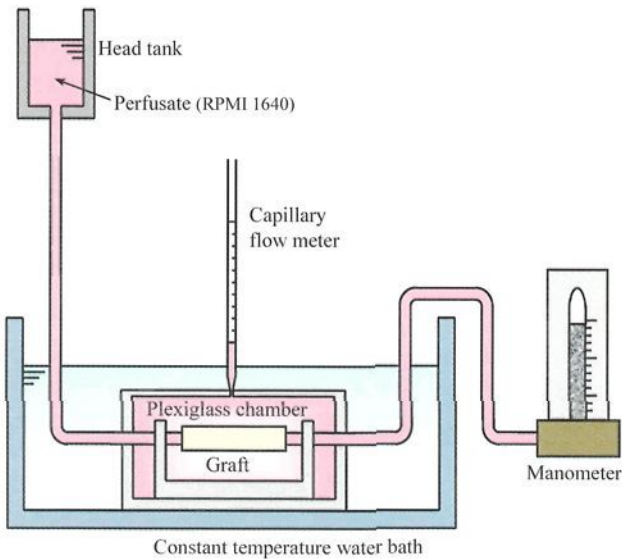


Figure 1. Schematic diagram of the perfusion system used for the measurements of water filtration velocity at the vessel wall of the grafts.

the bilateral common carotid arteries were exposed carefully. All the branches stemming from these arteries were ligated at locations close to their branching sites and then severed. An approximately 4-cm long segment of the common carotid artery was cut out at 90-degree angle, and a graft having a length of 4 cm were then implanted at its position by performing end-to-end anastomoses by a technique of an extraluminal continuous over-and-over suture with 7-0 Surgilene (monofilament polypropylene suturing thread). To protect the operated dogs from infectious diseases, two kinds of antibiotics were administered. Cefotaxime (500 mg) was given intravenously twice on the day of operation, and cephalexin (1 mg) was given orally twice a day for 5 postoperative days. Neither anticoagulants nor platelet antiaggregating drugs were used. Dogs were kept from 1 week to 13 months for recovery and healing, and then they were brought back to the operating room and the implanted vessels were harvested under general anesthesia with sodium pentobarbital.

### 2.3 Measurements of water filtration velocity and the thickness of pseudointima

Measurements of water filtration velocity at the vessel wall were carried out on all the harvested grafts at 37°C within 1 hour after harvesting the grafts by perfusing a cell culture medium under various pressures using the head tank system shown in Fig. 1. The inner diameter of the implanted graft and the thickness of the pseudointima formed in each graft were measured by preparing thin sections of the vessel, staining



them with hematoxylin-eosin and Verhoeff-van Gieson elastica stains, and photographing the sections under a light microscope. Observations of the luminal surface of the grafts were also carried out using a scanning electron microscope.

### 3 Results

#### 3.1 Histological observation of harvested grafts

Observation of the luminal surface of the GA graft before implantation showed that there was no endothelial cell and bare internal elastic lamina was exposed. In the GA graft harvested one week postoperatively showed that the luminal surface was covered with a smooth thin layer of fibrin, and it was also the same even in the graft harvested at 12 months postoperatively as shown in Figs. 2A and 3A. The luminal surface of the ePTFE graft observed before implantation showed that although the graft was pre-clotted with native whole blood, no thrombus was formed and fibrils of the graft were exposed and red cells were seen attached here and there. The luminal surface of the ePTFE graft harvested at one week postoperatively was coated with a smooth thin layer of fibrin containing red cells and white cells. However, the fibrin layer was composed partly of a layer with smooth surface which was the same as that observed in GA graft at one week postoperatively and partly with a layer with rough

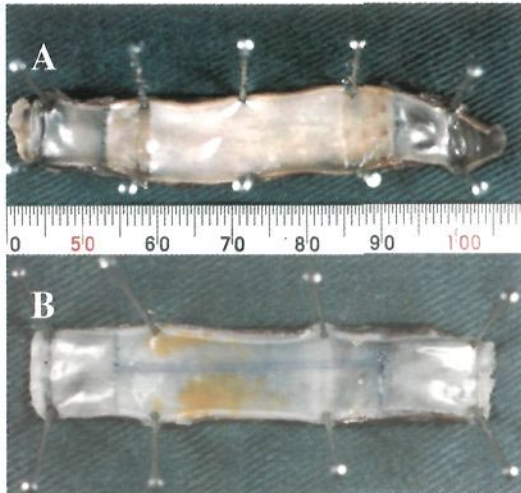


Figure 2. Photographs of the harvested and longitudinally opened grafts showing the gross appearance of their luminal surfaces. A: GA graft (12 months), B: ePTFE graft (13 months).

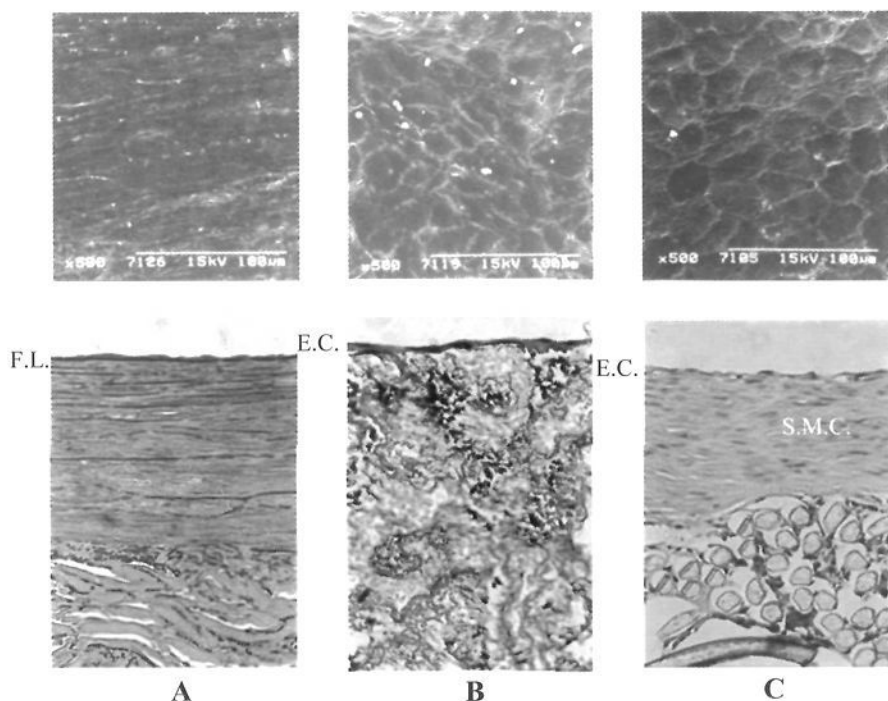


Figure 3. Photographs of the luminal surface of the harvested grafts observed with a scanning EM (upper) and a light microscope (lower) . A: GA graft (12 months), B: ePTFE graft (13 months), C: PE graft (2 months). F.L.: fibrin layer, E.C.: endothelial cells, S.M.C.: smooth muscle cells.

surface. The luminal surface of the graft harvested at 6 months postoperatively was partly covered with endothelial cells and partly with a fibrin layer containing red cells. The luminal surface of the ePTFE graft harvested at 13 months postoperatively was covered with a thin layer of cellular materials as shown in Fig. 2B, and the surface was completely coated with a monolayer of irregular-shaped endothelial cells as shown in Fig. 3B. The luminal surface of the PE graft observed before implantation was covered with a fibrin layer containing many red cells since it was pre-clotted with native whole blood. In the PE graft harvested at one month postoperatively, it was found that although most of the luminal surface was covered with a fibrin layer, there were some areas where the cells that were considered to have intruded from outside of the vessel wall reached the luminal surface. In the PE graft harvested at 2 months postoperatively, a pseudointima consisting of cellular materials and incomparably thicker than that found in ePTFE grafts was formed, and the luminal surface was completely covered with a monolayer of endothelial cells as shown in Fig. 3C.

### 3.2 Water filtration velocity at the vessel wall of harvested grafts

Measurements of water filtration velocity at the vessel wall were carried out on all the harvested grafts. Figure 4 shows the relationship between perfusion pressure and water filtration velocity at the wall of the three different types of implanted and harvested grafts. It was found that, in all the grafts, water filtration velocity increased almost linearly with increasing perfusion pressure. However, there was a clear difference in absolute value among the three types of grafts as it was so before their implantation, and the graft that showed the highest water filtration velocity before implantation showed the highest value even after its implantation in vivo. Figure 5 shows the relationship between water filtration velocity measured at a transmural pressure of 100 mmHg and the duration of implantation of all the grafts. As evident

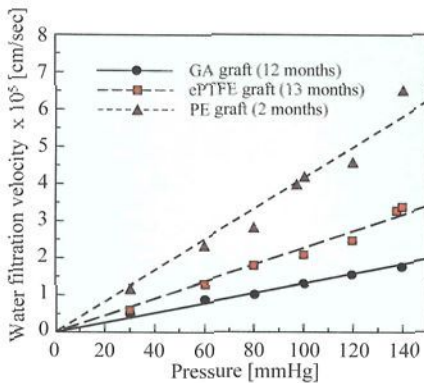


Figure 4. Relationship between perfusion pressure and water filtration velocity at the wall of the implanted grafts.

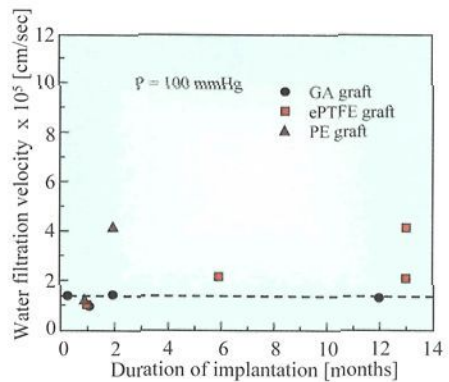


Figure 5. Relationship between the duration of implantation of the grafts and water filtration velocity at the wall of the implanted grafts.

from the figure, in all the grafts, the values of water filtration velocity at the wall became smaller than those measured before their implantation, and approached the value obtained with dog common carotid arteries. Thus in the case of the GA grafts which showed the lowest value of  $(1.5 - 2.9) \times 10^{-5}$  cm/sec before implantation, the water filtration velocity remained almost the same even at 12 months postoperatively. In the cases of the ePTFE grafts and PE grafts that showed very high filtration velocities (in the order of  $10^{-2}$  and  $10^{-1}$  cm/sec, respectively) even after a pre-clotting procedure was performed on them, the filtration velocity dropped drastically to the order of  $10^{-4}$  and  $10^{-3}$  cm/sec, respectively, at 1 week postoperatively, and to the order of  $10^{-5}$  cm/sec at 1 to 13 months in both cases which was very close to the value obtained with freshly excised dog common carotid arteries (host artery:  $1.4 \times 10^{-5}$  cm/sec).

### 3.3 Thickness of the pseudointima formed in implanted grafts

Measurements of the thickness of the pseudointima formed in implanted grafts were carried out on all the grafts. The results are shown in Fig. 6 as a plot of the duration of implantation of the graft versus the thickness of the pseudointima formed at the wall of the implanted graft. In the case of the GA graft, the luminal surface was occupied with a thin layer of fibrin-like material at any time postoperatively, and the thickness of the layer was approximately 20  $\mu\text{m}$  even in the graft harvested at 12 months postoperatively, indicating that almost no intimal thickening occurred in this vessel. In the case of the ePTFE grafts, at the time of one month postoperatively, the

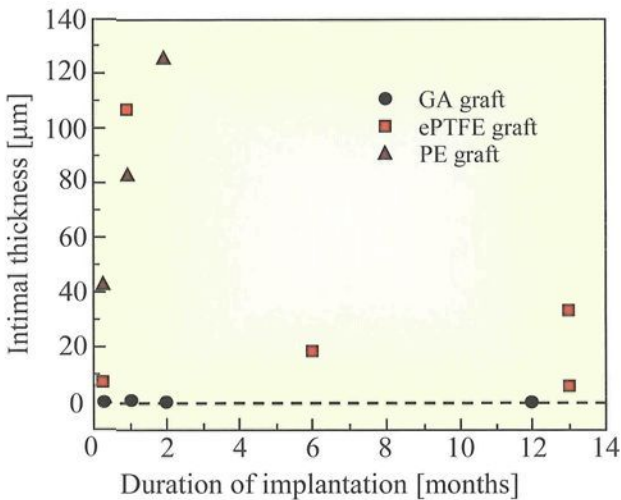


Figure 6. The relationship between the duration of implantation of the graft and the thickness of the pseudointima formed at the wall of the implanted graft.

luminal surface of the graft was occupied with a relatively thick layer of fibrin and thrombotic material with a thickness of approximately 100  $\mu\text{m}$ . However, with increasing the duration of implantation, the content of the pseudointima was replaced with cellular materials coated with a layer of endothelial cells at the luminal surface, and the thickness of the pseudointima diminished to 34  $\mu\text{m}$  at 13 months postoperatively. In the case of the PE graft, the pseudointima which consisted of mainly fibrin and thrombotic materials at 1 month changed to cellular materials coated with a monolayer of endothelial cells, giving a thickness of 126  $\mu\text{m}$  at 2 months postoperatively.



#### 4 Concluding Remarks

We have studied the changes in water filtration velocity at the vessel wall and the thickness of pseudointima formed in the grafts as a function of the time lapsed after implantation by implanting 3 types of artificial grafts having very different water permeability into the common carotid artery of the dog and harvesting them at different times postoperatively. As the results, it was found that despite of the large difference in water filtration velocity at the vessel wall among the 3 types of grafts measured prior to their implantation, the water filtration velocities dropped drastically within one month after their implantation and attained values in the same order as that obtained with freshly excised dog common carotid arteries (host artery). However, there were some differences among the 3 types of grafts in the process by which pseudointima was formed and the thickness of the pseudointima formed in each graft. Thus in GA graft that showed the lowest water filtration velocity that were almost equal to that obtained with freshly excised dog common carotid arteries (host artery) prior to their implantation *in vivo*, the pseudointima was composed of fibrin-like materials and no smooth muscle cell nor endothelial cell was present

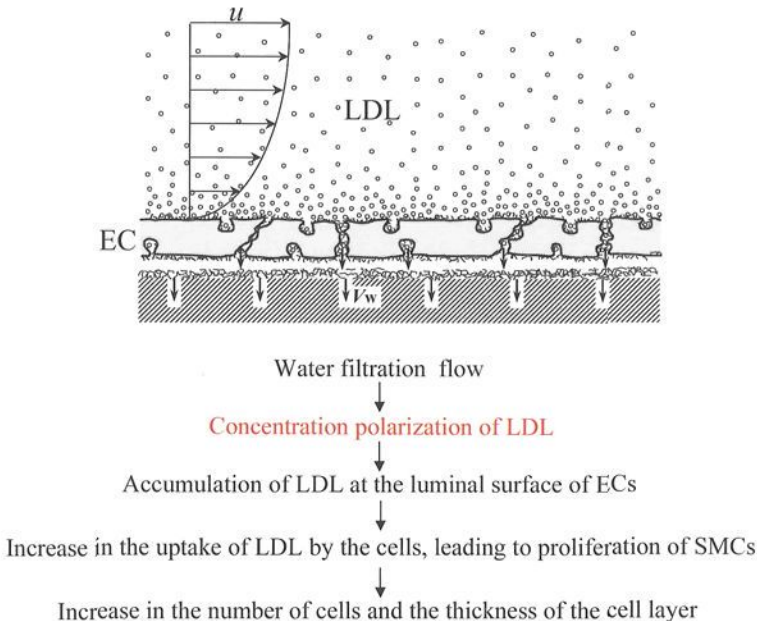


Figure 7. Schematic representation of the role of water filtration flow at the vessel wall in concentration polarization of LDL and development of intimal hyperplasia.

there even one year after implantation of the graft. In contrast to this, in the PE grafts that showed the highest water filtration velocity prior to their implantation, the pseudointima was composed of cellular materials that seemed to have intruded from outside of the graft even only 2 months after implantation of the graft, and it was the thickest of all the 3 types of grafts. Based on these results, it was considered that, as we suspected earlier in Introduction, due to the presence of a filtration flow of water at the vessel wall, concentration of low-density lipoproteins (LDL) occurred at the luminal surface of the implanted grafts as shown in Fig. 7, providing the highest surface concentration of LDL at the wall of PE grafts that showed the highest water filtration velocity both before and after implantation of the grafts. Then this caused migration of smooth muscle cells and fibroblasts from exterior and enhanced the uptake of LDL by the cells, resulting in their rapid proliferation and eventual formation of pseudointima that was the thickest in all the 3 types of grafts used for implantation experiments. If we consider the case where a non-porous graft is implanted, since there is no filtration of water at the vessel wall, no accumulation of LDL will occur at the luminal surface of the graft. Thus no intimal hyperplasia will occur in such vessels as it was demonstrated in several animal experiments [15, 22]. These results suggest the possibility that anastomotic intimal hyperplasia that develops at sites of anastomotic junctions might be prevented or at least alleviated by locally lowering water permeability of the graft either by the application of certain drugs which reduce the permeability of the implanted graft as well as the host artery, or by covering the region of anastomotic junction with an external support. With respect to this, there have been several reports that support our idea. It was shown that it is possible to reduce neointimal and medial thickening that form in porcine saphenous vein bypass grafts by placing a macro-porous external stent [23] and protect vein grafts implanted in the common carotid artery of the rabbit from atherosclerosis by placing a rigid external support [24].

### **Acknowledgements**

This work was supported by Grant-in-Aid for Scientific Research 15086201 from the Ministry of Education, Science, Sports and Culture of Japan and partly by a Grant-in-Aid for Scientific Research 15300150 from Japan Society for the Promotion of Science (JSPS).

### **References**

1. Morinaga, K., Eguchi, H., Miyazaki, T., Okadome, K., Sugimachi, K., 1987. Development and regression of intimal thickening of arterially transplanted autologous vein grafts in dogs. *J. Vasc. Surg.* 5, 719-730.

2. Kraiss, L.W., Kirkman, T.R., Kohler, T.R., Zieler, B., Clowes, A.W., 1991. Shear stress regulates smooth muscle proliferation and neointimal thickening in porous polytetrafluoroethylene grafts. *Arteriosclerosis and Thrombosis* 11, 1844-1852.
3. Mattsson, E.J.R., Kohler, T.R., Vergel, S.M., Clowes, A.W., 1997. Increased blood flow induces regression of intimal hyperplasia. *Arteriosclerosis, Thrombosis, and Vascular Biology* 17, 2245-2249.
4. Meyerson, S.R., Skelly, C.R., Curi, M.A., Shakur, U.M., Vosicky, J.E., Glagov, S., Schwartz, L.B., 2001. The effects of extremely low shear stress on cellular proliferation and neointimal thickening in the failing bypass graft. *J. Vasc. Surg.* 34, 90-97.
5. Verceli, S.A., Davies, M.G., Kenagy, R.D., Clowes, A.W., 2002. Flow-induced neointimal regression in baboon polytetrafluoroethylene grafts is associated with decreased cell proliferation and increased apoptosis. *J. Vasc. Surg.* 36, 1248-1255.
6. Hoff, H.F., Beck, G.J., Skibinski, C.I., Jürgens, G., O'Neil, J., Kramer, J., Lytle, B., 1988. Serum Lp(a) level as a predictor of vein graft stenosis after coronary artery bypass surgery in patients. *Circulation* 77, 1238-1244.
7. Miller, A., Schoen, F.J., Lees, A.M., Fallon, J.T., Strauss, H.W., Lees, R.S., 1987. Low density lipoprotein accumulation by PTFE grafts in the rabbit aorta: autoradiographic-morphologic correlations. *Trans. Am. Soc. Artif. Intern. Organs XXXIII*, 489-493.
8. Chignier, E., Guidollet, J., Lhopital, C., Louisot, P., Eloy, R., 1990. Lipid accumulation in prosthetic vascular grafts. *Am. J. Pathol.* 137, 531-540.
9. Baumann, D.S., Doblas, M., Daugherty, A., Sicard, G., Schonfeld, G., 1994. The role of cholesterol accumulation in prosthetic vascular graft anastomotic intimal hyperplasia. *J. Vasc. Surg.* 19, 435-445.
10. Zwolak, R.M., Kirkman, T.R., Clowes, A.W., 1989. Atherosclerosis in rabbit vein grafts. *Arteriosclerosis* 9, 374-379.
11. DeWeese, J.A., 1978. Anastomotic intimal hyperplasia. In: Sawyer, P.N., Kaplitt, M.J., (Eds). *Vascular grafts*. New York, Appleton-Century-Crofts, pp. 147-152.
12. Cameron, A., Kemp, H.G., Green, G.E., 1986. Bypass surgery with the internal mammary artery graft: 15 year follow-up. *Circulation* 74(Suppl III), 111-130.
13. Grondin, C.M., Campeau, L., Lesperance, J., Enjalbert, M., Bourassa, M.G., 1984. Comparison of late changes in internal mammary artery and saphenous vein grafts in two consecutive series of patients 10 years after operation. *Circulation* 70(Suppl. 1), I-208-212.
14. Campbell, C.D., Goldfarb, D., Roe, R., 1975. A small arterial substitute: Expanded microporous polytetrafluoroethylene: patency versus porosity. *Annals of Surgery* 182, 138-143.

15. Hunter, G.C., Carson, S.N., Wong, H.N., French, S., 1980. Experimental small-diameter graft patency: Effect of compliance, porosity and graft healing potential. *Current Surgery* , 439-441.
16. Wada, S., Karino T., 1999. Theoretical study on flow-dependent concentration polarization of low density lipoproteins at the luminal surface of a straight artery. *Biorheology* 36, 207-223.
17. Wada, S., Karino, T., 2002. Prediction of LDL concentration at the luminal surface of a vascular endothelium. *Biorheology* 39, 331-336.
18. Naiki, T., Sugiyama, H., Tashiro, R., Karino, T., 1999. Flow-dependent concentration polarization of plasma proteins at the luminal surface of a cultured endothelial cell monolayer. *Biorheology* 36, 225-241.
19. Wada, S., Karino, T., 2002. Theoretical prediction of low-density lipoproteins concentration at the luminal surface of an artery with a multiple bend. *Ann. Biomed. Eng.* 30, 778-791.
20. Wada, S., Koujiya, M., Karino, T., 2002. Theoretical study of the effect of local flow disturbances on the concentration of low density lipoproteins at the luminal surface of end-to-end anastomosed vessels. *Med. Biol. Eng. Comput.* 40, 576-587.
21. Grimm, M., Eybl, E., gravenwöger, M., Spreitzer, H., Jäger, W., Grimm, G., Böck, P., Müller, M.M., Woloner, E., 1992. Glutaraldehyde affects biocompatibility of bioprosthetic heart valves. *Surgery* 111, 74-78.
22. Lumsden, A.B., Changyi, C., Coyle, K.A., Ofenloch, J.C., Wang, J-H., Yasuda, H.K., Hanson, S.R., 1996. Nonporous silicone polymer coating of expanded polytetrafluoroethylene grafts reduces graft neointimal hyperplasia in dog and baboon models. *J. Vasc. Surg. Online* 24(5), 1-10.
23. Batellier, J., Wassef, M., Merval, R., Duriez, M., Tedgui, A., 1993. Protection from atherosclerosis in vein grafts by a rigid external support. *Arteriosclerosis and Thrombosis* 13(3), 379-384.
24. George, S.J., Izzat, M.B., Gadsdon, P., Johnson, J.L., Yim, A.P.C., Wan, S., Newby, A.C., Angelini, G.D., Jeremy, J.Y., 2001. Macroporosity is necessary for the reduction of neointimal and medial thickening by external stenting of porcine saphenous vein bypass grafts. *Atherosclerosis* 155, 329-336.



# STRENGTHENING OF FIBROUS TISSUES UNDER MECHANICAL STIMULI

K. TAKAKUDA

*Tokyo Medical and Dental University,  
2-3-10 Kanda-Surugadai, Chiyoda-ku, Tokyo 101-0062, Japan  
E-mail: takakuda.mech@tmd.ac.jp*

The effects of mechanical stimuli to the fibrous tissues were investigated utilizing the collagen gel culture method. A specimen of thin collagen gel membrane, in which fibroblasts were proliferating and was supported by stainless steel wire mesh, was cultured in medium and subjected to static or repeated dynamic uniaxial tensile/compressive load in an incubator. The cell alignment and the shrinkage of collagen gel matrix were observed. Furthermore, mechanical tests were carried out under microscope and changes in mechanical properties of the specimens were measured. We found that both of static and dynamic loads strengthened the collagen matrix, however, the dynamic stimuli were concluded to be more effective in matrix strengthening than the static stimuli.

## 1 Introduction

Fibrous connective tissues such as tendons and ligaments have an ability to adapt to mechanical environments. Such functions attracted attentions of many researchers and some investigations have been carried out [1,2], but majority of them were of animal experiments of organ level and few were focused on cellular level responses. Since any functions of tissues originate from the involving cells, investigation of cellular phenomena is necessary to understand the mechanism of the adaptation of fibrous tissues.

Collagen gel culture technique [3] enables us to realize the environment for cells similar to that observed *in vivo*. We also have developed the experimental culture model [4,5] to investigate mechanical behaviors of fibroblasts in collagen gel, and showed that fibroblasts generates tensile stresses and the cells align in the direction of tensile stress. In these experiments, however, the mechanical environments around the cells were static ones. While it was well known that the dynamic stimuli affects the cells significantly [6-9], experimental models have not been developed that enable us to examine the effect of controlled mechanical stimuli on the specimens of collagen gel and measure the change of mechanical properties of the collagen matrix. Hence here we constructed the equipment for the application of repeated dynamic mechanical stimuli to specimens of collagen gel, and we investigated the strengthening of the fibrous tissues under mechanical stimuli.

## 2 Materials and Methods

### 2.1 Materials

Fibroblast-like cells were obtained from synovial membrane of a knee joint of Japanese white rabbit by the explant method, and cultured in an incubator with 37 °C and 5% CO<sub>2</sub> environment. The medium was  $\alpha$ MEM with nucleosides (GIBCO), with 10% calf serum and 60  $\mu$ g/ml kanamicin. The cells were subcultured by the trypsin/EDTA solution digestion method. Since the cells after repeated subculture lost ability to contract collagen gel, the generations of 1st to 5th were used for the experiments.

Figure 1 is the schematic illustration of the specimen for culture. The supporting parts made with stainless steel mesh were divided to the upper and the lower parts and had a square hole of 5x5 mm between them. The reconstituting collagen solutions were 8 parts of 0.3% collagen solution (CELL MATRIX type I-A, Nitta), 1 part of x10 solution of MEM (Nissui), and 1 part of buffer (HEPES 4.77g/0.08N NaOH solution 100ml). The mixed solution of them was poured onto the supporting part placed on the silicone rubber mold of 10x10 mm. After the collagen gelation, the cuts were made along both sides of the center hole, and we had the thin collagen gel membrane specimen of 5mm length, 5mm width, and ca.1mm thickness supported by the stainless steel wire mesh[4]. In the experiments for the observation of cell morphology, the mass of the cells of ca. 1mm<sup>3</sup> were placed at the upper ends of the specimen and let the cell immigrate from there. In the experiments for the measurement of the mechanical properties of the specimens, the cells were dispersed over the collagen gel uniformly with the density of 0.2 x 10<sup>6</sup>/ml.

### 2.2 Experimental apparatus

Fibroblasts cultured in collagen gel generate tensile stresses and aligns in the direction of the tensile stress [4,5]. Hence in the static experiments to elucidate the effects of static stress on the cells, the both supporting parts were fixed and the static tensile stresses were generated in the specimens by the functions of the cells. In the dynamic experiments, an apparatus for the applications of repetitive tensile load to the specimens as shown in Figure 2 was constructed. The apparatus was composed of

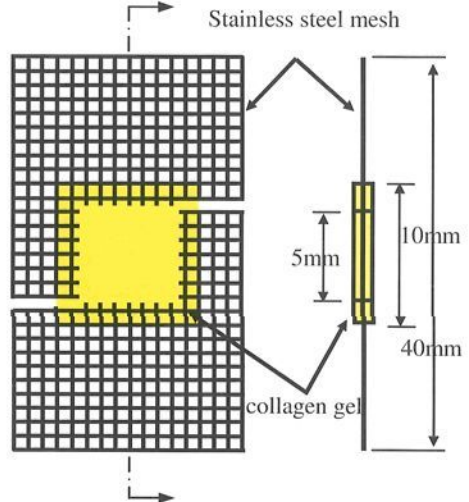


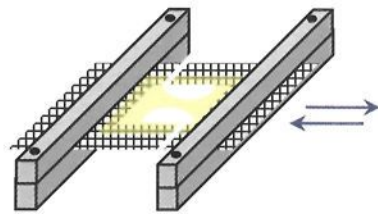
Figure 1. Collagen gel specimen.

autoclavable chambers for the specimens and an actuator equipped with an air cylinder. The aluminum chamber shown in Figure 2(b) holds the culture dish (60mm diameter, Corning) filled with the medium. The specimen was clamped by the stainless steel jigs at the mesh supports and kept within the medium. The jigs were fixed to stainless steel rods, which run through holes on the chamber wall. One end of the rod was connected to the actuator, and the other end to an adjustable stopper that enabled us to set the magnitude of the displacement of the rod. The setup of apparatus in an incubator is shown in Figure 2(c). The rod moved linearly along the hole on the chamber wall, and thus introduces the repeated dynamic mechanical stimuli to the specimens.

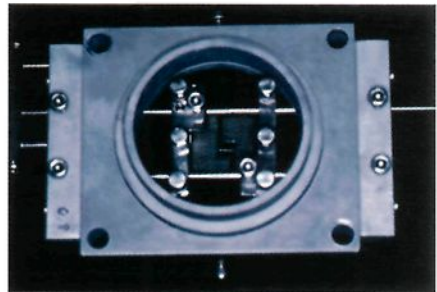
### 2.3 Experimental conditions

In the static experiments, the both ends of the specimen were fixed and the original length of 5mm of the specimen was kept constant throughout the experiments. Although no external load was applied to the specimen, tensile stresses were generated in the specimen by the functions of the cells.

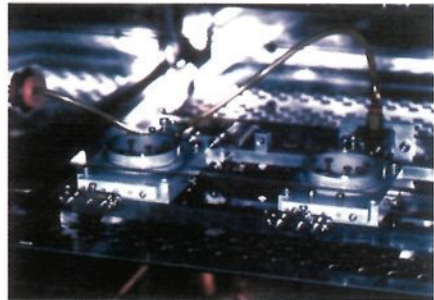
In the dynamic experiments, the magnitude of the displacement was set to be 0.5mm and thus the strain of the specimen was set as 10%. The displacement cycles were 5 sec for stretching and 5 sec for compression, continuously applied throughout the experiments. The original length of the specimen was set as the maximum stretch position, and the experiment was carried out in the compressive side from this setting. Just after the beginning of the experiment, the specimen was so soft and flexible that it bent at the maximum compressive position, and virtually no compressive stresses were induced in the specimen. As the experiment proceeds, the cells in the specimen generated tensile stresses, the rigidity of the specimen increased, so the tensile and/or compressive



(a) Dynamic stimuli for specimen.



(b) Specimen chamber.



(c) Loading apparatus in an incubator.

Figure 2. Loading apparatus.

stresses were induced in the specimen. We had made no attempts to measure the magnitude of the stress in this experiment.

In the experiments for the cell morphology, the observations become difficult as the density of the cells increases. Hence the experiments were carried out mainly for the case of the cells proliferating from one end[4,5]. The length of the experimental period was 3 weeks or as long as the occurrence of the specimen's failure by self-elongation.

In the experiments for the measurement of mechanical properties of the specimens, the cells were dispersed over the collagen matrix uniformly. In some control experiments, specimens without any cells were made utilized. The experiments period were zero (just after the making of the specimens) and 1 week for the specimens without the cells, and 0 week (1 day after the making of the specimens), 1, 2 and 3 weeks for the specimens with the cells.

#### 2.4 Evaluation of the specimens

Throughout the experimental periods, the specimens were observed time to time with a phase contrast microscope (Diaphot TMD, Nikon) and the shape of the specimens and the alignment of the cells were photographed. The planar shapes and the thickness of the specimens were measured by a tool microscope (Shadow Graph Model 6, Nikon), and the cross-sectional areas of the specimens were calculated assuming elliptical shapes of the sections.

After attachment of carbon particles as markers, the specimen was kept in PBS and was tested under a stereo microscope (SMZ-U, Nikon). The specimen was elongated by a linear motor (MLA-7020, Micron Kiki) with the crosshead speed of 2mm/min and the load was measured by a load cell (120T-100B, Kyowa Electric). The deformation induced in the specimens was monitored by a video camera and recorded. The images of the specimen were analyzed at 5 locations on the central longitudinal axis, i.e. at the edge parts (0.5mm apart from the end), the intermediate parts (1.5mm apart from the end), and the central part (2.5mm apart from the end). The location changes of marker particles in respective parts were analyzed to give the strains and the load-displacement diagram obtained was converted to the stress-

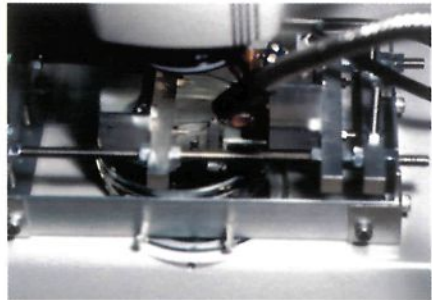
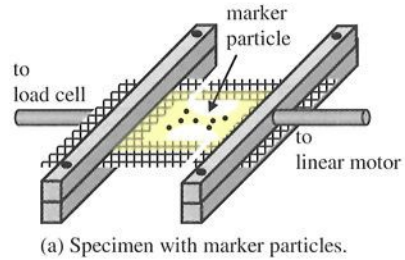


Figure 3. Optical strain measurement.



strain diagram. The maximum tensile stress was calculated as the maximum load divided by the minimum cross sectional area, and the elastic modulus of the specimen was calculated assuming a linear responses from the starting point and the failure point in the stress-strain diagram.

### 3 Results

The results are presented for the cases of specimens with the cells immigrating from one end and the cases of specimens with the uniformly dispersed cells. To specify the directions in the specimens, we would refer the vertical direction of the specimen shown in Fig. 1 as longitudinal, and the horizontal direction as lateral. Furthermore, the portions of the area close to the horizontal edges of the specimen would be referred as the sides, and central portion in the lateral direction as the center. The portion of the area close to the vertical end of the specimen as the upper and the lower, and the central portion as the middle.

#### 3.1 Deformation of specimens with cells immigrating from one end

The upper photographs in Figure 4 show the typical shape change observed in experiments. In the photograph, the bright areas were where significant number of cells was proliferating. The shrinkage of the specimen in the lateral direction was observed. The cells were proliferating along the longitudinal direction, and the rate

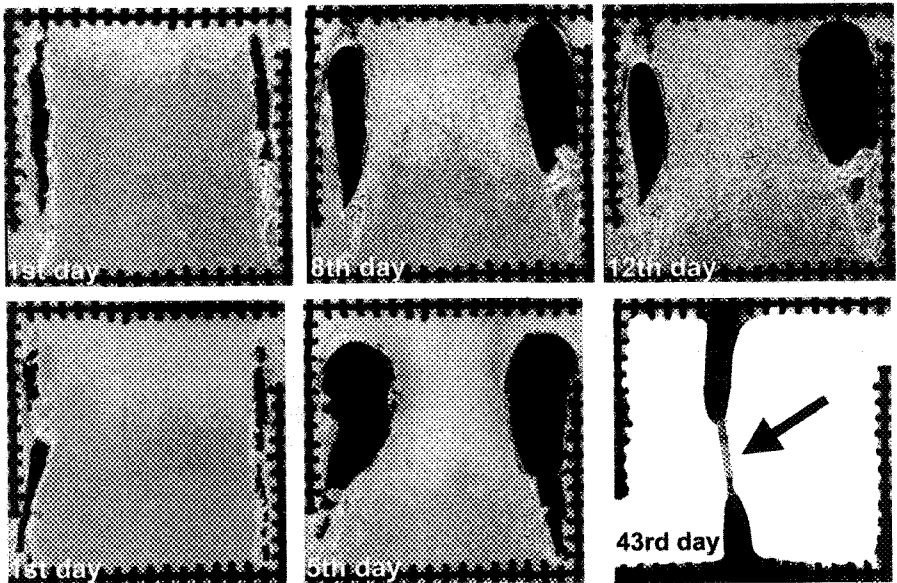


Figure 4. Deformation of specimens with cells immigrating from one end. Upper: Static condition, lower: dynamic condition.

of proliferation was nearly uniform along the lateral direction. It was also observed that the cells aligned in the longitudinal direction. This alignment direction did not change throughout the experiment. As the culture period prolonged, the shrinkage in the lateral direction proceeded and finally the specimen failed spontaneously.

The lower photographs in Figure 4 show the typical example of the case of dynamic experiments. The shrinkage in the lateral direction was larger than that observed in the case of static experiments. The cell alignment was firstly in the longitudinal direction but when the cells reached to the middle of the specimen, although the cells in the sides kept alignment in the longitudinal direction, the cells in the central aligned in the lateral direction. The speed of proliferation in the central portion of the specimen was decreased compared to that of the cells in the sides. As longer the culture period became, the rigidity of the specimens increased, and some part of the specimen was compressed at the maximum compression position. In this case, the cells were killed over such area, but some collagen fibers were left and the specimen was bent around there and did not fail even after 43 days of incubation.

The above is the typical example of the results. Similar results were observed in repeated experiments and the qualitative reproducibility of the results was confirmed.

### 3.2 Deformation of specimens with uniformly dispersed cells

The specimen after 3 weeks incubation under the dynamic stimuli was shown in Figure 5. The upper photographs show the specimen under the static condition, and the lowers show that under the dynamic stimuli. The lefts show that in the maximum stretch position, and the rights in the maximum compression position. Although the

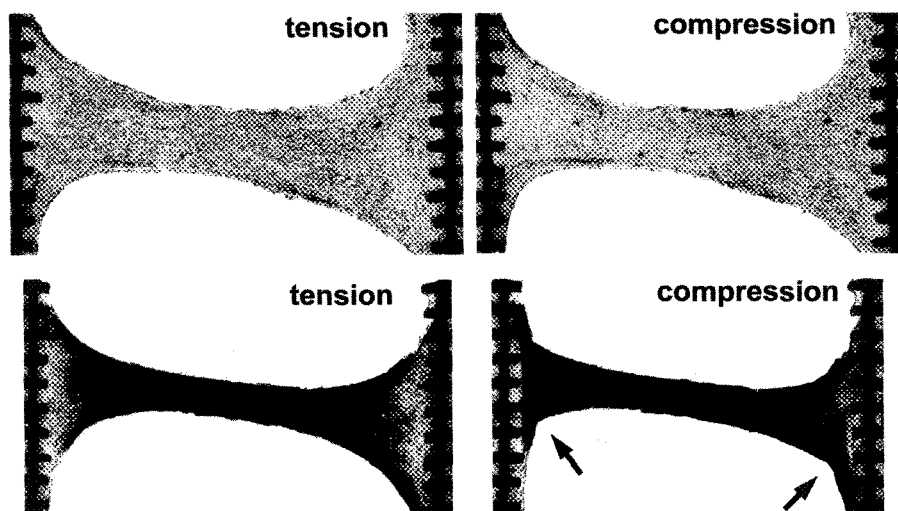


Figure 5. Specimens with cells uniformly dispersed after 3 weeks incubation. Upper: Static condition, lower: dynamic condition.

specimen under the static condition remained soft and stretchable, the specimen under the dynamic stimuli increased its rigidity at the middle part of the specimen so that the both ends of the specimen were compressed at the maximum compression position (the parts pointed by arrows in the figure). In the tensile tests, the failures of the specimens always took place in the both ends, and never at the middle parts where the cross sectional areas were minimum.

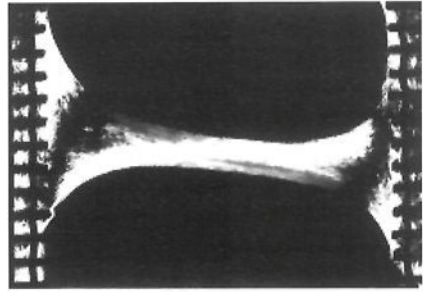


Figure 6. Collagen fibers in specimen observed by polarized light.

Figure 6 shows the same specimen under the dynamic stimuli but observed under the polarized light. The longitudinal alignment of collagen fibers along the direction of tensile stresses in the specimen can be clearly observed.

### 3.3 Mechanical properties of specimens with the cells

The maximum tensile stresses of the cultured specimens were shown in Figure 7. The solid circles indicate the mean values and the error bars express the standard deviations. The maximum

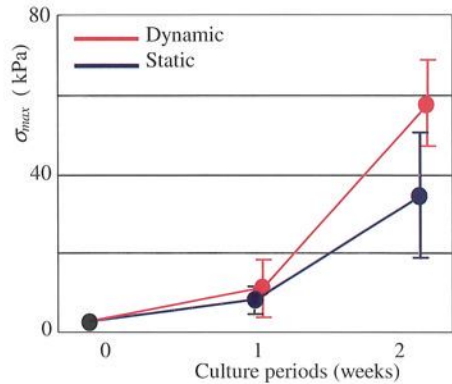


Figure 7. Maximum tensile stresses of cultured specimens.

tensile stresses were increasing with the increase of the culture periods in both specimens under static conditions and dynamic stimuli. Although we could observe the tendency that the maximum tensile stresses were larger in the specimens under dynamic stimuli than those under static conditions, the scatters in the results were so great that we could not have a statistically significant conclusion. This might be attributed to the fact that the failure occurred in either of the both ends of the specimens in which no effective strengthening by dynamic loading was took place.

The elastic moduli of the cultured specimens were measured and shown in Figure 8. Similar to the maximum tensile stresses, the moduli were increasing with the increase of the culture periods and we could observe the tendency that those under dynamic stimuli were greater than those under static conditions. Although we could not have statistical significances again for the modulus of the whole specimen, we could examine the respective parts of the specimens in this case of elastic modulus. Hence the changes of the elastic moduli of the respective parts of the

specimens, i.e., the centers (Cnt), the intermediates (Mid), and the edges (Edg) were shown in Figure 9. Similar to the moduli of the whole specimens, the moduli were increasing with the increase of the culture periods and furthermore we have statistic differences between the modulus under the dynamic and the static conditions at intermediate parts of 1 and 2 weeks culture periods (t-test,  $p < 0.05$ ).

## 4 Discussions

### 4.1 Cell alignments

We have already shown that fibroblasts in the specimens under the static condition generate tensile stresses and align in the direction of the tensile stress [4,5]. In this investigation, we again observed the same phenomena in the specimens under the dynamic stimuli. Furthermore, we observed the alignment of collagen fibers in the direction of tensile stress in the specimens under dynamic stimuli as shown in Figure 6. Although we could not identify the collagen fibers by the polarized light in the specimens under the static conditions, the cell alignments were believed to be induced by the alignments of the collagen fibers, and which were the result of the tensile stress induced in the collagen gels by the cells. The dynamic stimuli were seemingly more effective in the structuring performance of the collagen fiber than the static stimuli.

### 4.2 Strengthening of the matrix by cells

In this experiment, both of the maximum tensile stress and the elastic modulus of the specimen were increased as the culture period increased. Such phenomenon was never observed in the specimens without cells (data not shown), strengthening must

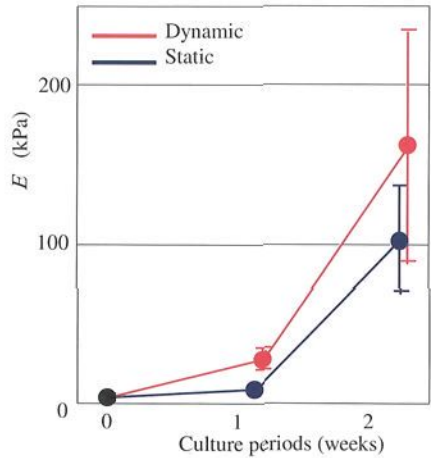


Figure 8. Elastic modulus of the whole cultured specimens.

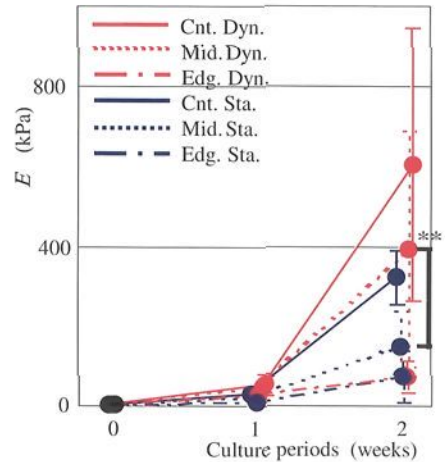


Figure 9. Elastic modulus of respective parts of cultured specimens.



be the function of the cells and the same mechanism of the *in vivo* strengthening may be responsible for this *in vitro* strengthening.

One candidate mechanism of the strengthening is such that as the cells contract and generate tensile stresses, the water among the three dimensional meshwork of collagen matrix is pushed away and the density of the matrix increased and the specific strength of the matrix increased. Since the gel contraction is a remarkable event that can be observed by the naked eyes, it surely must be considered to make some contributions to the strengthening phenomena. However, the above mechanism cannot explain the whole fact since the maximum tensile force as well as the maximum tensile stress was increased in this experiment. We believe that the cells must make such change in the collagen matrix structure as aligning the orientations of fibers and making bridges between fibers according to the tensile stresses.

We could not find the statistically significant difference in the mechanical properties of the whole specimens under the static conditions and those under the dynamic stimuli. The specimens under the static conditions were in tensile state and the cells may react to strengthen the collagen matrix in such a mechanical environment. But the specimen's strengthening was not so great that it broke spontaneously during the prolonged period of incubation. Furthermore, we could observe that collagen matrix itself flowed toward the supporting mesh at the middle part of the specimen. Hence the spontaneous failure was not that of the fracture as an elastic solid material but the flow of a viscoelastic liquid material. Hence we believe that the specimens under the static condition were so soft and weak that the strengthening of the specimens was not so significant phenomena and is not the counterpart of that observed *in vivo*.

The strengthening of the specimen under the dynamic stimuli was, contrary to that under the static condition, observable by naked eyes. For example, as shown in Figure 4, in the specimen that did not fail during prolonged incubation, we clearly observed the fibrous structure that evidenced that the specimen was of a solid. In Figure 5, the rigidity of the middle part of the specimen with uniformly dispersed cells was so increased that it could compress the both end parts of the specimen, and the middle part could be considered to be solid again.

The cells in both end parts of the specimen under dynamic stimuli of Figure 5 were aligned in the lateral directions. As Figure 6 reveals the collagen fibers there align in the lateral direction. The collagen matrix was transparent whereas the middle part of the specimen was not transparent and looked dark in phase contrast microscope. Since the transparency is directly related to low matrix density and low rigidity, we concluded that the end parts of the specimen were not strengthened at all. In fact, the elastic moduli at the edge parts were remained low. On the other hand, the cells in the center and the intermediate parts aligned in the longitudinal direction. The elastic moduli were increased at the intermediate parts and there were statistical significance between static and dynamic conditions.

Thus we conclude that the fibroblasts in specimens made of collagen gel significantly strengthen the specimens if they are stimulated by the repeated application of dynamic tensile stresses.

### **Acknowledgements**

This work was supported by Grant-in-Aid for Scientific Research on Priority Areas 15086206 from the Ministry of Education, Culture, Sports, Science and Technology of Japan.

### **References**

1. Tipton, C.M., James, S.L., Mergner, W., Tcheng, T., 1970. Influence of Exercise on Strength of Medial Collateral Knee Ligaments of Dogs. *Am. J. Physiol.* 218-3, 894-902.
2. Noyes, F.R., 1977. Functional Properties of Knee Ligaments and Alterations Induced by Immobilization. *Clin. Orthop. Rel. Res.* 123, 210-242.
3. Soc Tissue Culture Japan (Compiled), 1988. The technique of tissue culture (In Japanese), 315, Asakura Tokyo.
4. Takakuda, K., Miyairi, H., 1996. Tensile stresses generated by fibroblasts and automorphogenesis (An in vivo experiment) (In Japanese). *Tr JSME* 62-595, A, 800-807.
5. Takakuda, K., Miyairi, S., 1996. Tensile Behavior of Fibroblasts Cultured in Collagen Gel. *Biomaterials* 17, 1393-1397.
6. Hasegawa, S., Sato, S., Saito, S., Suzuki, Y., Brunette, D.M., 1985. Mechanical Stretching Increase the Number of Cultured Bone Cells Synthesizing DNA and Alters Their Pattern of Protein Synthesis. *Calcif. Tissue Int.* 37, 431-436.
7. Vandenburg, H.H., Hatfaludy, S., Karlisch, P., Shansky, J., 1991. Mechanically Induced Alternations in Cultured Skeletal Muscle Growth. *J. Biomech.* 24-sup1, 91-99.
8. Naruse, K., Sokabe, M., 1993. Involvement of Stretch-Activated Ion Channels in Ca<sup>2+</sup> Mobilization to Mechanical Stretch in Endothelial Cells. *Am. J. Physiol.* 264, C1037-C1044.
9. Kanda, K., Matsuda, K., Oka, T., 1993. Biomechanics under repeated stretch and compression (Auto alignment of vascular wall cells) (In Japanese) *Artificial Organs* 22-2, 483-487.

This page is intentionally left blank

## **IV. COMPUTATIONAL BIOMECHANICS**

This page is intentionally left blank

# ASSESSMENT OF CORTICAL BONE MICROSTRUCTURE USING MONOCHROMATIC SYNCHROTRON RADIATION MICRO-CT

T. MATSUMOTO, M. YOSHINO AND M. TANAKA

*Division of Bioengineering, Osaka University Graduate School of Engineering Science,  
1-3 Machikaneyama-machi, Toyonaka 560-8531, Japan  
E-mail: tanaka@me.es.osaka-u.ac.jp*

Monochromatic synchrotron radiation (SR) allows ultrahigh-resolution computed tomography (CT) and accurate density measurements. The purpose of this study was to demonstrate the utility of monochromatic SRCT in microstructural analysis of cortical bone. Tibial diaphyses of growing rat (14 weeks, n=8) undergoing unilateral sciatic neurectomy 8 weeks ago were imaged with 5.83- $\mu\text{m}$  voxel resolution by 20-keV SRCT at the synchrotron radiation facility (SPring-8). Reconstructed image data were translated into local mineral densities using a calibrated linear relationship between linear absorption coefficients and concentrations of homogeneous  $\text{K}_2\text{HPO}_4$  solution. After bone segmentation by a simple thresholding, pure bone 3D images were analyzed for macro- and microscopic structural properties. In neurectomized hindlimbs, the cortical canal network rarefaction as well as the bone atrophy were found. The former was characterized by 30% smaller porosity, 11% smaller canal density in transverse section, and 38% smaller canal link density than those in the contralateral bone, implying the reduced bone microcirculation in the disuse-induced atrophic tibia. On the other hand, no difference was found in the bone mineral density between neurectomized and intact hindlimbs. In conclusion, the SRCT is a promising method for the 3D analysis of cortical microstructure.

## 1 Introduction

The computed microtomography based on a microfocus X-ray source ( $\mu\text{CT}$ ) allows 3D microstructural analyses of trabecular bone (1-3), which is of great clinical interests because of its high turnover rate or high vulnerability to bone loss. On the other hand, only a few  $\mu\text{CT}$  studies have reported on cortical bone despite its microstructure or canal pore structure is closely related to the bone strength (4, 5) and the cortical microcirculation (6, 7). One reason would be that the resolution of conventional  $\mu\text{CT}$  is insufficient for quantification of cortical microstructure. Accordingly, the 2D histomorphometry or the 3D reconstruction based on serial histological sectional images has been mainly used for the cortical microstructural analysis (8, 9). However, such techniques are subject to deformation artifacts and time-consuming. Besides, anisotropic properties of cortical microstructure make it difficult to apply 2D image-based analyses.

The synchrotron radiation computed microtomography (SRCT) has opened up new possibilities in the 3D analysis of cortical microstructure (10-13). Natural collimation and extremely high light intensity of SR allow the reconstruction of highly resolved 3D images with a high signal-to-noise ratio. Furthermore, the

monochromatic X-ray, which eliminates beam hardening artifacts, is available for the determination of local bone mineralization (14-16).

To date, the ability of SRCT has been demonstrated mainly in cancellous bone analysis (14, 16-20); however, there have been very few SRCT measurements of cortical bone. Thus, the present study was aimed to demonstrate the availability of SRCT in cortical microstructural analysis by evaluating disuse-mediated changes of cortical microstructure in tibiae of growing rats.

## 2 Methods

Experiments were conducted according to the guiding principles of the American Physiological Society and with an approval of the Animal Research Committee of Osaka University Graduate School of Engineering Science.

The synchrotron radiation experiments were performed with the approval of the Japan Synchrotron Radiation Research Institute (JASRI).

### 2.1 Sample preparation

Six-week male Wistar rats (140-150 g, n=6) underwent the unilateral sciatic neurectomy of the left hindlimb under pentobarbital anesthetization. The right hindlimb was left intact. After the operation, the rats were housed singly and allowed free access to standard lab chow and tap water for eight weeks. Then, all rats, weighing 350-390 g, were sacrificed with the intravenous infusion of saturated KCl solution. Both tibiae in operated (OP) and intact (non-OP) hindlimbs were excised, cleaned of soft tissue, and soaked in 70% ethanol for 7 days. Specimens of 4-mm-long diaphyses were obtained immediately proximal to the tibio-fibula junctions using a diamond-saw cutter (South Bay Technology, SBT650).

### 2.2 SRCT

The sample imaging by SRCT was performed at beamline BL20B2 in the SR facility, Super Photon Ring-8GeV (SPring-8) in Harima, Japan. The detailed experimental arrangement for utilizing monochromatic SR has been described in early works (16, 18). In the present study, we used 20-keV X-ray (photon flux incident:  $>1 \times 10^9$  photons/sec/mm<sup>2</sup>; X-ray size: 5 mm (H)  $\times$  75 mm (W)).

The specimens were encapsulated in a polyethylene tube and mounted on a stage allowing high-precision translations and rotations (Fig. 1). A high-resolution X-ray detector, consisting of a fluorescent screen, a beam monitor (Hamamatsu Photonics, AA40P), and a cooled CCD camera (Hamamatsu Photonics, C4880-10-14A), was used for the radiographic imaging (Fig. 2). The viewing field of 4.0 mm (H)  $\times$  5.8 mm (W) was resolved into 5.83- $\mu$ m pixels with 14-bit resolution. Radiographic images were acquired over an angular range of 0°-180° in 0.5° steps. Reconstruction was made with a 2D filtered backward projection algorithm,

providing 700 contiguous 2D images comprised of  $1000 \times 1000$  cubic voxels of  $5.83 \mu\text{m}$  in size. The reconstructed images were re-digitized with 8-bit resolution, proportional to the linear absorption coefficient. Commercial volume-rendering software (Studio Pon, FORGE) was used for the 3D visualization of the canal network.

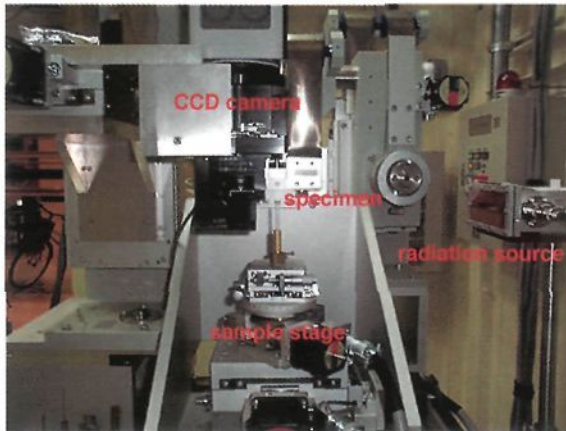


Figure 1. CT system in SPring-8 BL20B2 experimental hutch. The sample stage consists of a multiple-axis high precision diffractometers placed on the X-Y translation stages.

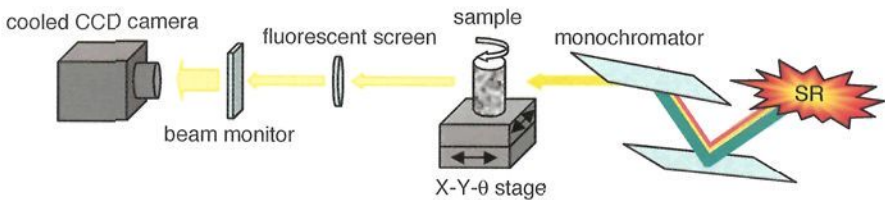


Figure 2. SRCT experimental setup. Polychromatic SR is monochromatized to 20-keV X-ray through a double crystal monochromator.

### 2.3 Calibration

The use of monochromatic SR allows the quantification of bone hydroxyapatite (HAp) because of no beam hardening artifacts. Assuming that the X-ray absorption of bone is described as a two-phase mixture (HAp and light elements), a linear relationship holds between the linear absorption coefficient ( $\mu_{\text{bone}}$ ) and bone HAp density ( $\rho_{\text{HAp}}$ ). To determine the relationship, cylindrical phantoms containing dipotassium hydrogen phosphate ( $\text{K}_2\text{HPO}_4$ ) water solutions of various concentrations were measured by SRCT (14, 15). Only 6% difference of mass absorption coefficient between  $\text{K}_2\text{HPO}_4$  and HAp for 20-keV X-ray (NIST database) validates the use of  $\text{K}_2\text{HPO}_4$  solution as a substitute for the HAp powder solution.



The linear regression between the linear absorption coefficient and the concentration of  $K_2HPO_4$  solution provides

$$\mu_{\text{bone}} = 5.45 \cdot \rho_{\text{HAp}} + 0.81 \quad (r^2 > 0.999). \quad (1)$$

#### 2.4 Image analysis

The central sample portion with a height of 2332  $\mu\text{m}$  (i.e., 400 contiguous transverse sections) was analyzed for each specimen. Prior to the determination of bone structural indexes, SRCT images were binarized with a simple thresholding for bone segmentation. The simple thresholding operated well because the distributions of linear absorption coefficient of SRCT images showed the clear peak corresponding to HAp (Fig. 3). The threshold value was determined through the comparisons between 2D binarized SRCT images and the light micrograph of the non-decalcified sliced sample showing the same transverse section. A threshold value of  $5.3 \text{ cm}^{-1}$ , which corresponds to the HAp density of  $0.82 \text{ g/cm}^3$  (Eq. 1), was used for every image binarization. Figure 4 shows an example of 3D-rendered images of cortical tissue, medullary cavity, and cortical canal pores after bone segmentation.

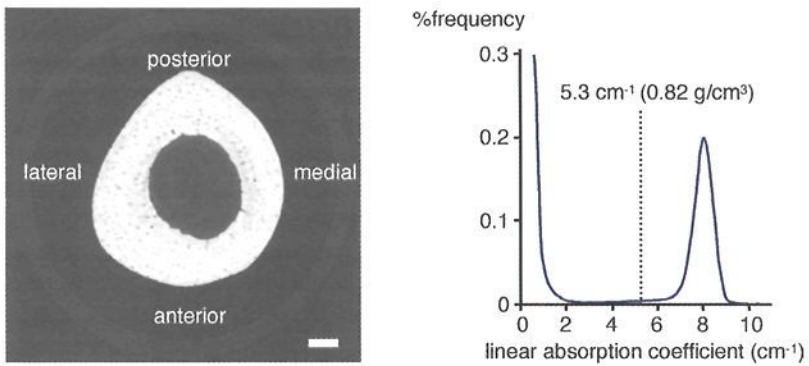


Figure 3. 2D-reconstructed image (left, bar, 200  $\mu\text{m}$ ) and the relative distribution of linear absorption coefficient (right). The threshold value for pure bone segmentation was set to  $5.3 \text{ cm}^{-1}$ .



Figure 4. 3D-rendered displays of reconstructed bone elements, based on 100 contiguous 2D binary reconstructed images.

As macroscopic structural indexes, calculated were the cortical tissue volume (CTV), the cortical transverse sectional area (CTA), and the medullary transverse sectional area (MA) were calculated, where the latter two were presented as the averages over 400 transverse sections. Trabeculae protruding into medulla were not excluded in calculating CTV and CTA because of their negligible occupation in medullary space (Fig. 4). The indexes characterizing cortical microstructure were the canal volume fraction (CaV/CTV), the mean canal cross-sectional area (CaCA), the number density of canals penetrating transverse sections (CaN/CTA) averaged over 400 transverse sections, the number density of canal bifurcations (CaBf/CTV), and the number density of canal links (CaLn/CTV). In the process of sectional image scanning, canal bifurcations where both branching canals extended beyond three contiguous slices and branching canals that met other canals ahead of their counterpart branch were included in the counts of CaBf and CaLn, respectively. The 26-adjacency was adopted for counting CaBf and CaLn.

Differences between OP and non-OP tibiae were assessed with Wilcoxon matched-pairs signed rank test. A value of  $P < 0.05$  was considered statistically significant. Data are represented as mean (SD).

### 3 Results

Figure 5 shows 2D-reconstructed images of OP and non-OP tibial transverse sections and 3D-rendered canal network images of the anterior-lateral regions of interest. The sciatic neurectomy induced bone atrophy; both CTV and CTA were significantly smaller while MA was significantly larger in OP than in non-OP tibiae ( $8.34 (0.32)$  vs.  $10.71 (0.49)$  mm<sup>3</sup>,  $3.58 (0.14)$  vs.  $4.59 (0.21)$  mm<sup>2</sup>, and  $1.22 (0.10)$  vs.  $1.14 (0.08)$  mm<sup>2</sup>,  $P < 0.05$ ).

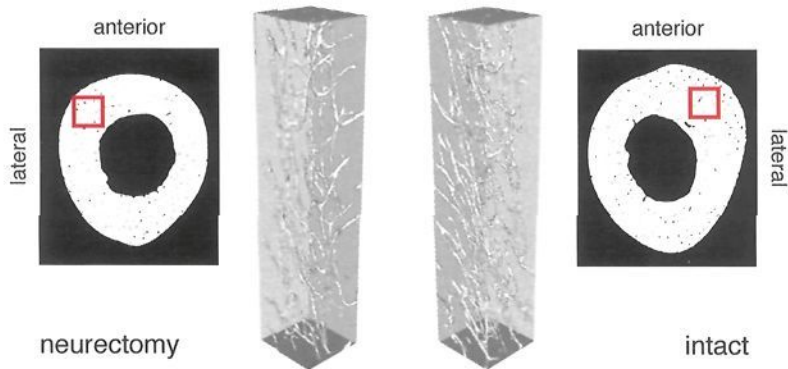


Figure 5. 2D-reconstructed images of OP (left) and non-OP (right) tibial transverse sections and volume-rendered images of regions of interest marked on the 2D images. Volume rendering was based on 400 contiguous 2D binary reconstructed images.

The microstructural indexes are compared in Fig. 6. All indexes showed significant differences, indicating the canal network rarefaction under neurectomy.

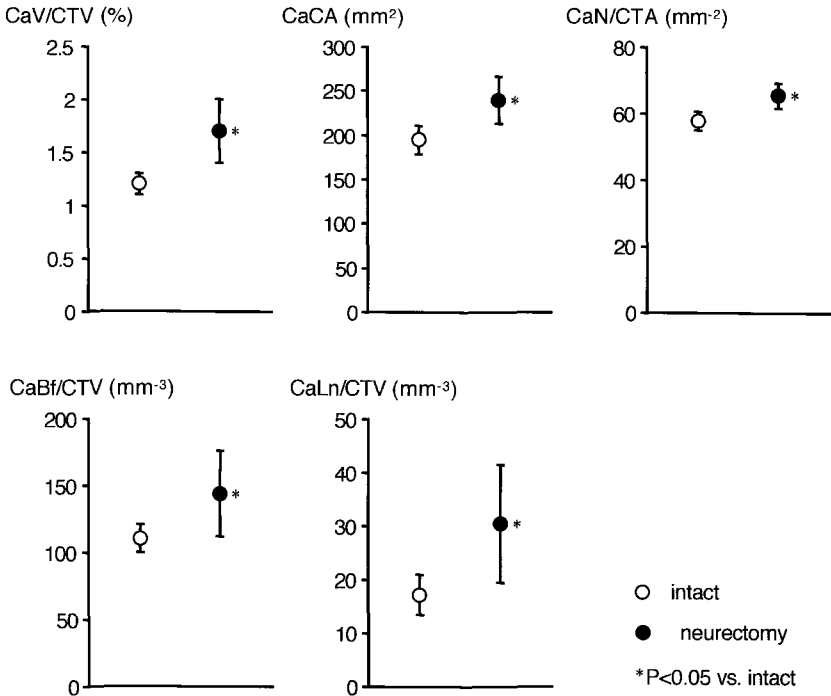


Figure 6. Comparisons of cortical microstructural properties between OP and non-OP tibiae.

No difference was found in the histogram of %frequency distribution of regional  $\rho_{\text{HAp}}$  values between OP and non-OP tibiae. Actually, there was no difference in both mean  $\rho_{\text{HAp}}$  (1.37 (0.01) vs. 1.36 (0.01)  $\text{g}/\text{cm}^3$ ) and the coefficients of variation of regional  $\rho_{\text{HAp}}$  values (0.085 (0.002) vs. 0.088 (0.002)) between OP and non-OP tibiae. These indicate no disuse effect on the bone mineralization.

## 4 Discussion

### 4.1 Advantages of SRCT

The major advantage of SRCT over conventional  $\mu\text{CT}$  is the availability of monochromatic X-rays, which makes SRCT free from beam hardening and allows the quantification of bone mineralization. The highly linear relationship between the concentration and the X-ray absorption of  $\text{K}_2\text{HPO}_4$  solution (Eq. 1) confirms the

validity of the present calibration method translating the SRCT image into the distribution of bone mineral density. The clearly differentiated peak of linear absorption coefficient corresponding to pure bone was also resulted from the use of monochromatic X-ray (Fig. 3), allowing a simple thresholding for the bone segmentation.

#### 4.2 Disuse effects on growing cortical bone

Disuse or immobilization caused by sciatic neurectomy induced bone atrophy as shown by the smaller CTV and CTA and the larger MA values in OP tibiae, indicating the disuse-induced deceleration of bone formation, the acceleration of bone resorption, or both, especially at the periosteal side. On the other hand, the sciatic neurectomy had no influence on bone mineral density. These tendencies are consistent with early studies on the cortical bone of sciatic neurectomized growing rats (21-23).

Regarding the cortical microstructure, all indexes demonstrate that the cortical canals are smaller the in cross section, more sparsely distributed, and less connected in OP tibiae (Fig. 6). Considering that canals possibly contain a single vessel of capillary structure, cortical microvasculature may also be reduced in OP tibiae. Interestingly, capillary network in disuse-induced atrophic soleus muscle is reduced in a similar manner to the present canal network rarefaction (24). The cortical microvascular rarefaction will lower the bone perfusion, enhance the perfusion heterogeneity (25), and decrease surface area for oxygen and nutrients supplies to bone cells.

The mechanism underlying the disuse-mediated canal network rarefaction is beyond the present scope. However, it could be speculated that loss of mechanical loading is responsible for such rarefaction during growth phase. Bone matrix deformation and/or interstitial fluid flow caused by loading induces osteocyte- and vascular endothelium-derived signals (26-30), which would regulate the bone resorption and formation around the cutting and closing cone of a progressing basic multicellular unit (BMU). Vascular growth or angiogenesis involved in BMU progression would be also driven through those signals (31, 32). During growth phase, the coupling of cortical canalization and vascularization would be coordinated through those signals to form a highly-developed cortical vascular network system, which supports the rapid bone gain through supplying sufficient oxygen and nutrients and facilitating a wash out of metabolic waste product.

The similarity between the mineral density distributions of OP and non-OP tibiae would make it reasonable to assume that the neurectomy-induced disuse affects the apparent cortical mechanical property essentially through the canal network rarefaction. To evaluate the effect of reduced canal network on the apparent cortical elasticity, we attempted the finite element analysis, in which 24 cubic bone blocks composed of  $48 \times 48 \times 48$  binarized voxels, one block in every cortical octant

at three tibial longitudinal positions, were examined in each tibia. Pure bone was modeled as a linear isotropic material with the elastic modulus and Poisson's ratio of 20 GPa and 0.3, respectively (intrinsic bone properties). The apparent elastic modulus was determined from the averaged stress resultant from a simple compression enforcing 1-mm displacement ( $-3,600$  microstrain) between two block faces opposing each other by means of a voxel finite element analysis. Differences in axial, radial, and circumferential apparent elastic moduli were only 1% at most between OP and non-OP tibiae (19.6 (0.2) vs. 19.7 (0.1), 19.4 (0.3) vs. 19.5 (0.2), and 19.3 (0.3) vs. 19.5 (0.2) GPa). That is, no effect of reduced canal network was found on apparent cortical elasticity.

### 4.3 Study limitations

It is not improbable that the widths of some vascular canals are close to or even smaller than the present voxel size of  $5.83 \mu\text{m}$  because even such small canals contain a single capillary of  $<5 \mu\text{m}$  in diameter observed in atrophic muscle (24, 33). Thus, there might be some differences between true and experimental values of indexes, especially CaLn/CTV, which are sensitive to artificial canal disconnections due to the thresholding or partial volume effects. More accurate measurements can be taken by SRCT arranged for resolving a sample into smaller voxels.

Although the observed canal network gives a conjecture about topological features of cortical microvascular network, whether canals contain vascular vessels and whether vascular diameters are correlated with canal diameters are not clear. Combining the monochromatic SRCT with a vascular casting or labeling method would allow a simultaneous evaluation of cortical canals and vascular vessels.

In conclusion, SRCT was shown to be useful for cortical microstructural analyses. Its application to tibial cortical bone of growing rats undergoing unilateral sciatic neurectomy demonstrated the disuse-mediated canal network rarefaction as well as the bone atrophy but no change of bone mineral density. The reduced cortical vascularity as a corollary to canal network rarefaction will decrease the cortical perfusion and increase the perfusion heterogeneity, probably having undesirable effects on the bone growth. The mechanism underlying this cortical microstructural alteration needs to be further investigated.

### Acknowledgments

We wish to thank Drs. T. Asano (Kawasaki Medical School) and K. Uesugi (JASRI) for their profound contribution to this study.

This study was supported partly by Grants-in-Aid for Scientific Research on Priority Areas 15086210 and for Scientific Research (B) 17300152 from the Ministry of Education, Science, Sports and Culture.

## References

1. Borah, B., Gross, G.J., Dufresne, T.E., Smith, T.S., Cockman, M.D., Chmielewski, P.A., Lundy, M.W., Hartke, J.R., Sod, E.W., 2001. Three-dimensional microimaging (MRmicroI and microCT), finite element modeling, and rapid prototyping provide unique insights into bone architecture in osteoporosis. *Anat. Rec.* 265, 101-110.
2. Feldkamp, L.A., Goldstein, S.A., Parfitt, A.M., Jasion, G., Kleerekoper, M., 1989. The direct examination of three-dimensional bone architecture in vitro by computed tomography, *J. Bone Miner. Res.* 4, 3-11.
3. Muller, R., Ruegsegger, P., 1997. Micro-tomographic imaging for the nondestructive evaluation of trabecular bone architecture. *Stud. Health Technol. Inform.* 40, 61-79.
4. McCalden, R.W., McGeough, J.A., Barker, M.B., Court-Brown, C.M., 1993. Age-related changes in the tensile properties of cortical bone. The relative importance of changes in porosity, mineralization, and microstructure. *J. Bone Joint Surg. Am.* 8, 1193-1205.
5. Sietsema, W.K., 1995. Animal models of cortical porosity. *Bone* 4, 297S-305S.
6. Brookes, M., Revell, W.J., 1998. Blood supply of bone: scientific aspects. London: Springer-Verlag.
7. Knothe, T.M.L., 2003. "Whither flows the fluid in bone?" An osteocyte's perspective. *J. Biomech.* 36, 1409-1424.
8. Robling, A.G., Stout, S.D., 1999. Morphology of the drifting osteon. *Cells Tissues Organs* 164, 192-204.
9. Stout, S.D., Brunsdon, B.S., Hildebolt, C.F., Commean, P.K., Smith, K.E., Tappen, N.C., 1999. Computer-assisted 3D reconstruction of serial sections of cortical bone to determine the 3D structure of osteons. *Calcif. Tissue Int.* 65, 280-284.
10. Bonse, U., Busch, F., 1996. X-ray computed microtomography (microCT) using synchrotron radiation (SR). *Prog. Biophys. Mol. Biol.* 65, 133-169.
11. Dilmanian, F.A., 1992. Computed tomography with monochromatic X-rays. *Am. J. Physiol. Imaging* 7, 175-193.
12. Grodzins, L., 1983. Optimum energies for x-ray transmission tomography of small samples: Applications of synchrotron radiation to computerized tomography I. *Nucl. Instrum. Meth.* 206, 541-545.
13. Peyrin, F., Salome, M., Nuzzo, S., Cloetens, P., Laval-Jeantet, A.M., Baruchel, J., 2000. Perspectives in three-dimensional analysis of bone samples using synchrotron radiation microtomography. *Cell. Mol. Biol. (Noisy-le-grand)* 46, 1089-1102.
14. Nuzzo, S., Lafage-Proust, M.H., Martin-Badosa, E., Boivin, G., Thomas, T., Alexandre, C., Peyrin, F., 2002. Synchrotron radiation microtomography allows the analysis of three-dimensional microarchitecture and degree of mineralization

- of human iliac crest biopsy specimens: effects of etidronate treatment. *J. Bone Miner. Res.* 17, 1372-1382.
15. Nuzzo, S., Peyrin, F., Cloetens, P., Baruchel, J., Boivin, G., 2002. Quantification of the degree of mineralization of bone in three dimensions using synchrotron radiation microtomography. *Med. Phys.* 29, 2672-2681.
  16. Sone, T., Tamada, T., Jo, Y., Miyoshi, H., Fukunaga, M., 2004. Analysis of three-dimensional microarchitecture and degree of mineralization in bone metastases from prostate cancer using synchrotron microcomputed tomography. *Bone* 35, 432-438.
  17. Bonse, U., Busch, F., Gunnewig, O., Beckmann, F., Pahl, R., Delling, G., Hahn, M., Graeff, W., 1994. 3D computed X-ray tomography of human cancellous bone at 8 microns spatial and 10-4 energy resolution. *Bone Miner* 25, 25-38.
  18. Ito, M., Ejiri, S., Jinnai, H., Kono, J., Ikeda, S., Nishida, A., Uesugi, K., Yagi, N., Tanaka, M., Hayashi, K., 2003. Bone structure and mineralization demonstrated using synchrotron radiation computed tomography (SR-CT) in animal models: preliminary findings. *J. Bone Miner. Metab.* 21, 287-293.
  19. Peyrin, F., Salome, M., Cloetens, P., Laval-Jeantet, A.M., Ritman, E., Ruegsegger, P., 1998. Micro-CT examinations of trabecular bone samples at different resolutions: 14, 7 and 2 micron level. *Technol. Health. Care* 6, 391-401.
  20. Salome, M., Peyrin, F., Cloetens, P., Odet, C., Laval-Jeantet, A.M., Baruchel, J., Spanne, P., 1999. A synchrotron radiation microtomography system for the analysis of trabecular bone samples. *Med. Phys.* 26, 2194-2204.
  21. Wakley, G.K., Baum, B.L., Hannon, K.S., Turner, R.T., 1998. The effects of tamoxifen on the osteopenia induced by sciatic neurotomy in the rat: a histomorphometric study. *Calcif. Tissue Int.* 43, 383-388.
  22. Yonezu, H., Ikata, T., Takata, S., Shibata, A., 1999. Effects of sciatic neurectomy on the femur in growing rats: application of peripheral quantitative computed tomography and Fourier transform infrared spectroscopy. *J. Bone Miner. Metab.* 17, 259-265.
  23. Zeng, Q.Q., Jee, W.S., Bigornia, A.E., King, J.G. Jr, D'Souza, S.M., Li, X.J., Ma, Y.F., Wechter, W.J., 1996. Time responses of cancellous and cortical bones to sciatic neurectomy in growing female rats. *Bone* 19, 13-21.
  24. Fujino, H., Kohzaki, H., Takeda, I., Kiyooka, T., Miyasaka, T., Mohri, S., Shimizu, J., Kajiya, F., 2005. Regression of capillary network in atrophied soleus muscle induced by hindlimb unweighting. *J. Appl. Physiol.* 98, 1407-1413.
  25. Hudetz, A.G., 1993. Percolation phenomenon: the effect of capillary network rarefaction. *Microvasc. Res.* 45, 1-10.
  26. Burger, E.H., Klein-Nulend, J., Smit, T.H., 2003. Strain-derived canalicular fluid flow regulates osteoclast activity in a remodelling osteon—a proposal. *J. Biomech.* 36, 1453-1459.

27. McGarry, J.G., Klein-Nulend, J., Mullender, M.G., Prendergast, P.J., 2005. A comparison of strain and fluid shear stress in stimulating bone cell responses – a computational and experimental study. *FASEB J* 19, 482-484.
28. Metz, L.N., Martin, R.B., Turner, A.S., 2003. Histomorphometric analysis of the effects of osteocyte density on osteonal morphology and remodeling. *Bone* 33, 753-759.
29. Noble, B.S., Peet, N., Stevens, H.Y., Brabbs, A., Mosley, J.R., Reilly, G.C., Reeve, J., Skerry, T.M., Lanyon, L.E., 2003. Mechanical loading: biphasic osteocyte survival and targeting of osteoclasts for bone destruction in rat cortical bone. *Am. J. Physiol. Cell Physiol.* 284, C934-C943.
30. Parfitt, A.M., 2000. The mechanism of coupling: a role for the vasculature. *Bone* 26, 319-323.
31. Carano, R.A., Filvaroff, E.H., 2003. Angiogenesis and bone repair. *Drug Discov. Today* 8, 980-989.
32. Tombran-Tink, J., Barnstable, C.J., 2004. Osteoblasts and osteoclasts express PEDF, VEGF-A isoforms, and VEGF receptors: possible mediators of angiogenesis and matrix remodeling in the bone. *Biochem. Biophys. Res. Commun.* 316, 573-579.
33. Kano, Y., Shimegi, S., Takahashi, H., Masuda, K., Katsuta, S., 2000. Changes in capillary luminal diameter in rat soleus muscle after hind-limb suspension. *Acta. Physiol. Scand.* 169, 271-276.



# STUDY ON PARTICLE PRESENTATIONS OF BLOOD CELLS AND THE PLASMA IN MICROVASCULAR BLOOD FLOW

T. YAMAGUCHI, S. WADA, K. TSUBOTA, H. KAMADA AND Y. KITAGAWA

*Department of Bioengineering and Robotics, Tohoku University,  
6-6-01 Aoba-yama, Sendai 980-8579, Japan  
E-mail: takami@pfs1.mech.tohoku.ac.jp*

To study the microcirculation for the analysis of thrombosis and haemolytic anaemia, fluid (plasma) flow and the motion of cellular components such as the red blood cell (RBC) and platelets must be included in the model. Vascular wall should also be included when the mechanical and biological interactions between the wall and cells are of concern. In the microvascular region, the cells and the plasma must be separately modeled because the length scale of the cellular components is comparable, sometimes larger, than the vascular diameter. To model the mechanical interactions between the cell and the wall, including their collisions, highly deformable nature of the cellular membrane must be represented in the model. In this study, a new computer simulation using particle method was proposed to analyze microscopic behavior of blood flow. A simulation region including plasma, red blood cells (RBCs) and platelets was modeled by an assembly of discrete particles. The proposed method was applied to the motion and deformation of single RBC and multiple RBCs, and the thrombogenesis process due to platelet aggregation.

## 1 Introduction

Cardiovascular disease is one of the most frequent causes of death in the industrialized world [1]. There is considerable indication that complex hemodynamics (blood fluid mechanics) play an important role in the development of atherosclerosis and other kinds of vascular diseases [2, 3]. Although the high amount of experimental, theoretical and numerical studies have been conducted in this area, according to our knowledge, there is not any study that reveals a direct evidence of the role of the blood fluid dynamics in the atherogenic process [3]. In this way, some unresolved questions need to be clarified, one of which is the blood flow at a blood cellular level.

Because the human blood can be regarded as a homogenous fluid from a macroscopic viewpoint, established numerical techniques based on continuum mechanics, such as finite difference method (FDM), finite volume method (FVM) and finite element method (FEM), have been used to analyze blood flow as homogeneous fluid. At a microscopic level, however, blood is treated as a suspension in which solid blood cells, such as red blood cells (RBCs), white blood cells (WBCs) and platelets, are suspended in fluid plasma. Consequently, the particle methods are a natural choice to simulate blood flow on a blood cellular scale, in which each component of blood is modeled by an assembly of discrete particles [4, 5].

The purpose of this paper is to propose a computer simulation method for blood flow using a particle method, in which solid blood cells and fluid plasma is directly modeled in order to investigate the microscopic behavior of blood flow. Motion of single deformable RBC [6] and thrombogenesis process due to platelet aggregation [7] are analyzed as a problem on a capillary scale. In addition, the particle method is useful to investigate the micro-macro relationships in the blood flow from a viewpoint of computational biomechanics considering multi-scale, in which mechanical interaction among multiple blood cells are important. To realize this kind of multi-scale simulation by direct modeling using a particle method, which is computationally expensive compared to FDM, FVM, and FEM, parallel-vector computation on the earth simulator (ES) system [8] is employed in the proposed particle method. This is one of a few means in a current computational environment that can overcome the difficulty in computing the collective behavior of large number of RBCs (order of 100  $\mu$  m to cm) directly from blood cellular scale ( $\mu$  m).

## 2 The MPS Methods

FDM, FVM and FEM have been very powerful and the most popular and widely used to solve engineering problems. In these methods, continuum domain is discretized into fixed discrete grids (nodes) or meshes (elements), which are connected together in a predefined manner with suitable interpolation function. This strategy with fixed grids or meshes assures both the robustness and accuracy when obtaining the solution of the differential equation by the discrete system. However, it also gives several limitations in analyzing complex geometries and multi-physics problems, which consequently limits their applications to biomechanical problem.

The limitations of the fixed grids- or meshes-based method have promoted the development of a mesh free method which use only a set of distributed nodes to express the mechanical system in a discretized form [9]. Each node is called "particle" in a particle method, and it moves in Lagrangean coordinates driven by interaction forces determined by discretized form of governing equations for the particles. This point makes it easy to track the solid-fluid interface in the case of large deformation. In a blood flow simulation using particle method, every particle can represents one discrete physical object (e.g. a small blood cell such as platelet) or can be generated as a set of particles to represent a part of the physical domain (e.g. a large blood cell such as RBC, and fluid plasma) [10], as shown in Fig. 1.

In this paper, the moving particle semi-implicit (MPS) method [11] is used to solve blood plasma flow. This method is a particle method developed for incompressible flow analysis based on Navier-Stokes (N-S) equations. The number density of particles is kept to be its reference value in order to express incompressibility. Gradient and Laplacian of physical quantity  $\phi$ , used in Navier-Stokes equations, on particle  $i$  are expressed by the summation of physical quantities

$\phi$  over neighboring particles  $j$  with a kernel function  $w$  (weighing function of distance) as

$$\langle \nabla \phi \rangle_i = \frac{d}{n^0} \sum_{j \neq i} \left[ \frac{\phi_j - \phi_i}{|\mathbf{r}_j - \mathbf{r}_i|^2} (\mathbf{r}_j - \mathbf{r}_i) w(|\mathbf{r}_j - \mathbf{r}_i|) \right] \quad (1)$$

and

$$\langle \nabla^2 \phi \rangle_i = \frac{2d}{n^0 \lambda} \sum_{j \neq i} \left[ (\phi_j - \phi_i) w(|\mathbf{r}_j - \mathbf{r}_i|) \right], \quad \lambda = \frac{\sum_{j \neq i} [|\mathbf{r}_j - \mathbf{r}_i|^2 w(|\mathbf{r}_j - \mathbf{r}_i|)]}{\sum_{j \neq i} w(|\mathbf{r}_j - \mathbf{r}_i|)}, \quad (2)$$

where  $\mathbf{r}$  is position vector,  $d$  is the number of space dimensions and  $n^0$  is the reference value of the particle number density [11]. With this discretization using particles, fluid flow is solved using an algorithm similar to a simplified marker and cell method. In the following, two-dimensional numerical examples are briefly summarized; (1) motion and deformation of single RBC [6], (2) primary thrombogenesis due to platelet aggregation [7], and (3) collective behavior of multiple RBCs.

### 3 Results

In the following, two-dimensional numerical examples are briefly summarized; (1) motion and deformation of single RBC [6], (2) primary thrombogenesis due to platelet aggregation [7], and (3) collective behavior of multiple RBCs.

#### 3.1 Motion and deformation of single RBC [6]

Blood flow on a capillary scale was analyzed to examine the basic characteristics of the proposed particle method. A two-dimensional particle model was constructed for the blood flow between parallel rigid plates, as shown in Fig. 2 ( $t = 0[s]$ ). The model consisted of fluid particles for the blood plasma, elastic particles for the RBC membrane, and rigid particles for the rigid plates. The size of the model was  $L = 80 \mu\text{m}$  in axial flow length and  $D = 10 \mu\text{m}$  in distance between the plates. Particle distance was set to  $0.5 \mu\text{m}$ , and total number of particles was 4919. The physical property of the plasma was assumed to be the same as that of water. As a boundary condition, constant and uniform velocity in the axial direction was applied to the fluid particles placed at the inlet. Reynolds number to the distance between the plates  $D$  was 0.1. Zero pressure was applied at the outlet, and non-slip condition at the inner vessel wall.

RBC was modeled by 59 particles configuring RBC membrane. These particles configured the same number of line elements in order to express the mechanical

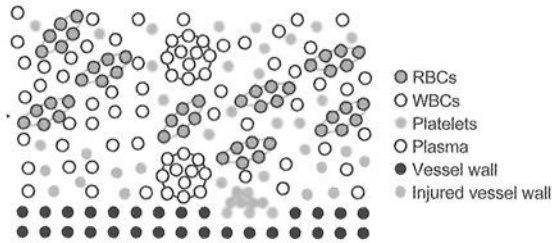


Figure 1. Particle model of blood consisting of blood cells, plasma and vessel walls.

behavior of membrane with small number of particles. Elastic energy of the membrane was considered for changes in the length of the element and the angle between the neighboring elements [12]. In addition, areal constraint was introduced to express internal pressure within RBC [12]. Initial biconcave shape, as shown in Fig. 2, was obtained by shape change simulation of a swollen RBC based on minimum energy principle in the case of decrease in the RBC area by 70% from circular shape.

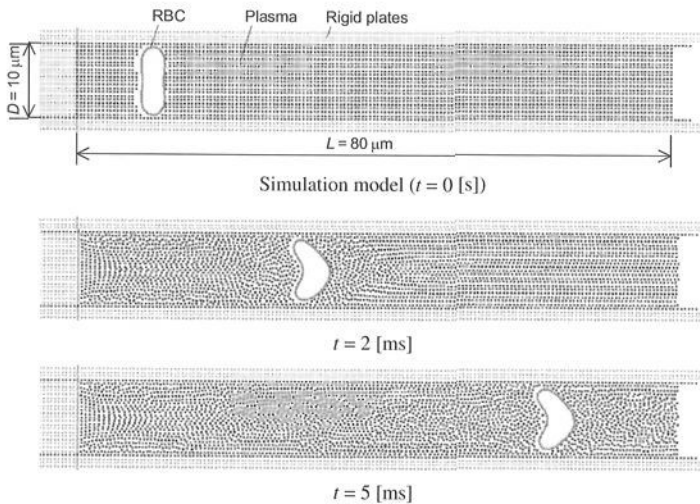


Figure 2. Motion and deformation of single RBC in blood flow.

A simulation result revealed change in RBC shape and position in blood flow, as shown in Fig. 2 ( $t = 2$  and  $5$ [ms])). Since fluid pressure was higher upstream than downstream, the RBC was accelerated to move downstream at the beginning of the simulation. The fluid pressure caused RBC deformation in concave upstream and

convex downstream. This shape corresponds to experimental observation, so called parachute shape. After the initial acceleration, the pressure force became proportional to the viscous force, and the RBC moved at constant velocity with keeping its deformed shape.

### 3.2 Primary thrombogenesis due to platelet aggregation [7]

The particle method simulation is applied to primary thrombogenesis due to platelet aggregation in injured vessel wall, in which fluid mechanical factors play an important role. Each platelet was modeled by single particle. Since the size of each platelet is considered to be very small compared to the characteristic size of blood vessel, platelets were assumed to move along with blood plasma flow when they were far from the injured part of blood vessel. In the near region of the injured part within distance  $d_{ag}$ , aggregation of the platelets was assumed to be stochastic and its probability to be higher for the platelets closer to the injured part. This probability was expressed by introducing an attractive force acting between the aggregating platelet and the injured wall. When the aggregating platelets were within the distance  $d_{ad}$  ( $< d_{ag}$ ), the platelets were assumed to adhere with the injured part and neighboring adhered platelets, and to behave as solid. The deformation of the adhered platelets as a solid was expressed by introducing normal and tangential spring forces acting among the adhered platelets and the injured wall.

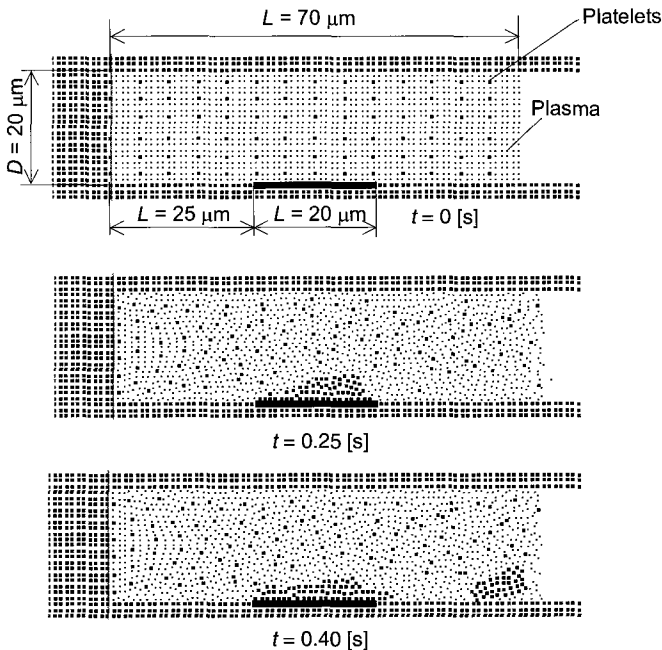


Figure 3. Primary thrombogenesis due to platelet aggregation in the blood flow.

A two-dimensional blood flow simulation between parallel plates was conducted in the case of Reynolds number of 0.02, as shown Fig. 2. The size of the model was  $L = 70 \mu\text{m}$  in axial flow length and  $D = 20 \mu\text{m}$  in distance between the plates. Particle distance was set to  $1.0 \mu\text{m}$ , and total number of particles was 3044.

An injured region was placed on the center of the lower plates. At  $t = 0.1$  [s], the platelets started to aggregate to the injured wall due to an attractive force acting between platelets and the injured wall. After the first aggregation, the number of platelets attached to the injured wall increased with time and the shape of the aggregated platelets grew until  $t = 0.25$  [s]. Thereafter, the platelets detached due to the fluid force of the plasma flow at  $t = 0.40$  [s]. These results suggest that the proposed particle method can simulate generation, growth and destruction of primary thrombus.

### 3.3 Collective behavior of multiple RBCs

In the much larger vessels than RBC size, collective behavior under the influence of mechanical interaction between RBCs is increasingly important to determine rheological properties of blood as a mass. In this section, a simulation method for multiple RBCs is proposed toward understanding of rheological properties of blood from a viewpoint of multi-scale mechanics. Assuming macroscopic flow field is not affected by each RBC motion, macroscopic flow field was prescribed by theoretical/numerical analysis [13]. The difference in the velocities between the RBC and the prescribed flow field determined momentum and viscous forces acting on RBC. In addition, reaction force is introduced in the case of contact of RBCs [13].

A two-dimensional blood flow model between parallel plates was constructed using  $10 \times 120 = 1200$  RBCs, as shown in Fig. 4(a). Each RBC was modeled by 100 particles. The size of the model was  $200 \mu\text{m}$  in axial flow length and  $75 \mu\text{m}$  in distance between the plates. The Poiseuille flow was assumed as the prescribed flow field. The ES system [8], a vector/parallel super computer system, was used to simulate the problem, in which we used 80 processors and 12 hours in real time (960 hours in CPU time). The parallel computation with standard MPI library was employed, and the simulation region was divided into 80 regions as the same

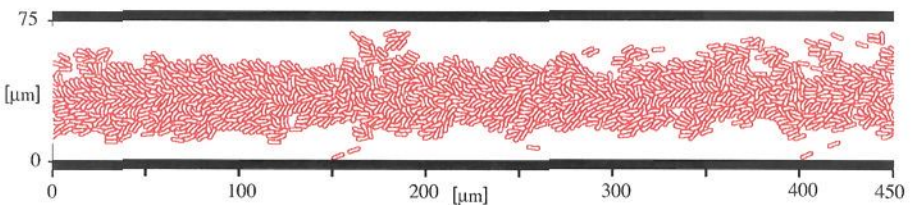


Figure 4. Multiple RBCs flow in the prescribed blood flow field.

number of the processors. Preliminary numerical experiments showed that the data communication time greatly affected computing time in the simulation. Therefore, the communication was performed per 1000 calculation steps, which did not change the essential result from that obtained in the case of full communication.

As for the simulation codes developed for 80 processors on the ES system, vector operation ratio, average vector length and parallel efficiency were 99.30%, 203.19 and 98.69%, respectively. These specs were acceptable to use 1024 processors in the ES system. The code enabled us to calculate blood flow in 98.9 [s] in the simulation time, in which RBCs were able to travel from the inlet to the outlet.

The simulation result demonstrated that RBCs flew downstream due to fluid force and concentrated to the flow axis, as shown in Fig. 4(b). This axial concentration, corresponding to experimental observation, would play an important role in distributing the RBCs into the daughter vessels at bifurcation [13].

#### 4 Discussion and Conclusion

Three applications of the particle method to study the blood flow were briefly analyzed. The simulation results demonstrate that the proposed method enables the analysis of single RBC motion and deformation, the initial thrombogenesis, growth and destruction of thrombus, and the collective behavior of multiple RBCs. This indicates that the particle method is potentially an important and useful approach to investigate the mechanical behavior of the blood cells in the blood flow at a microscopic level. Although the proposed method seems to be very useful in evaluating the microscopic mechanical behavior of blood flow, the results obtained by the computer simulation need to be validated by comparing with experimental data. In this way, we are currently developing a parallel plate flow chamber in order to obtain some experimental results by means of a confocal micro particle image velocimeter ( $\mu$  PIV). In addition, another very important ongoing work is to perform much larger-scale calculation using parallel computing technique, which will be an extended work of Sec. 3.3. The sophisticated computing techniques with a powerful hard ware, such as the ES system [8], will increase significantly the number of particles used in the proposed particle method. Furthermore, we intend to extend our simulations from a two dimensional analysis to a three dimensional analysis. With these developments, the proposed simulation method would express blood flow from viewpoints of both multi-physics and multi-scale, contributing to understanding of the over all properties of blood flow from blood cellular level (microscopic) to the resultant rheological properties of blood as a mass (macroscopic).

## **Acknowledgments**

This study was financially supported in part by a Grant-in-Aid for Scientific Research on Priority Areas 15086204 from the Ministry of Education, Culture, Sports, Science and Technology of Japan.

## **References**

1. Yamaguchi, T., 2000. Computational Mechanical Model Studies in the Cardiovascular System. *Clinical Application of Computational Mechanics to the Cardiovascular System* (Ed., Yamaguchi, T.) pp. 3-18, Springer-Verlag, Tokyo, Japan.
2. Fung, Y.C., 1997. *Biomechanics – Circulation* (2nd Edition). Springer-Verlag, New York.
3. Lipsch, D., , 2002. An Introduction to Biofluid Mechanics – Basic Models and Applications. *J. Biomech.* 35, pp. 415-435.
4. Miyazaki, H., Yamaguchi, T., 2003. Formation and Destruction of Primary Thrombi under the Influence of Blood Flow and von Willebrand Factor Analyzed by a Discrete Element Method. *Biorheology* 40, 265-272.
5. Boryczko, K., Dzwinel, W., Yuen, D.A., 2003. Dynamic Clustering of Red Blood Cells in Capillary Vessels, *Journal of Molecular Modeling* 9, 16-33.
6. Tsubota, K., Wada, S., Yamaguchi, T., 2004. A Particle Method Computer Simulation of Blood Flow. *Proc. of the 21st International Congress of Theoretical and Applied Mechanics (ICTAM04)* ISBN 83-89687-01-1, IPPT PAN (CDROM).
7. Kamada, H., Tsubota, K., Wada, S., Yamaguchi, T., 2004. Proposal of a Particle Method Simulation of Thrombogenesis. *Proc. of the Mechanical Engineering Congress (JSME) No.04-1* (6), 187-188 (in Japanese).
8. <http://www.es.jamstec.go.jp>
9. Li, S., Liu, W., 2002. Meshfree and Particle Methods and their Applications. *Applied Mechanics Reviews* 55, 1-34.
10. Tsubota, K., Wada, S., Yamaguchi, T., 2004. Mechanical Interaction among Blood Cells in Blood Flow Predicted by Computer Simulation using Particle Method. *Proc. of the 17th Computational Mechanics Conference (JSME), No04-40*, 69-70 (in Japanese).
11. Koshizuka, S., Oka, Y., 1996. Moving Particle Semi-Implicit Method for Fragmentation of Incompressible Fluid. *Nucl. Sci. Eng.* 123, 421-434.
12. Wada, S., Kobayashi, R., 2003. Numerical Simulation of Various Shape Changes of a Swollen Red Blood Cell by Decrease of its Volume. *Transactions of the JSME* 69A, 14-21 (in Japanese).



13. Sato, M., Wada, S., Tsubota, K., Yamaguchi T., 2005. Computer Simulation of the Flow of Elastic Red Blood Cells in Two-Dimensional Branch. Proc. of the 17th Bioengineering Conference (2004 Annual Meeting of BED-JSME) No04-48, 243-244 (in Japanese).

# **BRIEF REVIEWS OF MECHANICAL MODELS OF SKELETAL MUSCLE AND FORMULATION OF A MUSCLE MODEL TAKING INTO ACCOUNT MICROSTRUCTURE AND DAMAGE**

E. TANAKA AND D. ITO

*Department of Mechanical Science and Engineering, Nagoya University,  
Furo-cho, Chikusa-ku, Nagoya 464-8603, Japan  
E-mail: e\_tanaka@nagoya-u.jp*

Skeletal muscle models for computer simulations are reviewed, and special emphasis is located on models taking into account a three-dimensional architecture and microscopic structure of skeletal muscle. Then a model describing damage as well as deformation is proposed by taking into account a three-dimensional architecture and microscopic structure and by modifying the model in literature. It is ascertained that the proposed model describes damage properties of muscle qualitatively.

## **1 Introduction**

Skeletal muscle is a motor organ and is responsible for moving and stabilizing parts of the body. For applications in biomechanics and biomedical engineering, we often need a simulation model to understand and elucidate the mechanical properties and functional behavior of the skeletal muscle. For this purpose, many researchers developed mathematical models.

Skeletal muscle has a hierarchical structure that consists of sub-scale microstructure. For accurate description of mechanical properties of skeletal muscle, the three-dimensional architecture and the deformation mechanisms of muscle should be incorporated into the model based on a physical consistency and anatomical accuracy.

In this paper, we first survey literatures on skeletal muscle models and discuss the scheme of our skeletal muscle modeling. Finally, we formulate a mathematical model of skeletal muscle taking into account microstructure and damage.

## **2 Brief Reviews of Skeletal Muscle Models**

### *2.1 Simplified skeletal muscle model*

Hill model [1] is the most famous 1-D skeletal muscle model. It represents the active and passive properties of the musculo-tendinous unit. The model has three components; the contractile element (active muscle force), the series elastic element (tendon and other soft tissue), and the parallel elastic element (passive muscle force).

Zajac [2] derived Lumped-parameter models based on Hill model. This model

took into account the effects of pennation angle between the line of action of the muscle and tendon.

These models are commonly used in musculoskeletal models to predict muscle forces, and have been recommended as the most practical and accurate approach for simulating human movement. But a three-dimensional architecture and microscopic structure of skeletal muscle is simplified in those models. Thus, for example, they cannot represent nonuniform shortening along some muscle fascicles during low-load elbow flexion (Pappas et al., [3]) resulting from a more complex arrangement.

## 2.2 Skeletal muscle models with geometric features

Some continuum models describing two- or three-dimensional shapes and internal microstructures of skeletal muscle have been developed. Gielen et al. [4] proposed a two-dimensional non-linear finite element model to simulate tibialis anterior muscle. The geometry was reconstructed by high-resolution MRI image and the fiber direction was reconstructed by diffusion tensor images.

The constitutive equation of the contractile myofibers was based on the micro-mechanical Huxley model. The stress developed in cross bridge process was derived from the attachment distribution function  $n(\xi, t)$ . In this model, it is assumed that the cross bridge force depends linearly on the coordinate  $\xi$ , with constant  $\kappa$ . The force developed by one cross bridge is then  $F = \kappa h \xi$ , where  $h$  is a typical attachment length. The Cauchy stress in a slice of half-sarcomere with thickness  $s/2$  was computed by summing all cross-bridge forces:

$$\sigma_a(t) = \frac{msh}{2l} \int_{-\infty}^{\infty} \kappa \xi h n(\xi, t) d\xi \quad (1)$$

where  $m$  is the actin-site density, and  $l$  is the actin spacing.

To determine the distribution function  $n(\xi, t)$ , the process of attaching and detaching is expressed with a modified two state Huxley equation

$$\frac{Dn(\xi, t)}{Dt} = \frac{\partial n(\xi, t)}{\partial t} + v_r \frac{\partial n(\xi, t)}{\partial \xi} = r(t) f(\xi) [\alpha(l_s) - n(\xi, t)] - g(\xi) n(\xi, t) \quad (2)$$

The constitutive equation of the connective tissue network and the passive elements within the muscle fiber is given by a strain energy density function  $W_s$ :

$$\sigma_p = \frac{1}{J} \mathbf{F} \cdot \frac{\partial W_s(\mathbf{E})}{\partial \mathbf{E}} \cdot \mathbf{F}^c \quad (3)$$

where  $\mathbf{F}$  and  $\mathbf{F}^c$  are a deformation gradient and its conjugation,  $\mathbf{E}$  is the Green-Lagrange strain tensor, and  $J = \det \mathbf{F}$ . As the viscous effects of muscle tissue only seem to play a role at large sarcomere lengths and resting muscle, they are neglected in the model.

In order to specify an anisotropic strain energy density function, an orthonormal vector basis  $e_i (i = 1, 2, 3)$  with  $e_1$  parallel to the fiber direction and  $e_2$  and  $e_3$

perpendicular to the fiber direction is chosen. With respect to this basis the strain tensor  $\mathbf{E}$  is written as the strain matrix  $\underline{E}$  with components  $E_{ij}$ . The functional form of  $W_s$  was chosen as:

$$W_s(\underline{E}) = a_0 \left[ \exp\left(a_1 I_E^2 + a_2 II_E + a_3 E_{11}^2 + a_4 (E_{12}^2 + E_{13}^2) - 1\right) \right] \quad (4)$$

where  $I_E$  and  $II_E$  represent the first and the second invariant of the Green-Lagrange strain tensor and the muscle tissue behaves (nearly) incompressible. This model examined the effects of variation in the fiber direction and the initial sarcomere length distribution on the muscle mechanics.

Yucesoy et al. [5] proposed a nonlinear finite element model using a two-domain approach. In this model, skeletal muscle is considered explicitly as two separate domains: (1) the intracellular domain and (2) extracellular matrix domain. To account for the trans-membranous attachments, the two domains are linked elastically.

The strain energy function mechanically characterizing the extracellular matrix includes two parts. The first part  $W_1$  represents the nonlinear and anisotropic material properties. The second part  $W_2$  includes a penalty function to account for the constancy of muscle volume:

$$W_1 = W_{ij}(\varepsilon_{ij}) = \begin{cases} k(e^{a_{ij}\varepsilon_{ij}} - a_{ij}\varepsilon_{ij}) & \text{for } \varepsilon_{ij} > 0 \\ -W_{ij}(|\varepsilon_{ij}|) & \text{for } \varepsilon_{ij} < 0 \text{ and } i \neq j \end{cases} \quad (5)$$

$$W_2 = \lambda_s (I_3 - 1)^2 + \lambda_t (I_3^{\text{avg}} - 1)^2 \quad (6)$$

where  $\varepsilon_{ij}$  is the Green-Lagrange strain in the local coordinate; the indices  $i, j = 1, 2, 3$  represent the local cross-fiber, fiber and thickness directions, respectively. The  $I_3$  is the third invariant of the right Cauchy-Green strain tensor and  $I_3^{\text{avg}}$  is the weighted mean of all  $I_3$ s per element.

The total stress for the intracellular domain is the Cauchy stress acting only in the local fiber direction and is the sum of the active stress of the contractile elements and the stress due to intracellular passive tension.

The stress of contractile elements is defined as

$$\sigma_{22\text{contr}}(\varepsilon_{22}) = \begin{cases} b_3 e^{b_2 \varepsilon_{22}^3} & \text{for } \varepsilon_{22} > 0 \\ b_3 e^{b_1 \varepsilon_{22}^4} & \text{for } \varepsilon_{22} < 0 \end{cases} \quad (7)$$

This function is scaled such that at optimum length, the strain in the fiber direction is zero and the maximal stress value is unity. The stress due to intracellular passive tension was chosen as:

$$\sigma_{22\text{icp}}(\varepsilon_{22}) = \begin{cases} t_1 \varepsilon_{22}^2 + t_2 \varepsilon_{22} + t_3 & \text{for } \varepsilon_{22} > 0 \\ 0 & \text{for } \varepsilon_{22} < 0 \end{cases} \quad (8)$$

This model allowed assessment of force transmission and interaction between these domains. The results indicate the role of extracellular matrix for a muscle in sustaining its physiological condition. It is shown that if there is an inadequate linking to the extracellular matrix, the myofibers become deformed beyond physiological limits due to the lacking of mechanical support and impairment of a pathway of force transmission by the extracellular matrix. This leads to calculation of a drop of muscle force and if the impairment is located more towards the center of the muscle model, its effects are more pronounced.

Lemos et al. [6] also suggested an interesting model, which allowed the microscopic complexity of the system to account for the macroscopic results. Their model incorporated several possible structural levels of representation to predict force relationships.

In order to represent the tissue matrix for the passive soft tissues, it is represented by the Mooney-Rivlin relation:

$$W = a(I_c - 3) + b(II_c - 3) \quad (9)$$

where  $a$  and  $b$  are material parameters.

The force in activated muscle tissue represented as velocity-dependent form is given by:

$$F_{act} = a[f(r_0) + K(r_0)(r - r_0)] \frac{n_f}{10,000} f_v(v) \quad (10)$$

where  $f(r)$  is a force-length relationship given by parabola function. The variable  $r$  is the ratio  $r = L/L_{\text{opt}}$  and  $L_{\text{opt}}$  is the optimal fiber length, which corresponds to the vertex of the parabola. The stiffness  $K(r_0)$  represents the behavior for active elongations beyond the initial length  $r_0$ . The parameter  $n_f$  is the number of fibers running through a given element. It is assumed that the stress corresponds to the presence of 10,000 individual fibers per square millimeter. The function  $f_v(v)$  is the force-velocity dependence which results in the inclusion of a viscous component in the muscle fibers:

$$f_v(v) = 1 - \tanh\left(\frac{v}{120}\right) = 1 - \frac{(e^{v/120} - e^{-v/120})}{(e^{v/120} + e^{-v/120})} \quad (11)$$

The model is used to investigate force production and structural changes during isometric and dynamic contractions of the cat medial gastrocnemius. From comparison with experimental data, the model faithfully predicts all of the observations pertaining to force production, fascicle length and pennation angle under various test conditions.

These three-dimensional models represent macroscopic behavior and mechanical properties of skeletal muscle. In addition, internal distribution of stress, strain and each fiber shortening are also represented. Therefore, when considering contraction, shortening and muscle injury, it is possible to specify the portion of stress or strain concentration and explain the effects of nonuniform fiber length.

In practice, muscle tissue is damaged by excessive stretch of it. But the evolution of the damage to active and passive elements is not incorporated in those models.

### 2.3 Scheme of our skeletal muscle modeling

In the real world, muscle injuries are often observed in car crash and sport accidents, and simulations to predict muscle damage are often performed for injury prevention. For this purpose a constitutive model of muscle is prerequisite which can represent the damage distribution in muscle and the damage mechanisms as well as the above-mentioned mechanical properties of muscle. For this reason, we will formulate a constitutive model of muscle taking into account the effects of tissue damage on mechanical properties referring to Blemker et al. [7] in the following.

## 3 Formulation of a Skeletal Muscle Model Taking Into Account Microstructure and Damage

We considered muscle fiber and extracellular matrix as microstructure of skeletal muscle. We formulate the mechanical properties of muscle as an uncoupled form of the strain energy referring to Blemker et al. [7]. Then the strain energy density function is additively separated into the dilatational and deviatoric parts

$$\Psi_{total}(\mathbf{C}, \mathbf{a}_0) = \Psi_{dev}(\bar{I}_1, \bar{I}_2, \bar{I}_4, \bar{I}_5) + \Psi_{vol}(J) \quad (12)$$

where  $\mathbf{C}$  is the right Cauchy-Green deformation tensor,  $\mathbf{a}_0$  is the local fiber direction,  $\bar{I}_1$  and  $\bar{I}_2$  are deviatoric invariants of  $\mathbf{C}$ . The  $\bar{I}_4$  and  $\bar{I}_5$  are additional deviatoric invariants of  $\mathbf{C}$  that arise from the description of transverse isotropy, and  $J$  is equal to  $\sqrt{\det(\mathbf{C})}$  and expresses the relative change in volume. The deviatoric term is described by

$$\Psi_{dev} = W_1 + W_2 + W_3 \quad (13)$$

where  $W_1$  and  $W_2$  represent the strain energies of along-fiber and cross-fiber shear of intramuscular connective tissue, respectively. The term  $W_3$  describes the relationship between Cauchy stress in the fibers ( $\sigma_{total}^{fiber}$ ), the fiber stretch ( $\lambda$ ) and activation level of the fiber ( $\alpha$ ) in the form:

$$\lambda \frac{\partial W_3^{muscle}}{\partial \lambda} = \sigma_{total}^{fiber}(\lambda, \alpha) \quad (14)$$

To define  $\sigma_{\text{total}}^{\text{fiber}}$ , several assumptions are made. A force-length relationship led by Zajac [2] was used. The active stress is scaled linearly with respect to the activation level, which varies from 0 (no activation) to 1 (maximal activation):

$$\sigma_{\text{total}}^{\text{fiber}}(\lambda, \alpha) = \sigma_{\text{max}} \left\{ f_{\text{passive}}^{\text{fiber}}(\lambda) + \alpha f_{\text{active}}^{\text{fiber}}(\lambda) \right\} \lambda / \lambda_{\text{off}} \quad (15)$$

where  $\sigma_{\text{max}}$  is the maximum isometric stress,  $f_{\text{passive}}^{\text{fiber}}$  is a passive fiber force,  $f_{\text{active}}^{\text{fiber}}$  is an active fiber force,  $\lambda_{\text{off}}$  is the optimal fiber length.

To describe the microdamage of the muscle tissue, we introduced two damage variables into  $W_3$  which are defined by

$$W_3 = \int \frac{\sigma_{\text{max}}}{\lambda_{\text{off}}} \left\{ (1 - D_p) f_{\text{passive}}^{\text{fiber}} + \alpha (1 - D_p)(1 - D_a) f_{\text{active}}^{\text{fiber}} \right\} d\lambda \quad (16)$$

The variables  $D_p$  and  $D_a$  describe the damages of passive and active elements, respectively. When the passive element is damaged, the function of the force generation of the muscle fiber will be lost. Therefore the passive damage variable operates on both  $f_{\text{passive}}^{\text{fiber}}$  and  $f_{\text{active}}^{\text{fiber}}$ . The evolution equations of the two damage variables are represented by

$$\dot{D}_p = A_p e^{B_p D_p} \langle \dot{\lambda} \rangle \langle \lambda - \lambda_{yp} \rangle \quad (17)$$

$$\dot{D}_a = A_a e^{B_a D_a} \langle \dot{\lambda} \rangle \langle \lambda - \lambda_{ya} \rangle \quad (18)$$

where  $A_p$ ,  $A_a$ ,  $B_p$ ,  $B_a$  are material constants, and  $\lambda_{yp}$ ,  $\lambda_{ya}$  are the threshold fiber stretches of injury generation of passive and active elements. The symbol  $\langle \rangle$  is Macauley bracket defined by

$$\langle x \rangle = \begin{cases} x & \text{when } x \geq 0 \\ 0 & \text{when } x < 0 \end{cases} \quad (19)$$

These equations represent that the muscle tissue damage evolves only if stretch exceeds the threshold.

To examine the adequacy of the proposed model, we simulated uniaxial stretching of muscle tissue. An example of simulation result of the proposed model is shown in Figure 1.

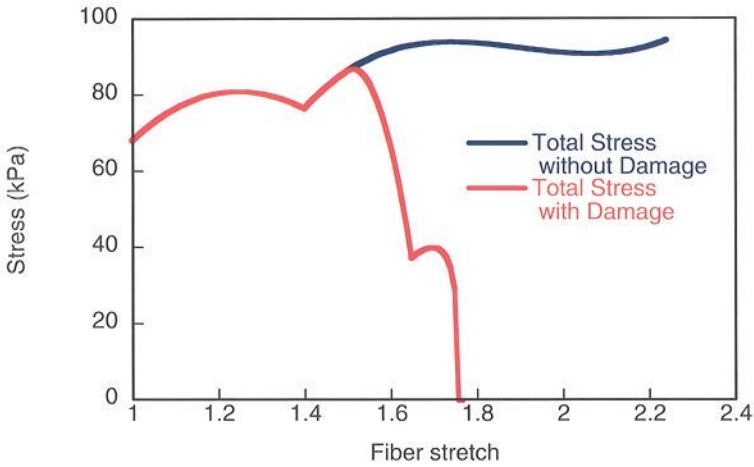


Figure 1. Comparison between the stress-strain curves of muscle fiber with and without damage evolution.

The red line shows the result of the model including microstructural damage and the blue one describes the ones predicted by the model without damage evolution. Second decrease on stress curve represented active element damage, and last one represented passive damage. The proposed model could describe the evolution of the internal tissue damage and predict the failure of the fiber qualitatively.

#### 4 Concluding Remarks

In this study, we surveyed the typical mechanical models of skeletal muscle, and formulated the constitutive model taking into account microstructure and damage. For describing mechanical behavior of skeletal muscle quantitatively, we need to identify better material functions and constants of the proposed model based on experimental data; which is our future work.

Another approach to represent macroscopic properties of muscle deformation and damage taking into account microscopic properties is to use the homogenization technique. Palmer [8] developed a computational model of a single fiber based on the homogenization method which is a rigorous mathematical theory for composite materials. In practical application, the homogenization method may be applied to problems with a relatively large scale ratios between the microlevel and macrolevel of the material and to problems with randomly oriented microstructures. The advantages of the homogenization method are its theoretical structure, greater



flexibility in deal with non-linear problems and localization of stress-strain fields. Although the homogenization method is not new in mechanics, it provides the framework for developing new techniques to analyze the behavior of heterogeneous materials.

### **Acknowledgements**

This work was supported by Grant-in-Aid for Scientific Research on Priority Areas 15086208 from the Ministry of Education, Culture, Sports, Science and Technology of Japan.

### **References**

1. Hill, A.V., 1938. The heat of shortening and the dynamic constants in muscle, *Proceedings of the Royal Society London*, 126, 136-165.
2. Zajac, F.E., 1989. Muscle and tendon: properties, models, scaling, and application to biomechanics and motor control, *Critical Reviews in Biomedical Engineering* 17, 359-411.
3. Pappas, G.P., Asakawa, D.S., Delp, S.L., Zajac, F.E., Drace, J.E., 2002. Nonuniform shortening in the biceps brachii during elbow flexion, *J. Appl. Physiol.* 92, 2381-2389.
4. Gielen, A.W.J., 1998. A continuum approach to the mechanics of contracting skeletal muscle, Ph.D. thesis, Eindhoven University of Technology.
5. Yucesoy, C.A., Koopman, B.H.F, J.M., Huijing, P.A., Grootenboer, H.J., 2002. Three-dimensional finite element modeling of skeletal muscle using a two-domain approach: linked fiber-matrix mesh model, *J. Biomech.* 35, 1253-1262.
6. Lemos, R.R., Epstein, M., Herzog, W., Wyvill, B., 2004. A Framework for Structured Modeling of Skeletal Muscle, *Computer Methods in Biomechanics and Biomedical Engineering* 7, 305-317.
7. Blemker, S.S., Pinsky, P.M., Delp, S.L., 2005. A 3D model of muscle reveals the causes of nonuniform strains in the biceps brachii. *J. Biomech.* 38, 657-665.
8. Palmer, M.L., 2004. A Non-Linear Hierarchical Model of Stretch-Induced Injury to Skeletal Muscle Fibers, Ph. D. thesis, The University of Michigan.

# NUMERICAL SIMULATION OF THE EFFECTS OF ACTIN BINDING AND CELLULAR DEFORMATION ON THE ORIENTATION OF ACTIN STRESS FIBERS UNDER CYCLIC STRETCH

H. YAMADA, H. ANDO AND D. MORITA

*Department of Biological Functions and Engineering Graduate School of Life Science and Systems Engineering, Kyushu Institute of Technology,  
2-4 Hibikino, Wakamatsu-ku, Kitakyushu 808-0196, Japan  
E-mail: yamada@life.kyutech.ac.jp*

We made theoretical predictions of the orientation of actin stress fibers (SFs) in a substrate-attached endothelial cell subjected to cyclic stretch within a constant range of strains. Taking account of polymerization/depolymerization of actin monomers and binding of SFs to adjacent actin filaments (AFs), we simulated the formation of SFs at the basal membrane. The numerical simulations predicted that AFs would be bundled but remain crossed with other AFs, which suggested that an additional mechanism was needed for the model to reproduce the actual distribution of AFs. Next, we validated two working hypotheses that defined the maximum strain in a SF during deformation as either the strain measured at maximal substrate deformation or the strain measured at maximal compression or stretching. Nonuniform cell deformation was also incorporated into the model. Under certain conditions of cyclic stretching of SFs for which one end of the fiber was attached to the apical membrane, the different measures of maximum strain produced clear differences in the position of the other end of the fiber.

## 1 Introduction

Endothelial cells on the luminal side of the arterial wall align longitudinally under flow shear stress, thereby avoiding the strain that results from cyclic deformation of the vascular wall [1-3]. Under such loading conditions, stress fibers (SFs) or bundles of actin filaments (AFs) located on the basal membrane of the cell are observed to orient in the major axis of the cell [4-8]. Wang et al. reported a “tent-like” actin structure in which AFs orient out of the basal membrane surface under cyclic equibiaxial stretch conditions [6]. The alignment of SFs running between the apical and basal membrane clearly differs from the cell’s major axis along the substrate surface. Yamada and Ando also observed SFs located above the nucleus in cells which were subjected to cyclic stretch [8].

To describe the orientation of vascular endothelial cells under cyclic stretch conditions, hypotheses were initially proposed for cell orientation under cyclic stretch conditions [2], and later for that of SFs [5, 9, 10]. Initial studies recognized SF responses qualitatively, as a phenomenon of deformation avoidance [1, 5]. Takemasa et al. explained the orientation angles of SFs on the basal membrane by quantifying the strain state of the substrate [5]. We conceptualize a forming process of AFs and SFs as a chemical response under

cyclic stretch conditions, with the orientation range restricted by the mechanical stress/strain state [9-12]. Civelekogu et al. modeled the reorganization of AFs focusing on the dynamic behavior [13].

In the current study, we first carried out numerical simulations of the formation of remodeled array of AFs on the basal region of an endothelial cell under cyclic uniaxial stretch. We focused on the actin binding between adjacent filaments as well as the polymerization/depolymerization to investigate their effects on the formed pattern of AFs.

We also validated the hypotheses using the two measures of maximum strain by comparing theoretical predictions of SF and AF orientation with experimental results reported in the literature. Then we performed numerical simulations of the orientation of SFs in different cytoplasmic locations under various conditions of cyclic stretch, comparing predicted results between these hypotheses. Finite element analyses have shown that cells deform nonuniformly [11] and this was included in our simulations.

## 2 Methods

### 2.1 Numerical simulation methods to predict the formation of AFs

The procedure of numerical simulation is:

- (1) Give a configuration of a cell (shape, location of integrins)
  - (2) Give an initial distribution of AFs by random orientation
- Repeat steps (3) to (5) until one obtains a stable pattern of AFs:
- (3) Check if polymerization {Eq. (1)} or depolymerization occurs (At 1000th step, divide all AFs into 2  $\mu\text{m}$ -segments)
  - (4) AFs will be bundled if the conditions in Table 1 are satisfied
- Every stretch cycle:
- (5) Check the strain of a AF at the maximum stretch state of substrate. If the strain is greater than the limit, then the AF will be dissociated immediately. If the strain is less than the limit, then the AF will remain.

Table 1. Conditions for actin binding in the numerical simulation.

Case	Distance between adjacent AFs (nm)	Angle between adjacent AFs (deg)	End of a AF for binding
A	100	10	plus
B	30	20	plus

The cell is a half ellipsoid with major and minor axes of 83  $\mu\text{m}$  and 45  $\mu\text{m}$  on the bottom surface and a height of 6  $\mu\text{m}$ . Integrins are located on the basal membrane with an interval of 2  $\mu\text{m}$ . AFs are assumed to start polymerization

from these locations. The type of cyclic stretch is a pure uniaxial stretch with a strain range of 20%. The cycle of stretch is 1 s. A single time step corresponds to 0.1 s. The strain limit of a AF is +/- 5%. With this limit, the angle range in which AFs can exist decreases as 46-134, 61-119 and 67-113 degrees with respect to the axis of stretch under cyclic pure uniaxial stretch with an increase of the strain range as 10%, 20% and 30%. The pure uniaxial stretch is a uniaxial stretch with a fixed length of the substrate in the transverse direction of stretch.

The polymerization of actin monomers at each end of a AF is governed by the equation

$$dn/dt = k_{on}M - k_{off} \tag{1}$$

where  $n$  and  $M$  are the number of attached actin monomers, concentration of actin monomers,  $k_{on}$  and  $k_{off}$ , capture rate constant and release rate constant, respectively [14]. We determined these constants as  $k_{on} = 1.5(\mu\text{M}^{-1}\text{s}^{-1})$ ,  $k_{off} = 0.2(\text{s}^{-1})$  at the plus end and  $k_{on} = 0.1(\mu\text{M}^{-1}\text{s}^{-1})$ ,  $k_{off} = 0.4(\text{s}^{-1})$  at the minus end, taking into account the variation of rate constants [15] and the evidence that a parallel array of SFs have appeared at 30 minutes under cyclic simple elongation at 1 Hz with a strain range of 30% [5]. In Eq. (1),  $M$  in the basal region is assumed to be constant as  $M = 190(\mu\text{M})$ . In the simulation, we checked the effect of the distance and angle to allow actin binding for adjacent AFs as summarized in Table 1.

## 2.2 Numerical simulation methods to predict the 3D orientation range of SFs

### 2.2.1 Hypotheses with different measures of maximum strain and categories of SF orientation

**Hypothesis 1:** A SF orients itself only in the direction in which the strain component in the fiber direction does not exceed the strain limit in the maximally deformed state of the substrate [10].

**Hypothesis 2:** A SF orients itself only in the direction in which the strain component in the fiber direction does not exceed the strain limit in the maximally stretched or compressed state of the SF during a cycle of cellular deformation [12].

These working hypotheses, formulated to predict the orientation of SFs after sufficient cycles of stretch, have different measures of SF maximum strain. Hypothesis 1 evaluates a SF's strain at the state in which the substrate is maximally deformed. Hypothesis 2 evaluates a SF's strain at the state in which the SF is stretched or compressed maximally during the deformation process of the substrate. According to our previous study (and with the assumption that the cells deform uniformly), whether the maximally deformed state of a SF coincides

with the maximally deformed state of the substrate is determined by the type and amount of deformation of the substrate [12].

SFs are classified into one of five categories depending on their orientation. SFs may connect (1) two points (focal adhesions) on the basal membrane, (2) two points (apical plaques) on the apical membrane, (3) the apical to the basal membrane, (4) the basal membrane and the nucleus, or (5) the apical membrane and the nucleus. Quantitative or qualitative observations of SF orientation in vascular endothelial cells exposed to cyclic deformation or fluid shear stress are reported in the literature for categories (1), (2) and (3) [1, 4-6, 16, 17]. SFs in categories (4) and (5) may also form in cells. In this study we focused on the case (3) which was of interest to predict the SF formation in various types of cyclic stretch.

### 2.2.2 Methods for validation of the working hypotheses and prediction of SF orientation

The above working hypotheses were validated by comparison of their predictions of SF and AF orientation in cultured endothelial cells (under conditions of cyclic pure uniaxial stretch and cyclic equibiaxial stretch, as well as SF orientation under conditions of cyclic simple elongation) with experimental measurements in the literature [10, 12] (Table 2, Figure 1). For the purposes of the validation, we assumed uniform deformation of the cell during substrate stretching.

Table 2. Boundary conditions of the substrate ( $\lambda_x$  and  $\lambda_y$  are stretch, and  $\sigma_x$  and  $\sigma_z$  are stress in the x or y direction, respectively).

Stretch condition	x-axis	y-axis	z-axis
Pure uniaxial stretch	$\lambda_x > 1$	$\lambda_y = 1$	$\sigma_z = 0$
Simple elongation	$\lambda_x > 1$	$\sigma_y = 0$	$\sigma_z = 0$
Equibiaxial stretch	$\lambda_x > 1$	$\lambda_y = \lambda_x$	$\sigma_z = 0$

To check whether the different measures of maximum strain in the two hypotheses produced differences in the predicted SF orientation, we used SFs with one end at the apical membrane. In the numerical simulations, a SF end was positioned at one of three locations on the apical membrane, points P, Q, and R, as shown in Figure 2. P', Q', and R' were the projected points of P, Q, and R on the basal membrane. To simulate nonuniform deformation of a cell, we approximated the deformation of the apical surface of the cell as

$$\lambda_x(z) = f(z) \cdot \lambda_x(0), \lambda_y(z) = g(z) \cdot \lambda_y(0), \lambda_z(z) = 1 / \{ \lambda_x(z) \cdot \lambda_y(z) \}, 0 \leq z \leq z_{\max} \quad (2)$$

for various types of substrate stretch (Table 2), using finite element models to reproduce the deformation of the cell [10, 11]. In Eq. (2),  $z$  is a coordinate in the

height direction of the cell,  $\lambda_x$ ,  $\lambda_y$  and  $\lambda_z$  are stretch in the  $x$ ,  $y$  and  $z$  directions, respectively,  $f(z)$  and  $g(z)$  are approximation functions at height  $z$ , and  $z_{max}$  is the height of the cell.

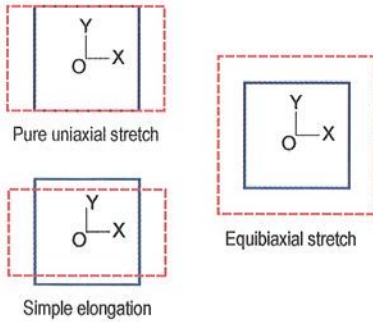


Figure 1. Three types of stretch for a substrate. A square with a solid line at an unstretched state deforms to a rectangle with a dashed line at the maximally stretched state.

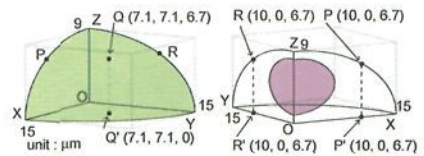


Figure 2. Selected points on the apical membrane (P, Q, R) and their projections on the basal membrane (P', Q', R') in a cell model, a quarter of the whole cell.

### 3 Results and Discussion

#### 3.1 Formation of AFs

Figure 3 shows the initial distribution of AFs through polymerization of actin monomers starting from the locations of integrins with random orientation.

Figure 4 shows the distributions of AFs after 5000 steps for the Case A in Table 1. In the figure, a black line denotes a AF which is a part of stress fibers, i.e., a bundle of AFs. A yellow line denotes an independent AF which is not bundled with any other AFs. The result shows that the orientations of AFs are not in specific directions yet.

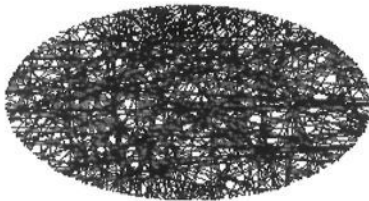


Figure 3. Initial distribution of AFs.



Figure 4. Distributions of AFs after 5000 steps for the Case A in Table 1.

Figure 5 shows the distributions of AFs on the basal membrane after 10000 steps for both cases in Table 1. Comparisons of these results show that a long distance between AFs which allows actin binding causes bundles with many filaments, and that a large angle between AFs tends to have more uniform directions between AFs. Compared these numerical simulation results with experimental ones in the literature, effective distance of AFs for binding seems to be much larger than the size of binding proteins, e.g., 30 nm. The angle between AFs for binding also seems to be not so small maybe due to a kind of Brownian movement.

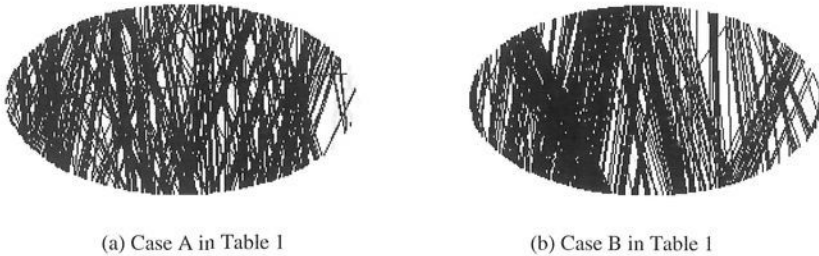


Figure 5. Distributions of AFs after 10000 steps.

### 3.2 Three dimensional orientation range of SFs

#### 3.2.1 Validation and comparison of the working hypotheses with the assumption of uniform cell deformation

We obtained predictions of SF orientation for three conditions of stretch (Table 2) with a 10% strain range and with the assumption of uniform deformation of the cell. Figure 6 compares the theoretical predictions of Hypothesis 1 with the experimental observations by Dartsch and Betz of AF orientation on the basal membrane of cultured endothelial cells exposed to cyclic pure uniaxial stretch with a 15% strain range [1, 12]. In this figure, dashed lines indicate AFs with 1% strain when the substrate is maximally stretched, and dot-dash lines are AFs with 5% strain. The results show that AFs orient in the angle range within which they are subjected to <5% strain. In our previous study, we compared the predictions of Hypothesis 1 to experimental measurements by Takemasa et al. of SF orientation on the basal membrane of cultured endothelial cells exposed to cyclic simple elongation with various strain ranges [4, 5, 10]. This result also showed that SFs orient in the angle range which has <5% strain.

We compared the predictions of the two hypotheses for the SF orientation range for the three boundary conditions in Table 2 with those for a <20% strain

range, which covers the physiological conditions of cyclic stretch. We found that if the strain limit of the SFs was 5%, there was no difference in the SF orientation predicted by the two working hypotheses. Small differences in the ranges of predicted orientations occurred when the SF strain limit was small (e.g., 1%) and the substrate strain range was simultaneously large (e.g., 20%).

Figure 7 presents theoretical predictions of the distributable range of the position of a AF end on the basal membrane, under the condition of cyclic equibiaxial stretch of the substrate with a 10% strain range, assuming that the other end of the AF is located at a height of 8 μm or 10 μm. As Wang et al. reported for the three-dimensional “tent-like” actin structures observed in their experiment, AF ends gather on the apical membrane, while the other end of each fiber is located at various points on the basal membrane [6]. One of these “tent-like” structures is shown in Figure 7 (from an image in Ref. [6]) with the positions of the AF ends on the basal membrane marked with the symbol (x). The simulations involving 10-μm AFs predicted an orientation range covering most of the (x) symbols on the basal membrane.

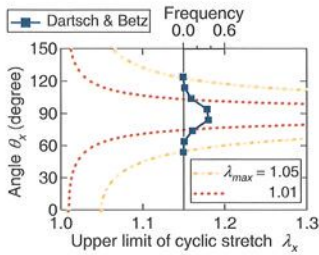


Figure 6. Predictions of the orientation angle of AFs by Hypothesis 1 under conditions of cyclic pure uniaxial stretch, with the SF strain limit at 1% or 5% [1, 12].

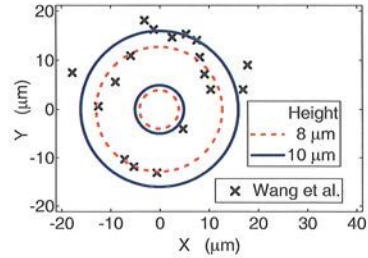


Figure 7. Predictions using Hypothesis 1 for the distributable region of a SF end on the basal membrane ( $Z = 0$ ) in AFs in which the other end is located at point  $(X, Y, Z) = (0, 0, 8)$  or  $(0, 0, 10)$  μm [6, 12].

### 3.2.2 Comparison of predicted results with the working hypotheses based on the nonuniform deformation of a cell model

The approximation functions in Eq. (2) are obtained as

$$\begin{aligned} f(z) &= 0.921 + 0.079 \exp(-0.322z), \\ g(z) &= 1 + \{-0.166 + 0.166 \exp(-0.508z)\}(\lambda_x(0) - 1) \end{aligned} \tag{3}$$

for a pure uniaxial stretch with 10% strain of the substrate in the x direction,

$$f(z) = 0.919 + 0.081 \exp(-0.246z), \quad g(z) = f(z)^{-1/2} \tag{4}$$

for a simple elongation with 10% strain of the substrate in the x direction, and



$$f(z) = 0.907 + 0.093 \exp(-0.349z), \quad g(z) = f(z) \quad (5)$$

for an equibiaxial stretch with 10% strain of the substrate in the  $x$  and  $y$  directions. The averaged errors in the displacement with the above approximation functions for all the nodes on the apical surface of the finite element model of the cell are 7%, 16% and 14%, respectively. The approximation functions therefore reproduce the deformed shape of the cell with a 1/10 order of these errors, because the displacements (e.g., 1.5  $\mu\text{m}$ ) are roughly one tenth of the size of the cell model (e.g., 15  $\mu\text{m}$ ). The deformation of the points on the basal surface of the cell is described without error.

The basal membrane positions of a SF end predicted by the two working hypotheses (under conditions of cyclic pure uniaxial stretch with a 10% strain range, and with the other end of the SF located at points P, Q, or R on the apical membrane) are shown in Figure 8. The black region in the figure indicates a SF end on the basal membrane; the grey region denotes a SF end on the nucleus surface. Points P, Q, and R are located at different positions in the cell model with regard to the deformation of the cell, and as a consequence the shape of the SF end distribution range does not have the same symmetry as one derived on the assumption of uniform deformation of the cell. The distributable range changes depending on the location of the SF's other end on the apical membrane. The two working hypotheses predict slightly different ranges.

Figure 9 shows the predictions of the two hypotheses for the positions of the basal membrane end of a SF (the other end of which is at P or R on the apical membrane) under cyclic simple elongation with a 10% strain range. There are some differences between the distribution range predicted under these conditions and those predicted with cyclic pure uniaxial stretch (Figure 8), and this is also the case for SFs orienting on the basal membrane.

Figure 10 shows the predictions of the two hypotheses for the positions of the basal membrane end of a SF (the other end of which is at P or R on the apical membrane) under cyclic equibiaxial stretch with a 10% strain range. The two hypotheses clearly predict different ranges. Under these conditions, the small size of the cell model (Figure 2) used in these predictions limits the distribution range, which is much larger in the predictions in Figure. 7. The cell in the experimental report by Wang et al. was actually larger than the region shown in their image (80  $\mu\text{m}$  by 50  $\mu\text{m}$ ) [6].

Our numerical simulations describe the distributional range of a SF end when the other end is at a specific location. By choosing a stretch condition and focusing on the end points of the SFs, this enables validation of the hypotheses explaining mechanical effects on SF orientation. Though the orientation of SFs is restricted by their deformation, it is still unknown which determines the actual array of SFs. Combination of mechanical and chemical responses would be required to reproduce the phenomenon.

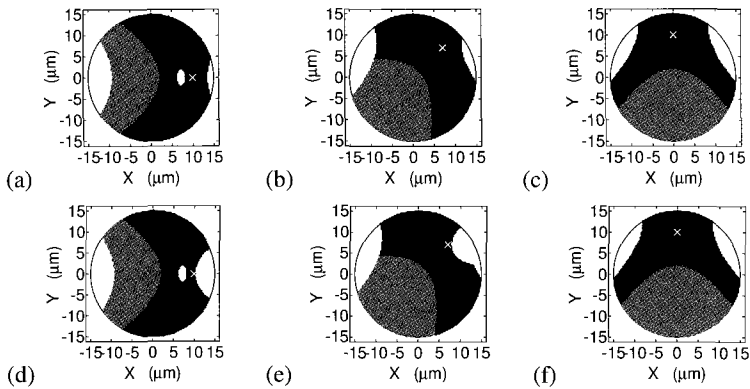


Figure 8. Predictions of the distributable region of a SF end on the basal membrane (black region) using Hypothesis 1 ((a), (b), (c)) or Hypothesis 2 ((d), (e), (f)) under conditions of cyclic pure uniaxial stretch of the substrate with a 10% strain range. The other end of the SF is at point P ((a), (d)), Q ((b), (e)) or R ((c), (f)). The grey region denotes that one end of a SF is not on the basal membrane but on the surface of the nucleus. The symbol (x) denotes a projected point on the basal membrane, i.e., point P' ((a), (d)), Q' ((b), (e)) or R' ((c), (f)).

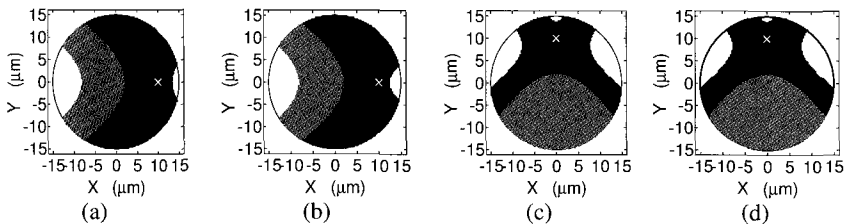


Figure 9. Predictions of the distributable region of a SF end on the basal membrane (black region) using Hypothesis 1 ((a), (c)) or Hypothesis 2 ((b), (d)) under conditions of cyclic simple elongation of the substrate with a 10% strain range. The other end of the SF is at point P ((a), (b)) or R ((c), (d)).

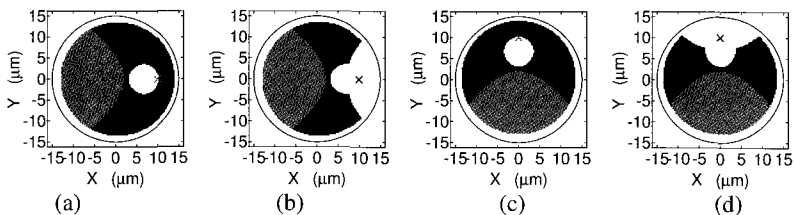


Figure 10. Predictions of the distributable region of a SF end on the basal membrane (black region) using Hypothesis 1 ((a), (c)) or Hypothesis 2 ((b), (d)) under conditions of equibiaxial stretch of the substrate with a 10% strain range. The other end of the SF is at point P ((a), (b)) or R ((c), (d)).

## 4 Conclusions

We performed a numerical simulation to reproduce the distribution of SFs on the basal membrane during cyclic stretching. The simulation reproduced the effects of distance and the angles of AFs on actin binding and a certain structure of AF arrays. The simulation revealed that an additional mechanism must exist to avoid crossing other AFs.

We also performed theoretical predictions of the orientation of SFs in an endothelial cell that was attached to a substrate and was exposed to cycles of biaxial stretching. First, we validated and compared two measures of the maximum strain in a SF using two formulations of a strain limit hypothesis. The results of the numerical simulations indicated that both measures produced accurate predictions of the orientation of SFs and AFs that have been reported in the literature. Next, incorporating the nonuniform deformation of the cell into the model, we predicted an orientation of SFs such that one end of the fiber was located at one of three positions on the apical membrane. Clear differences were observed between the distribution ranges predicted by the two hypotheses under conditions of cyclic equibiaxial stretch.

## Acknowledgements

This work was supported by Grant-in-Aid for Scientific Research on Priority Areas 15086213 from the Ministry of Education, Culture, Sports, Science and Technology of Japan and by a Grant-in-Aid for Scientific Research (C) 13650083 and 15560075 from the Japan Society for the Promotion of Science.

## References

1. Dartsch, P.C., Betz, E., 1989. Response of cultured endothelial cells to mechanical stimulation. *Basic Res. Cardiol.* 84, 268-281.
2. Wang, H., Ip, W., Boissy, R., Grood, E.S., 1995. Cell orientation response to cyclically deformed substrates: Experimental validation of a cell model. *J. Biomech.* 28, 1543-1552.
3. Owatverot, T.B., Oswald, S.J., Chen, Y., Wille, J.J., Yin, F.C-P., 2005. Effects of combined cyclic stretch and fluid shear stress in endothelial cell morphological responses. *Trans. ASME, J. Biomech. Eng.* 127, 374-382.
4. Takemasa, T., Sugimoto, K., Yamashita, K., 1997. Amplitude-dependent stress fiber reorientation in early response to cyclic strain. *Exp. Cell Res.* 230, 407-410.

5. Takemasa, T., Yamaguchi, T., Yamamoto, Y., Sugimoto, K., Yamashita, K., 1998. Oblique alignment of stress fibers in cells reduces the mechanical stress in cyclically deforming fields. *Eur. J. Cell Biol.* 77, 91-99.
6. Wang, J.H-C., Goldschmidt-Clermont, P., Moldovan, N., Yin, F.C-P., 2000. Leukotrienes and tyrosine phosphorylation mediate stretching-induced actin cytoskeletal remodeling in endothelial cells. *Cell Motility and the Cytoskeleton* 46, 137-145.
7. Wang, J.H-C., 2000. Substrate deformation determines actin cytoskeleton reorganization: A mathematical modeling and experimental study. *J. Theor. Biol.* 202, 33-41.
8. Yamada, H., Ando, H., 2005. The orientation of stress fibers at the apical/basal membranes of endothelial cells subjected to cyclic stretching. *Proc. Second Japan-Switzerland Workshop on Biomechanics, Kyoto, Japan, September 12-16, 2005.*
9. Yamada, H., Takemasa, T., Yamaguchi, T., 2000. Theoretical study of intracellular stress fiber orientation under cyclic deformation. *J. Biomech.* 33, 1501-1505.
10. Yamada, H., Morita, D., Matsumura, J., Takemasa, T., Yamaguchi, T., 2002. Numerical simulation of stress fiber orientation in cultured endothelial cells under biaxial cyclic deformation using the strain limit hypothesis. *JSME Int. J., Ser. C* 45, 880-888.
11. Yamada, H., Matsumura, J., 2004. Finite element analysis of the mechanical behavior of vascular endothelial cells in culture under substrate stretch. *Trans. Jpn. Soc. Mech. Eng.* 70, 710-716 (in Japanese).
12. Yamada, H., Matsumura, J., Morita, D., 2004. Numerical analyses of the deformation of vascular endothelial cells and the orientation of stress fibers. *Biomechanism* 17, 173-184, Keio Univ. Press (in Japanese).
13. Civelekoglu, G., Tardy, Y., Meister, J.-J., 1998. Modeling actin filament reorganization in endothelial cells subjected to cyclic stretch. *Bull. Math. Biol.* 60, 1017-1037.
14. Boal, D., 2002. *Mechanics of the Cell*, Cambridge University Press, Cambridge.
15. Suzuki, N., Mihashi, K., 1990. Dynamic polarity of F-actin, *Biophysics. Biophys. Soc. Jap.* 30, 220-226 (in Japanese).
16. White, G.E., Fujiwara, K., 1986. Expression and intracellular distribution of stress Fibers in aortic endothelium. *J. Cell Biol.* 103, 63-70.
17. Kano, Y., Katoh, K., Fujiwara, K., 2000. Lateral zone of cell-cell adhesion as the major fluid shear stress-related signal transduction site. *Circ. Res.* 86, 425-43.

This page is intentionally left blank

## SUBJECT INDEX

### A

Actin filament, 16, 64, 149  
Actin stress fibers, 51  
Activation level, 145  
Active fiber force, 146  
Active stress, 146  
Adaptive multimode lubrication, 37  
Adventitia, 17  
Aggregation, 87  
Alignment, 16, 115  
Anaemia, 132  
Anastomotic intimal hyperplasia, 105  
Angiogenesis, 26  
Anisotropy, 16  
Apical membrane, 152  
Apical plaques, 152  
Arterial wall, 16  
Arteriosclerosis, 26  
Articular cartilage, 37  
Artificial grafts, 96  
 $\alpha$ -smooth muscle actin, 73  
ATP receptor, 74  
ATP release, 75  
Atrophy, 121  
Autocrine, 74

### B

Barrier/sieve, 78  
Basal membrane, 152  
Basic multicellular unit, 127  
Beam hardening, 122  
BFGF, 26  
Biomechanics, 141  
Biphasic viscoelastic property, 37  
Bleb, 18  
Blood cells, 132  
Bone segmentation, 121  
Bovine pulmonary microvascular ECs, 27

**C**

- Ca<sup>2+</sup> wave, 75
- cAMP, 74
- Canal network rarefaction, 121
- Capillary-like structures, 26
- Capture rate constant, 151
- Cardiovascular disease, 132
- Cartilage, 87
- CBX, 75
- cDNA, 3
- Cell alignment, 113
- Cell contraction, 77
- Cell line, 3
- Cell morphology, 69
- Cell shape change, 74
- Cell shortening, 17
- Cell suspension, 17
- Cellular deformation, 149
- Cell-cell interaction, 87
- Celltracker, 31
- Centroid, 30
- Chinese hamster ovary (CHO) cells, 3
- Chondrocyte, 37, 87
- Cochlear amplification, 3
- Co-culture, 88
- Collagen, 27, 88, 109, 114
- Collagenase, 17
- Compression apparatus, 38
- Computed microtomography, 121
- Concentration of actin monomers, 151
- Concentration polarization, 96
- Confluent monolayer, 27
- Confocal laser scanning microscope (CLSM), 6, 28, 38
- Constitutive model of muscle, 145
- Contact inhibition, 69
- Contracted cell, 17
- Contraction, 16
- Cortical canal, 121
- Cortical microstructure, 121
- Cortical vascularity, 128
- Cyclic stretch, 149
- Cytochalasin D, 16
- Cytoskeletal structure, 16, 62

**D**

Damage, 141  
Damage variable, 146  
dBcAMP, 78  
Degenerated cartilage, 43  
Depolymerization, 51, 150  
Dipotassium hydrogen phosphate, 123  
Disassembly, 51  
Disuse, 121  
Duodenum, 75  
Dynamic stimuli, 113

**E**

Elastase, 17  
Elastic moduli, 114  
Elastic properties, 16  
Electromotility, 4  
Elongation, 62  
Endothelial cell, 26, 62, 103, 149  
Endothelin, 74  
End-to-end anastomoses, 99  
Enhancement, 32  
Enzymatic digestion, 16  
Enzyme, 17  
ePTFE graft, 98  
Equibiaxial stretch, 152  
Escherichia coli (E. coli), 3  
Expression level, 13  
Expression system, 3  
Expression vectors, 4  
Extracellular matrix, 37, 143

**F**

Fibroblast-like, 109  
Filtration flow, 96  
Finite element method (FEM), 38  
Fluorescent images, 45  
Focal adhesions, 152  
Friction, 40

**G**

Gap junction, 75, 92  
Gene expression, 88



Glycosylation, 3  
Green fluorescent protein (GFP), 6  
Gut, 72

**H**

Haemolytic, 132  
Hearing, 3  
Hemodynamics, 132  
Heterogeneous expression, 3  
Hill model, 141  
Homogenization method, 147  
Hydrostatic pressure, 62  
Hydroxyapatite, 123

**I**

Immunofluorescence experiments, 4  
Implanted graft, 96  
Inhomogeneity, 46  
Injury prevention, 145  
Integrin, 34, 150  
Intercellular adhesion, 69  
Intestinal villi, 72  
Intima, 97  
Intimal hyperplasia, 96  
Intimal thickening, 97  
Intracellular tension, 51  
Ischemic tissue, 26

**L**

Laser scanning microscope, 64  
Limiting dilution cloning, 3  
Linear absorption coefficient, 121  
Local fiber direction, 143  
Local strain, 38  
Localization, 4  
Low-density lipoproteins, 96  
Luciferin-luciferase, 76  
Luminal surface, 101  
Lumped-parameter model, 141

**M**

Macroscopic tissue level, 46  
Major axis, 16

Maximum isometric stress, 146  
Maximum tensile stresses, 114  
Mechanical property, 16, 81, 145  
Mechanical stimulation, 75  
Mechanical stimuli, 51, 62  
Mechanosensing, 72  
Mechanosensor, 79  
Mechano-transduction, 46  
Micro tensile tester, 16  
Microdamage of the muscle tissue, 146  
Microelement, 87  
Microscopic cellular level, 46  
Microstructure of skeletal muscle, 145  
Microvascular blood flow, 132  
Micro-mechanical Huxley model, 142  
Micro-vessel formation, 27  
Micro-vessels, 26  
Migration, 27  
Mineral density, 121  
Mineralization, 122  
Minor axis, 16  
Minus end, 151  
Monochromatic X-ray, 122  
Morphology of chondrocyte, 42  
Morphology of the network, 27  
Motor protein, 3  
Moving particle semi-implicit (MPS) method, 132  
MRS2179, 75  
Multilayering, 63  
Muscle damage, 145  
Muscle fiber, 142  
Muscle injuries, 145  
Myosin filament, 16

**N**

Natural synovial joints, 37  
Navier-Stokes (N-S) equations, 132  
Network length, 29  
NO, 34  
Nonlinear membrane capacitance, 10  
Normalized stiffness, 16  
Nucleus, 152  
Number of attached actin monomers, 151

**O**

- Optimal fiber length, 144
- Orientation, 62, 149
- Osteoarthritis, 40
- Osteoblast, 51
- Outer hair cells (OHCs), 3

**P**

- P2X, 74
- P2Y, 74
- Paracrine, 74
- Parallel-plate flow chamber, 28
- Particle, 132
- Passive fiber force, 146
- Pellet, 88
- Peristaltic reflex, 72
- Permeability, 39, 97
- Plasma, 132
- Platelets, 132
- Plus end, 151
- Polymerization, 150, 151
- Pore pressure, 39
- Porosity, 97
- Pressure gradient, 45
- Prestin, 3
- Pseudointima, 96
- Pure uniaxial stretch, 152

**R**

- Release rate constant, 151
- Remodeling, 62
- Reorganization, 51
- Restoration, 38
- Rotational culture, 89

**S**

- Sciatic neurectomy, 121
- Serotonin, 17
- Shape index, 62
- Shear stress, 27, 62
- Shrinkage, 112
- Simple elongation, 152
- Simulation, 132

Skeletal muscle, 141  
SMC, 16  
Smooth muscle cell, 16  
SPRING-8, 121  
Stable expression, 3  
Stem cell, 87  
Stiffness, 16  
Strain-dependent permeability, 45  
Strain energy density function, 142  
Strain limit, 151  
Strengthening, 115  
Stress fiber, 33, 62, 149  
Stress relaxation, 41  
Stretch, 77  
Subchondral bone, 41  
Synchrotron radiation computed microtomography, 121  
Synchrotron radiation, 121  
Synovial membrane, 109

**T**

Tensile properties, 17  
Tensile stresses, 109  
Tensile test, 16  
Tensile tester, 17  
Thoracic aorta, 17  
Three-dimensional (3D) models, 26  
Thrombogenesis, 132  
Thrombosis, 132  
Time-dependent and depth-dependent changes in local strain, 38  
Tissue engineering, 87  
Tissue recovery, 26  
Tortuosity index, 62  
Transfection, 6  
Transverse isotropy, 145  
Trypsin, 18

**U**

Unconfined compression, 41  
Uptake of LDL, 96

**V**

VE-cadherin, 69  
VEGF, 69

Vessel wall, 96

Villous motility, 77

## **W**

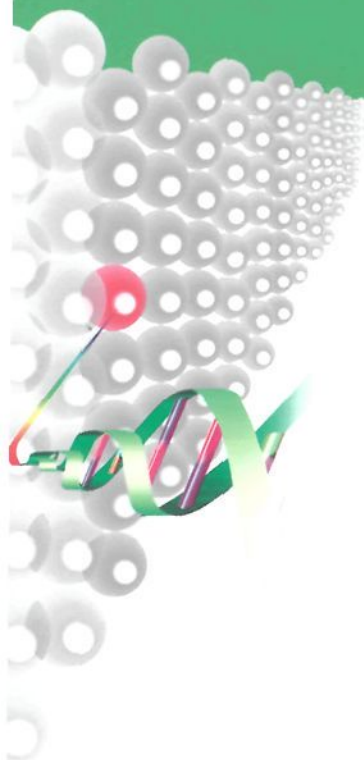
Water permeability, 96

Western blotting, 3

## **Y**

Young's modulus, 16

# BIOMECHANICS AT MICRO- AND NANOSCALE LEVELS



This book is essential reading for those interested in understanding current research trends in biomechanics at micro- and nanoscale levels. It details the research carried out to date in this field by fourteen prominent researchers as part of a four-year government supported project which commenced in 2003. The coverage includes four broad areas: cell mechanics, cell response to mechanical stimulation, tissue engineering, and computational biomechanics.